2016

Optical Parity Time Metasurface Structures

Ahmed El Halawany
University of Central Florida

OPTICAL PARITY TIME METASURFACE STRUCTURES

by

AHMED EL HALAWANY
Masters in Physics, University of Central Florida, 2016
Masters in Physics, American University of Cairo, 2008

A dissertation submitted in partial fulfillment of the requirements
for the degree of Doctor of Philosophy
in the Department of Physics
in the College of Science
at the University of Central Florida
Orlando, Florida

Fall Term
2016

Major Professor: Demetrios N. Christodoulides

ABSTRACT

In the last few years, optics has witnessed the emergence of two fields namely metasurfaces and parity-time (PT) symmetry. Optical metasurfaces are engineered structures that provide unique responses to electromagnetic waves, absent in natural materials. Optical metasurfaces are known for their reduced dimensionality i.e. subwavelength and consequently lower losses are anticipated. The other paradigm is the PT symmetric materials, also known as photonic synthetic matter. PT symmetry has emerged from quantum mechanics when a new class of non-Hermitian Hamiltonian quantum systems was highlighted to have real eigenvalues, hence eradicating Hermiticity of the Hamiltonian as an essential condition to the existence of real eigenvalues.

The first half of the thesis is focused on the experimental and numerical realization of PT symmetric metasurfaces. A systematic methodology is developed to implement this class of metasurfaces in both one-dimensional and two-dimensional geometries. In two dimensional systems, PT symmetry can be established by employing either H-like diffractive elements or diatomic oblique Bravais lattices. It is shown that the passive PT symmetric metasurfaces can be utilized to appropriately engineer the resulting far-field characteristics. Such PT-symmetric structures are capable of eliminating diffraction orders in specific directions, while maintaining or even enhancing the remaining orders.

Later, it is shown a first ever attempt of PT metasurface fabricated on a flexible polymer (polyimide) substrate. The studied PT metasurface exhibits the ability to direct light, i.e. Poynting vector in a desired direction. Herein, the light scattered from the fabricated device in the undesired direction is attenuated by at least an order of magnitude. The proposed PT symmetric metasurface is essentially diatomic Honeycomb Bravais lattice, where both the passive and lossy elements exist

side by side on each site separated by 50 nm. The unidirectionality of the studied metasurface is not limited to a single wavelength, on the contrary, it is observed to be effective on the entire visible band (400 – 600 nm). The PT symmetric meatsurface is also fabricated on a high strength substrate; sapphire (Al_2O_3). An excellent agreement between the experimental and numerical (COMSOL) results is found for both substrates. Customized modifications to the current design can open avenues to study the unidirectionality of metasurfaces to different optical bands, for example IR.

The second part of the thesis deals with the theoretical modeling of the dynamics of an electron that gets trapped by means of decoherence and quantum interference in the central quantum dot (QD) of a semiconductor nanoring (NR) made of five QDs, between 100 and 300 K. The electron's dynamics is described by a master equation with a Hamiltonian based on the tight-binding model, taking into account electron–LO phonon interaction. Based on this configuration, the probability to trap an electron with no decoherence is almost 27%. In contrast, the probability to trap an electron with decoherence is 70% at 100 K, 63% at 200 K and 58% at 300 K. Our model provides a novel method of trapping an electron at room temperature.

This setup is then used to propose a theoretical model for an electrically driven single photon source operating at high temperatures. It is shown that the decoherence, which is usually the main obstacle for operating single photon sources at high temperatures, ensures an efficient operation of the presented electrically driven single photon source at high temperatures. The single-photon source is driven by a single electron source attached to a heterostructure semiconductor nanoring. The electron's dynamics in the nanoring and the subsequent recombination with the hole is described by the generalized master equation with a Hamiltonian based on tight-binding model, taking into account the electron-LO phonon interaction. As a result of decoherence, an almost

100% single photon emission with a strong antibunching behavior i.e. $g^{(2)}(0) << 1$ at high temperature up to 300 K is achieved.

ACKNOWLEDGMENTS

Graduate school for me has been a long and arduous journey, and along the way there were a handful of people who played a significant role in me accomplishing my goal. I would like to start by extending my gratitude towards Professor Demetrios N. Christodoulides for accepting me in his group in January 2014. He has been a great support for me on so many levels. He entrusted me with the main project of this dissertation, and he gave me the confidence to finalize the project in a comprehensive manner. In addition, he generously sent me on multiple occasions to the nanoscale research facility (NRF) at University of Florida (UF) to take advantage of the available facilities at NRF. Professor Christodoulides was always available for valuable discussions, advice, and guidance. I am very thankful to him and cherish the opportunity he gave me.

I would like to thank Professor Talat S. Rahman, for being part of my dissertation committee despite her busy schedule. It is an honor to know her and I am very grateful for her advice and support during the ups and downs, especially in my particularly harsh times. She has been a constant source of hope and solace. I am thankful to Professor Robert Peale for taking interest in becoming part of my dissertation committee. My first interaction with him was in the “Classical Mechanics” course and later in “Electrodynamics II”. He is an excellent teacher and valuable asset to me when it came to experimental discussions. Thank you for lending me the mathematical integral book Prof. Peale. Also, I am grateful to Professor Patrick L. LiKamWa for being in my Ph.D. committee. Whenever I was stuck at my experiment, I used to go to his office to ask for tips and guidance. He was always happy to answer my questions no matter how basic they were. He was generous to let me use his optical table to finalize some measurements.

I would also like to extend my thanks to Professor Michael N. Leuenberger, I completed my project *Electrically driven Single Photon at High Temperature* under his mentorship.

Fabrication is a difficult and strenuous field and a perfectly designed sample often requires an assortment of techniques, machines and tricks. I have been very lucky to work with a team of professionals who helped me perfect my fabrication recipes. I would begin with thanking Dr. Ivan Divliniansky for his guidance in using the e-beam lithography at CREOL. I also had the opportunity to visit NRF, where I fabricated samples for one of my projects. The director of the NRF Dr. Brent Gila was extremely welcoming and always ready to share advice and resources. I learned a lot about fabrication techniques and systems while working with Andres Trucco, David Hayes, and Alvin Ogdin. While techniques, modeling, instruments have been a vital part of me finishing my tenure at UCF, an important part was the administrative support I received from the department of Physics, nanoscience technology center (NSTC), and CREOL staff. I would like to extend my hearty thanks to all the present and past staff members for their guidance and help in sorting out the executive aspects of my degree.

During my affiliations with the department of Physics, NSTC and CREOL, I came across some exceptional people, who later became good friends. Dr. Misha Erementchouk and Dr. Volodymyr Turkowski were great mentors and were always available for inputs and discussions. I would like to thank UCF Alumni Dr. Hani Khallaf and Professor Ramy El-Ganainy for their courteous invitations thus making me feel like home as a freshman graduate student. After starting at CREOL, Nicholas Nye became my hanging out buddy and great friend; we had a lot of fun exploring Orlando restaurants and getting into discussion involving work and any other topic we could conjure. I would like to extend warm wishes and multitude of thanks to Pedro Figueiredo.

Pedro is a dear friend and a comrade in arms when it came to tackling fabrication obstacles. We spent a lot of time untangling the various complications that arose while depositing materials and on fine tuning recipes. He has always provided a strong shoulder for support and empathy and I wish him the very best with his future endeavors. I would also like to extend my thanks to Ashoutsh Rao, Joshua Perlstein, Trenton Ensley, Christopher Lantigua, Felix Tan, Joshua Kauffman, Thamer Tabbakh, Yousef Alahmadi, Ali Abdulfattah, and Sarmad Alhasan. It was a pleasure to know you all and I wish you the very best with your future.

My family has always been a source of great comfort and encouragement. I would like to thank my father, mother, sister, and brother for their unconditional support and love during graduate school. I am especially grateful to my sister Ghada El Halawany, a source of profound knowledge, understanding and stability. I am thankful for the countless hours of talks and discussions, especially in the last three years. I would not have made it so far without her. My nephew Yassen El Halawany is a ray of sunshine in my life and has been a source of pure joy and contentment.

Last but not least, I am so glad to have Dr. Asma Amjad in my life. She is not just my Fiancé; she is also my best friend. Her continuous love, care, and support helped me overcome hard times. I am extremely lucky to have you (Asma) in my life!

"If my mind can conceive it, and my heart can believe it – then I can achieve it."

(The great Muhammed Ali)

Dedicated to My Family

&

My Fiancé

TABLE OF CONTENTS

LIST OF FIGURES

LIST OF TABLES

LIST OF ABBREVATIONS

1-D	One Dimensional
2-D	Two Dimensional
PT	Parity Time
FEM	Finite Element Simulations
CD	Conduction Band
NR	Nanoring
QD	Quantum Dot
SPS	Single Photon Source
OSPS	Optically Driven Single Photon Source
ESPS	Electrically Driven Single Photon Source
QPCs	Quantum Point Contacts

CHAPTER 1: PASSIVE PT-SYMMETRIC METASURFACES WITH DIRECTIONAL FIELD SCATTERING CHARACTERISTICS

1.1. Introduction

Recently, there has been considerable interest in synthesizing optical structures and devices that simultaneously exploit the presence of gain and loss domains, while maintaining parity time (PT) symmetry [1-14]. PT symmetry first emerged within the context of quantum field theories after recognizing that a special class of non-Hermitian Hamiltonians can exhibit entirely real eigenvalue spectra, as long as they commute with the anti-linear PT operator. In general, a necessary (but not sufficient) condition for PT-symmetry to hold is that the complex potential involved in such Hamiltonians should obey $V(r) = V^{*}(-r)$, which directly implies that the real part of the potential must be an even function of position, while the imaginary should be antisymmetric. Lately, such PT prospects have been proposed in the field of optics by recognizing that the complex refractive index distribution plays the role of an optical potential. In this case, PT-symmetry demands that $n(r) = n^{*}(-r)$. This latter condition clearly indicates that the refractive index profile must be symmetric, whereas the imaginary component (signifying gain or loss) must be an odd function in coordinate space. In more general settings, where the problem must be treated electrodynamically, this same symmetry can be introduced provided that the complex permittivity now satisfies $\varepsilon(r) = \varepsilon^{*}(-r)$ [14]. PT-symmetric optical arrangements can exhibit a number of exciting properties. These include for example power oscillations, non-reciprocal light propagation and Bloch oscillations [2-5], and unidirectional invisibility [12, 13] to mention a few.

In recent years, optical metasurfaces, a special class of metamaterials with reduced

dimensionality, have also received considerable attention. Such artificial surfaces can effectively control the flow of light through appropriately engineered subwavelength, surface-confined features that can introduce abrupt phase discontinuities after light encounters the interface [15-18]. So far, several studies have successfully demonstrated the use of optical metasurfaces in manipulating and controlling the phase, polarization and angular momentum of the incident light [19-24].

In this paper we show that one-dimensional (1-D) and two-dimensional (2-D) optical metasurfaces endowed with PT symmetry can display several intriguing characteristics. As we will show, PT-symmetry can be readily introduced in these systems through an appropriate amplitude and phase modulation when imposed on the surface. Even though bulk non-Hermitian gratings have been considered before in 1-D configurations [25-35], here we extend these concepts in more complex settings with particular emphasis on optical PT-symmetric metasurfaces. Such PT-symmetric structures are capable of eliminating diffraction orders in specific directions, while maintaining or even enhancing the remaining orders. In our study we provide all-passive 1-D and 2-D metasurface designs suitable for both the visible (532 nm) and NIR (1550 nm) bands. Such PT-symmetric metasurfaces can provide an alternative avenue to existing techniques [36-38] for effectively controlling a number of diffraction orders through surface-confined passive nano-features.

1.2. 1-D Hermitian PT symmetric Metasurfaces

To analyze the optical properties of a PT-symmetric metasurface, we assume that the complex refractive index $n(x) = f(x) + ig(x)$ is periodically modulated on the surface. Here $f(x)$ and $g(x)$ are periodic real functions having a spatial period L, representing the length of each unit cell on this

metasurface. In this regard, n(x) can be expressed through a Fourier series as follows;

$$n(x) = (a_0 + ia_0') + \frac{1}{2}\sum_{m=1}^{\infty}[(a_m + b_m') + i(a_m' - b_m)]\, e^{im\theta} +$$

$$\frac{1}{2}\sum_{m=1}^{\infty}[(a_m - b_m') + i(a_m' + b_m)]\, e^{-im\theta} \quad (1\text{-}1)$$

where $\theta = \frac{2\pi x}{L}$. In Eqn. (1-1), $\{a_m, b_m\}$ and $\{a'_m, b'_m\}$ represent the Fourier coefficients associated with the real f (x) and imaginary g (x) components of the complex refractive index distribution, respectively. The envisioned PT-symmetric metasurface is expected to be implemented solely using passive components, i.e., the imaginary component g (x) will introduce only loss.

Of interest would be to identify methods through which the negative (or positive) diffraction orders emanating from this PT-symmetric metasurface can be entirely suppressed while the remaining orders (positive or negative) can be enhanced. For this to occur one has to eliminate, for example, the negative orders $\exp(-im\theta)$ appearing in the Fourier series of Eqn. (1-1). This directly implies that $b'_m = a_m$ and $a'_m = -b_m$. From here, one obtains the following representations for f (x), g (x) that are necessary to suppress the negative orders.

$$f(x) = a_0 + \sum_{m=1}^{\infty}\{a_m \cos\left(m\frac{2\pi x}{L}\right) + b_m \sin(m\frac{2\pi x}{L})\}$$

$$g(x) = a_0' + \sum_{m=1}^{\infty}\{a_m \sin\left(m\frac{2\pi x}{L}\right) - b_m \cos(m\frac{2\pi x}{L})\} \quad (1\text{-}2)$$

Equation (1-2) show that this is only possible as long as the real and imaginary parts of the refractive index are intertwined through common coefficients a_m, b_m. This index distribution is PT-symmetric, when the terms in Eqn. (1-2) associated with the a_m, b_m coefficients are considered separately. Similarly, one can eliminate the positive orders $e^{im\theta}$ provided that $b'_m = -a_m$ and $a'_m = b_m$, in which case the following relations hold true.

$$f(x) = a_0 + \sum_{m=1}^{\infty}\{a_m \cos\left(m\frac{2\pi x}{L}\right) + b_m \sin(m\frac{2\pi x}{L})\}$$

$$g(x) = a_0' + \sum_{m=1}^{\infty}\{-a_m \sin\left(m\frac{2\pi x}{L}\right) + b_m \cos(m\frac{2\pi x}{L})\} \quad (1\text{-}3)$$

Equations (1-2), (1-3) indicate that, in order to eliminate either the negative or the positive orders, f (x) and g (x) must be PT-symmetric partners. The diffractive configuration considered here, essentially acts like a phase screen with a phase transmission function of the form $\exp(ik_0 n(x)d)$, where d represents an effective depth. Equations (1-1 to 1-3) provide a methodology for designing such unidirectional metasurfaces. Once the subwavelength surface elements are positioned on the surface in a PT-symmetric fashion, finite element simulations (FEM) are then used to further optimize the performance of this arrangement.

In general the allowed diffraction orders associated with this metasurface system can be determined from $\vec{k}_{diff,tan} = \vec{k}_{inc,tan} + m\vec{G}_{lat}$, where $\vec{G}_{lat}$ is the reciprocal lattice vector of this 1-3 D lattice, and $\vec{k}_{inc,tan}$ and $\vec{k}_{diff,tan}$ are the tangential components of the incident and diffracted wave vectors, and m is the diffraction order. Since we are investigating this system in transmission mode, the previous relation implies that $n_2 \sin\beta_m = n_1 \sin\alpha + m(\lambda_0/L)$, where n_1, n_2 are the refractive indices of the incident and transmitted media, α is the angle of incidence, β_m is the diffraction angle and λ_0 is the free space wavelength.

1.2.1 PT symmetric designs

Based on the aforementioned analysis we investigate the optical properties of the structures shown in Fig. 1-1 and 1-2 for the wavelengths of 1550 and 532 nm, respectively. These configurations were conceived by matching the Fourier coefficients in a discrete fashion. These systems were subsequently optimized using finite element methods. For the 1550 nm design as

shown in Fig. 1-1, we employ silicon as the transparent material and nickel for loss. On the other hand, the 532 nm design (see Fig. 1-2) is based on sapphire (as the transparent medium) and again utilizes nickel for loss. In general, the real part of the refractive indices of the transparent and lossy materials are here approximately equal in order to satisfy the PT-symmetry condition. We would like to note that, while the imaginary component in our designs is not exactly antisymmetric, their response is still dictated to a great extent by PT symmetry. This is due to the fact, that PT symmetric related processes can be quite robust and hence can tolerate environments, where this symmetry is not exactly satisfied. For both wavelengths, we assume normal incidence and a TE-polarization, i.e., the electric field is parallel to the 1-D stripes of this metasurface. Under these conditions, the designs shown in Fig. 1-1 and 1-2 support up to six transmission orders.

In order to evaluate the performance of these configurations, we consider an extinction ratio, defined as the ratio between the diffraction efficiencies associated with the positive orders to that of the negative orders and vice versa. The FEM results corresponding to the aforementioned structures are shown in Fig. 1-1 and 1-2. As expected, if no loss is incorporated in the system (Hermitian case), light propagates symmetrically after this metasurface, as shown in Fig. 1-1(c) and 1-2(c). In this case the positive and negative orders are exactly the same. This scenario changes once loss from nickel is introduced. The resulting field distributions and Poynting vector plots are shown in Fig. 1-1(d), 1-2(d). Under these conditions, the light is skewed in one direction, towards the lossy side. The physical reason behind this symmetry-breaking behavior has to do with the redistribution of energy flow within the system. In other words, the Poynting vector now develops an additional transverse component that is needed to supply energy to the lossy domains.

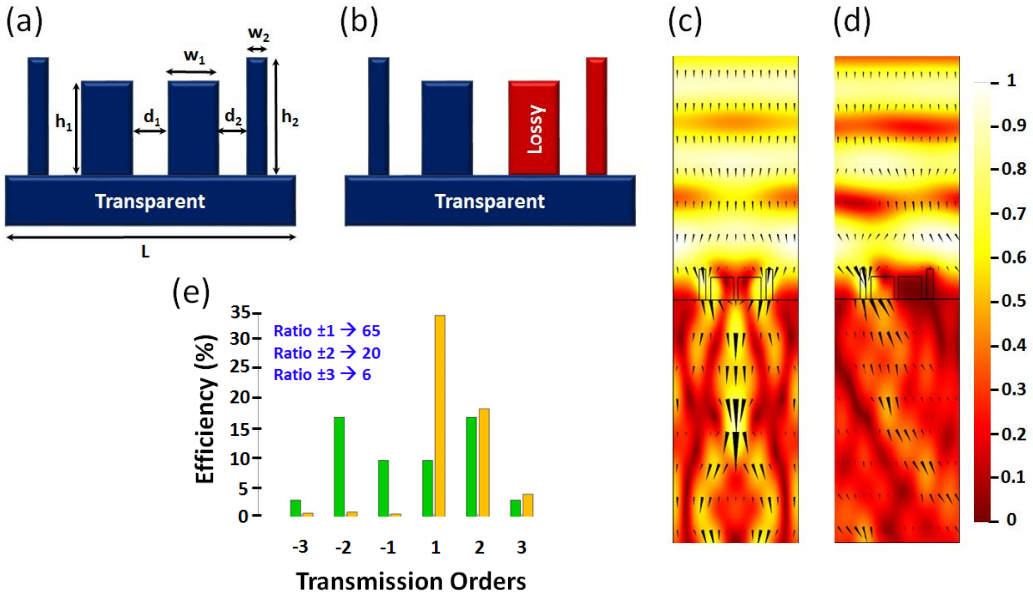

Figure 1-1: 1-D metasurface design for 1550 nm with dimensions L = 1520 nm, h_1 = 230 nm, h_2 = 310 nm, w_1 = 280 nm, w_2 = 80nm, d_1 = 50nm, d_2 = 60nm. The transparent material is silicon with a refractive index n_{Si} = 3.4757 [38], while the lossy medium used is nickel with a refractive index n_{Ni} = 3.4378 − 6.7359i [39]. (a), (c) Hermitian case (when no loss is incorporated) and corresponding near-field and Poynting vector (arrow plots), (b), (d) PT-symmetric case (when loss is introduced) and corresponding near-field and Poynting vector distributions, (e) transmission order efficiencies for the Hermitian case (green) and PT-symmetric case (yellow) and extinction ratios between the positive and corresponding negative orders (blue).

For the 1550 nm design, the FEM simulations show that the extinction ratio between the ± 1orders is approximately 65 (18 dB), for the ± 2 is 20 (13 dB) and for the ± 3 the extinction ratio is approximately 6 [see Fig. 1-1(e)]. On the other hand, the design intended for 532 nm exhibits optimum performance for the ± 2 orders where the extinction ratio is 1800 or 33 dB. Meanwhile for the remaining two orders it ranges between 62 to 16 [see Fig. 1-2(e)]. In essence, these metasurface designs can effectively suppress the positive (negative) orders by exploiting the symmetry-breaking induced by PT symmetry.

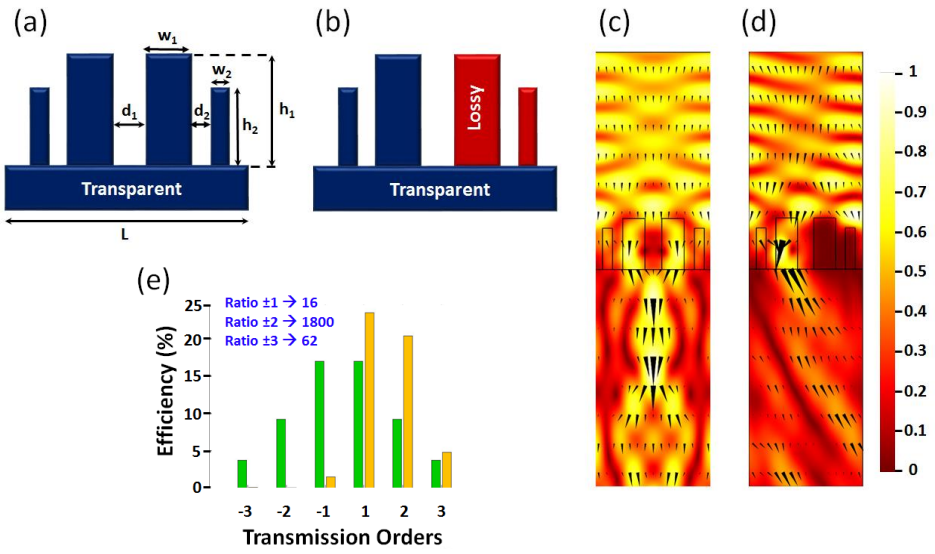

Figure 1-2: 1-D metasurface design for 532 nm with dimensions L = 1050 nm, h_1 = 470 nm, h_2 = 380 nm, w_1 = 200 nm, w_2 = 90nm, d_1 = 150 nm, d_2 = 90nm. The transparent material is sapphire with refractive index n_{Al2O3} = 1.7718 [40], while the lossy material is nickel with refractive index n_{Ni} = 1.7764–3.776i [39]. (a), (c) Hermitian case (when no loss is incorporated) and corresponding near-field distribution and Poynting vector (arrow plots), (b), (d) PT-symmetric case (when loss is introduced) and corresponding near-field distribution and Poynting vector plot, (e) transmission order efficiencies for the Hermitian case (green) and PT-symmetric case (yellow) and extinction ratios between the positive and corresponding negative orders (blue).

1.3. 2-D Hermitian PT symmetric Metasurfaces

Following a rationale similar to that used in the 1-D case, in order to identify designs capable of eliminating diffraction orders in certain directions, while enhancing the remaining orders, we again employ Fourier analysis. In this case, the complex refractive index distribution n (x, y) = f (x, y) + ig (x, y) is to be periodic on the surface of the PT-symmetric structure, where f (x, y), g (x, y) are real periodic functions, with spatial periods L_x, L_y along the x-axis and y-axis respectively. The parameters L_x, L_y physically represent the dimensions of each unit cell on the

PT-symmetric metasurface in the x-direction and y-direction, correspondingly. By expanding n (x, y) into a 2-D Fourier series we obtain,

$$n(x,y) = \frac{1}{2}\sum_{m,l=0}^{\infty}\{[\left(a_{m,l} + c'_{m,l}\right) + i(a'_{m,l} - c_{m,l})]\, e^{im\theta_x}e^{il\theta_y} + [\left(a_{m,l} - c'_{m,l}\right) + i\left(a'_{m,l} + c_{m,l}\right)]e^{-im\theta_x}e^{-il\theta_y} + \left[\left(b_{m,l} + d'_{m,l}\right) + i\left(b'_{m,l} - d_{m,l}\right)\right]e^{im\theta_x}e^{-il\theta_y} + \left(b_{m,l} - d'_{m,l}\right) + i\left(b'_{m,l} + d_{m,l}\right)]e^{-im\theta_x}e^{il\theta_y}\} \quad (1\text{-}4)$$

where $\theta_x = \frac{2\pi x}{L_x}$, $\theta_y = \frac{2\pi y}{L_y}$. In Eqn. (1-4) $\{a_{m,l}, b_{m,l}, c_{m,l}, d_{m,l}\}$ and $\{a'_{m,l}, b'_{m,l}, c'_{m,l}, d'_{m,l}\}$ are the Fourier coefficients of the functions f (x, y) and g (x, y) , respectively.

In order to achieve a unidirectional deflection, i.e., a suppression of the diffraction orders in all three quadrants ($e^{-im\theta_x}e^{il\theta_y}, e^{-iml}e^{-il\theta_y}, e^{im\theta_x}e^{-il\theta_y}$) except for the first ($e^{im\theta_x}e^{il\theta_y}$), the relations $c'_{m,l} = a_{m,l}$, $a'_{m,l} = -c_{m,l}$, $b_{m,l} = d'_{m,l} = b'_{m,l} = d_{m,l} = 0$ should hold. Consequently, f (x, y), g (x, y) take the form;

$$f(x,y) = \sum_{m,l=0}^{\infty}\{a_{m,l}\cos\left(m\frac{2\pi x}{L_x} + l\frac{2\pi y}{L_y}\right) + c_{m,l}\sin\left(m\frac{2\pi x}{L_x} + l\frac{2\pi y}{L_y}\right)\}$$

$$g(x,y) = \sum_{m,l=0}^{\infty}\{a_{m,l}\sin\left(m\frac{2\pi x}{L_x} + l\frac{2\pi y}{L_y}\right) - c_{m,l}\cos\left(m\frac{2\pi x}{L_x} + l\frac{2\pi y}{L_y}\right)\} \quad (1\text{-}5)$$

From Eqn. (1-5), we conclude that the index distribution n (x, y) is PT-symmetric, when the $a_{m,l}$, $c_{m,l}$ terms in the equation are separately considered. These coefficients were imposed on 2-D scattering configurations and optimized using FEM.

We next define the reciprocal lattice vectors as $\vec{G}_1 = 2\pi\frac{(\vec{a}_2\times\vec{z})}{\vec{a}_1.(\vec{a}_2\times\vec{z})}$ and $\vec{G}_2 = 2\pi\frac{(\vec{z}\times\vec{a}_1)}{\vec{a}_1.(\vec{a}_2\times\vec{z})}$, where $\vec{a}_1, \vec{a}_2$ are the unit cell vectors, while $\vec{z}$ is the unit vector along the z-axis, normal to the considered unit cell. The diffraction orders supported by the metasurface system can be determined from

$\vec{k}_{diff,\parallel} = \vec{k}_{inc,\parallel} + m\vec{G}_1 + l\vec{G}_2$, where the pair of integers [m, l], represents the transmission order, $\vec{k}_{diff,\parallel}$ and $\vec{k}_{inc,\parallel}$ denote the tangential components of the diffracted and incident wave vector, respectively. The normal component of the diffracted wave vector can be found from $\vec{k}_{diff,\perp} = \sqrt{(k_0 n_2)_2 - \left|\vec{k}_{diff,\parallel}\right|^2}\vec{z}$, where n_2 is the refractive index in the transmission medium. Finally, the corresponding elevation and azimuth propagation angles can be evaluated from $\theta = \cos^{-1}(\frac{k_{diff,z}}{k_0 n_2})$ and $\varphi = \tan^{-1}(\frac{k_{diff,y}}{k_{diff,x}})$ respectively, where $k_{diff,x}, k_{diff,y}$ and $k_{diff,z}$ are the x–, y– and z– components of the diffracted wave vector.

1.3.1 H-like designs

We next consider the diffraction behavior of a 2-D PT symmetric metasurface comprised of H-like elements, as shown in Fig. 1-3. Such metasurface is locally and globally PT-symmetric around a central point. These designs are investigated for the wavelengths of 1550 and 532 nm using FEM. As in the 1-D case, the materials considered here are silicon and nickel (1550 nm), while for the 532 nm design are sapphire and nickel. Given that each H-like element is passively PT-symmetric [see Fig. 1-3(a)], one expects that the entire metasurface will exhibit this same symmetry. In performing FEM simulations, we assume normal incidence with the electric field linearly polarized along the y-axis. Based on the chosen dimensions and the wavelength of operation, we deduce that these configurations support up to eight transmission orders. For the 1550 nm design, the extinction ratio is 65 (18 dB) between the [1, 1] and [− 1, − 1] transmission orders [see Fig. 1-3(c)] when the loss of nickel is taken into account (PT-symmetric metasurface). This is in stark contrast to its corresponding Hermitian design, where the ratio is unity and the

transmitted field distribution is completely symmetric. This same ratio is approximately 11 for the [0, ± 1] orders and 6 for the [± 1, 0] orders. In Fig. 1-3(c) an overall deflection of the near field is observed in the y = 0, x = 0 and x = y planes, which stems from the significant asymmetry in the diffraction efficiencies of the transmission order pairs {[1, 0], [− 1, 0]}, {[0, 1], [0, − 1]}, {[1, 1], [− 1, − 1]}. This strong asymmetry arises from the fact that the lossy material is mostly present in the first quadrant, while it is completely absent from the third. On the other hand, even though the lossy material is equally distributed in the second and fourth quadrants it still leads to reduced efficiencies to the transmission orders [− 1, 1], [1, − 1] that happen to be below 1%.

Similar results are obtained for the 532 nm design. The extinction ratio between the [1, 1] and [− 1, − 1] transmission orders reaches up to a value of 65, while for the [0, ± 1] orders and [± 1, 0] orders is 12 and 10 respectively as shown in Fig. 1-3(d). Field distributions and Poynting vector plots, as obtained from FEM, are also shown in this same figure. We know that this suppression/enhancement behavior is a direct result of the judicious distribution of transparent and lossy elements on this metasurface. As we will see in the next section, such diffractive elements can be arranged in a different manner, while still retaining the overall PT-symmetric characteristics.

1.3.2 Diatomic oblique Bravais lattice designs

In this section we use an oblique Bravais PT lattice design in order to achieve unidirectional deflection in the diffraction orders of this metasurface. To do so, we utilize a diatomic configuration, similar to that shown in Fig. 1-4. The various quantities associated with this system are L_a, L_b, d and φ_{lat} [see Fig. 1-4(a)].

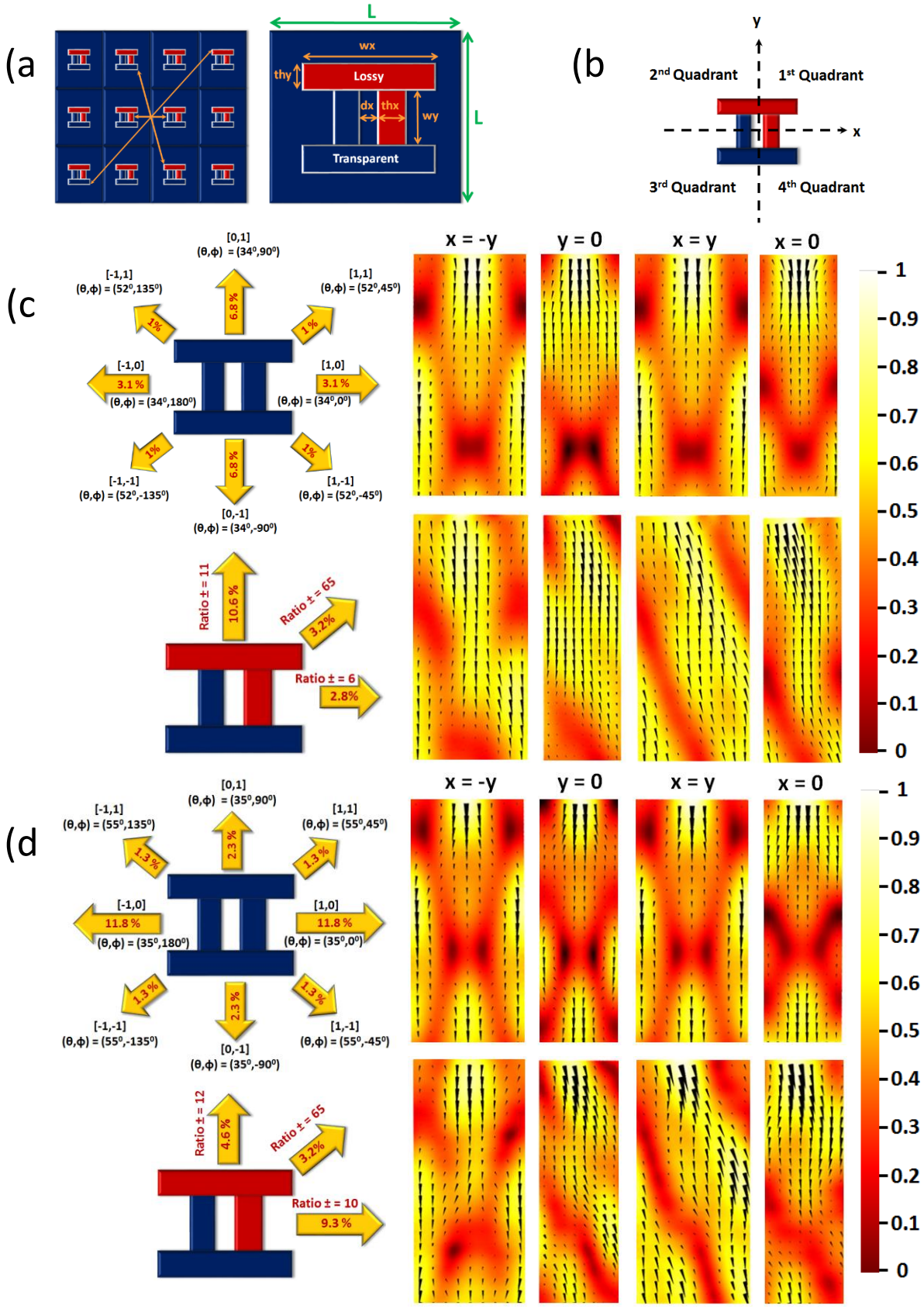
(a
L
wx
thy
Lossy
dx
thx
wy
L
Transparent
(b
y
2nd Quadrant
1st Quadrant
x
3rd Quadrant
4th Quadrant
(c
[0,1]
(θ,ϕ) = (34°,90°)
[-1,1]
(θ,ϕ) = (52°,135°)
[1,1]
(θ,ϕ) = (52°,45°)
6.8 %
1%
1%
[-1,0]
3.1 %
(θ,ϕ) = (34°,180°)
[1,0]
3.1 %
(θ,ϕ) = (34°,0°)
1%
1%
[-1,-1]
(θ,ϕ) = (52°,-135°)
6.8 %
[1,-1]
(θ,ϕ) = (52°,-45°)
[0,-1]
(θ,ϕ) = (34°,-90°)
Ratio ± = 11
10.6 %
Ratio ± = 65
3.2%
Ratio ± = 6
2.8%
x = -y
y = 0
x = y
x = 0
1
0.9
0.8
0.7
0.6
0.5
0.4
0.3
0.2
0.1
0
(d
[0,1]
(θ,ϕ) = (35°,90°)
[-1,1]
(θ,ϕ) = (55°,135°)
[1,1]
(θ,ϕ) = (55°,45°)
2.3 %
1.3 %
1.3 %
[-1,0]
11.8 %
(θ,ϕ) = (35°,180°)
[1,0]
11.8 %
(θ,ϕ) = (35°,0°)
1.3 %
1.3 %
[-1,-1]
(θ,ϕ) = (55°,-135°)
2.3 %
[1,-1]
(θ,ϕ) = (55°,-45°)
[0,-1]
(θ,ϕ) = (35°,-90°)
Ratio ± = 12
4.6 %
Ratio ± = 65
3.2%
Ratio ± = 10
9.3 %
x = -y
y = 0
x = y
x = 0
1
0.9
0.8
0.7
0.6
0.5
0.4
0.3
0.2
0.1
0

Figure 1-3: H-like design: (a) H-element and corresponding lattice, (b) coordinate plane and quadrants, (c) FEM results of the transmission order efficiencies, normalized near-field distributions and Poynting vector plots for the 1550 nm design with dimensions L = 800 nm, w_x = 520 nm, thx = 90 nm, w_y = 160 nm, thy = 180 nm, dx = 110 nm, and h = 160 nm. The transparent material is silicon and the lossy material is nickel as in Fig. 1-1, (d) Same as in (c), for the 532 nm design, with dimensions L = 520 nm, w_x = 410 nm, thx = 100 nm, w_y = 110 nm, thy = 90 nm, dx = 40 nm, and h = 160 nm. The transparent material is sapphire, while the lossy material is nickel as in Fig. 1-2. In (c) and (d), the brackets [m, l] denote transmission orders.

In its Hermitian manifestation, such a honeycomb system will symmetrically excite the diffraction orders. Even if PT symmetry is passively imposed and therefore some of the orders are eliminated [see Fig. 1-4(c)], the diffraction is still angularly balanced under normal incidence. Hence, in order to enhance some of the orders at the expense of others, the PT diatomic cell must assume an oblique shape with an angle φ_{lat} above 30°. This latter necessity arises from geometric considerations. More specifically, the honeycomb lattice as shown in Fig. 1-4(b) is characterized by the relations $L_a = 2L_b\cos(\varphi_{lat})$, $L_b = 2d\cos(\varphi_{lat})$ and φ_{lat}= 30°. Given the underlying symmetry of a honeycomb lattice, even in the PT-symmetric case, we don't observe directional scattering towards a particular angular sector. In order to break this spatial symmetry, we have relaxed the requirement $L_b = 2d\cos(30°)$ to $L_b/(2d\cos(\varphi_{lat})) > 2$. FEMs indicate that under these conditions, orders propagating in a particular angular sector can be enhanced, while the rest are eliminated. In the examples that follow we use φ_{lat}= 60°. Note that under this oblique transformation, the PT-symmetry condition is still retained in each cell and in the lattice in general.

For the sake of comparison, two designs are again analyzed at 1550 and 532 nm. In both cases, the same materials are used as in Section 1.3.1. Here we assume normal incidence, with the electric field linearly polarized in the horizontal direction [azimuthal plane φ = 0, Fig. 1-5(b)]. Under these

conditions, the simulated structures support six transmission orders.

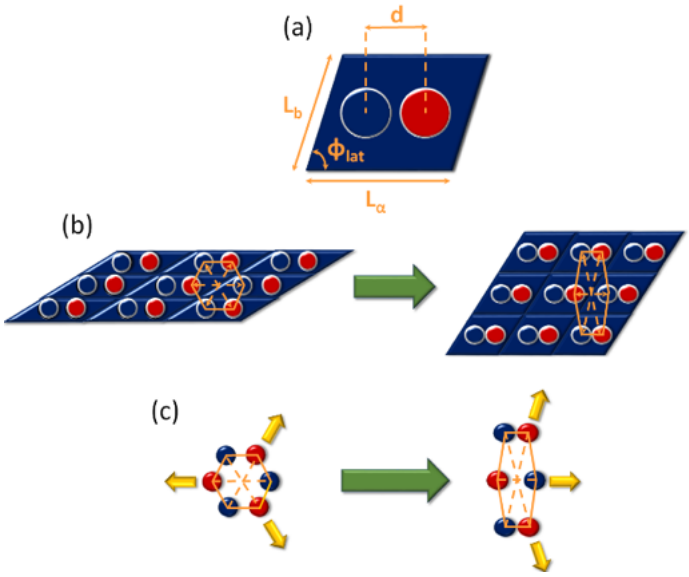

Figure 1-4: (a) Unit cell of the diatomic oblique Bravais lattice, (b) geometric transformation from the honeycomb lattice (left), to the diatomic oblique Bravais lattice (right), and (c) corresponding transmission orders.

The 1550 nm design, as shown in Fig. 1-5(c), the extinction ratio between the rightward [1, 1], [1, 0] and the respective leftward orders [− 1, − 1], [− 1, 0] is approximately 40 (16 dB) when loss is employed (PT-symmetric case). Such an asymmetry in the diffraction efficiencies justifies the strong bending of the near field in the azimuthal planes φ= 0, φ= 30° and φ= -30°. On the other hand, in the azimuthal plane φ= 90°, no deflection occurs. The diffraction efficiencies of the transmission orders [0, ± 1] propagating in the same plane, are much less than 1% and thus do not alter the propagation of the power flow. Similar effects are observed for the 532 nm design [see Fig. 1-5(d)]. More specifically, in the PT-symmetric case the extinction ratios between the rightward [1, 1], [1, 0] and the respective leftward orders [− 1, − 1], [− 1, 0] scales up to 30 (15 dB), which results in the asymmetric scattering of the near field in the azimuthal planes φ= 0, φ= 30° and φ= -30°. Instead in the azimuthal plane φ= 90°, the scattering pattern remains symmetric

since the diffraction efficiencies of the propagating orders [0, ± 1] are reduced to much below 1%.

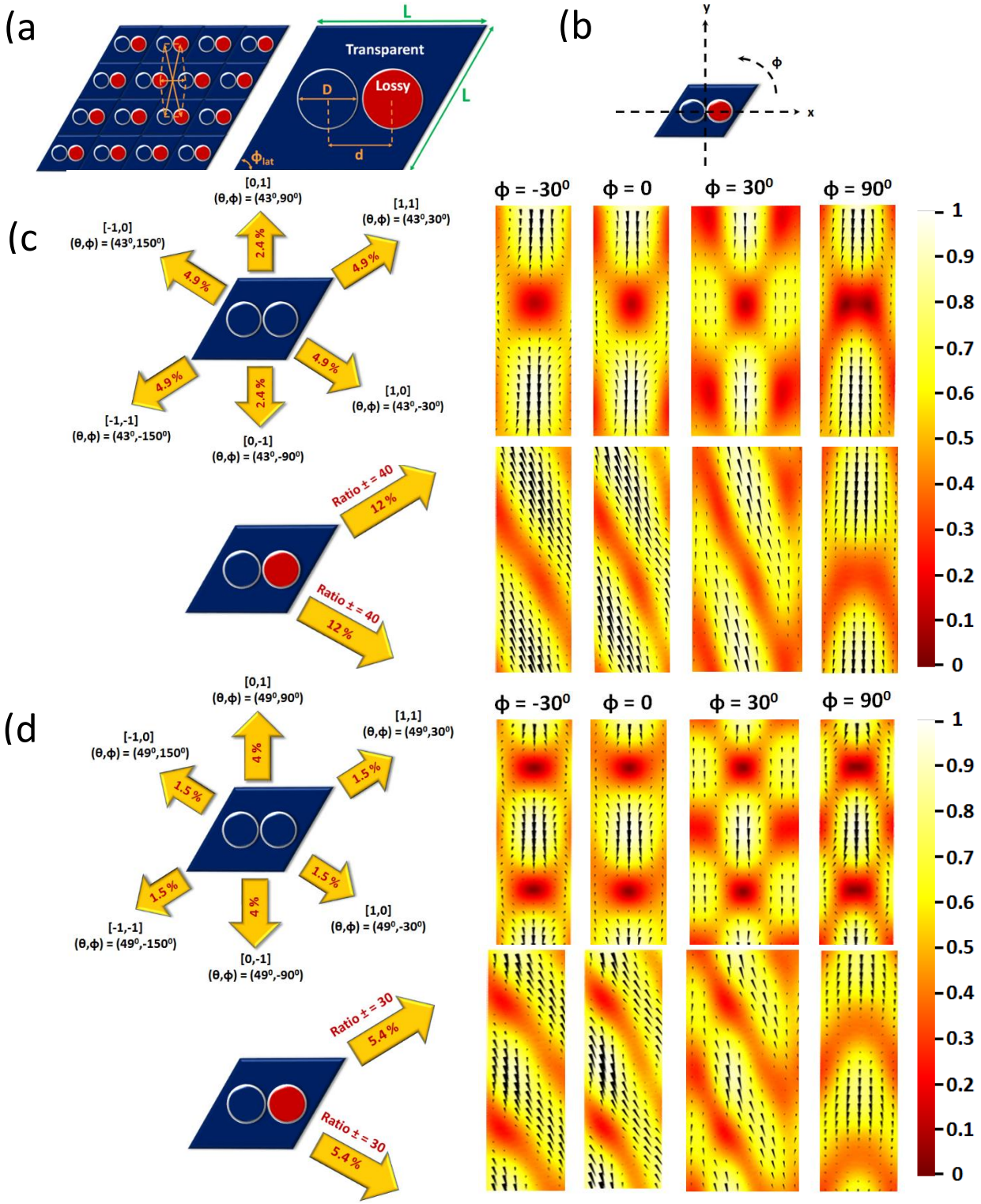

Figure 1-5: Oblique diatomic Bravais lattice design: (a) unit cell and corresponding lattice, (b) coordinate plane, (c) FEM results of the transmission order efficiencies, normalized near-field distributions and Poynting vector plots for the 1550 nm design with dimensions L = 750 nm, D = 260 nm, d = 290 nm, h = 330 nm, and φ_{lat} = 60°. The materials and respective refractive indices are the same as in Fig. 1-1, (d) FEM results of the diffraction efficiencies, normalized near-field distributions and Poynting vector plots for the 532 nm design with dimensions L = 460 nm, D = 160 nm, d = 180 nm, h = 330 nm, and φ_{lat} = 60°. The materials and respective refractive indices are the same as in Fig. 1-2. In (c), and (d), the brackets [m, l] denote transmission orders.

1.4 Summary

In conclusion, we have shown that by merging two recently developed concepts, those associated with PT-symmetry and metasurface optics, one can design systems with highly directional scattering characteristics. Hermitian PT-symmetry can be readily introduced in these arrangements by judiciously exploiting loss. In this study, all-passive one-dimensional and two-dimensional metasurface designs have been investigated. In two-dimensional settings, we have shown that PT symmetry can be established by employing either H-like diffractive elements or diatomic oblique Bravais lattices. PT-symmetric metasurfaces can provide an alternative avenue to existing techniques for effectively manipulating the resulting diffraction orders through surface-confined passive nano-features.

CHAPTER 2: FLEXIBLE ROADBAND PT SYMMETRIC METASURFACES

2.1 Introduction

In the last few years, optics has witnessed the emergence of two interesting fields namely metasurfaces and parity-time symmetry. Optical metasurfaces are engineered artificial structures that provide unique responses to electromagnetic waves, absent in natural materials [15,16,18,19]. Optical metasurfaces are known for their reduced dimensionality, subwavelength, consequently lower losses are anticipated. Such prevailing optical characteristics alleviated some of the conventional constraints imposed by the electromagnetic response of natural existing materials. Accordingly, a new class of unachievable applications and devices has been realized. Some of those applications are controllable surfaces, cloaking, ultrathin lens, terahertz switches, etc [21,22,45-47]. One appealing aspect of optical metasurfaces, which differentiates them from their 3D counterparts (metamaterials), is their adaptability to on-chip nanophotonics devices, hence new possibility for future applications such as imaging, optoelectronics and ultrafast information technologies.

Another paradigm of a new class of artificial materials is parity-time (PT) symmetric materials, which are known as photonic synthetic matter. PT symmetry has emerged from quantum mechanics when a new class of non-Hermitian Hamiltonian quantum systems was highlighted to have real eigenvalues, hence Hermiticity of the Hamiltonian is not an essential condition to the existence of real eigenvalues [1]. This is defined succinctly in the following condition $V(\boldsymbol{r}) = V^*(-\boldsymbol{r})$. Due to the absence of physical systems in quantum mechanics with such non-Hermitian Hamiltonians, the PT symmetry was pursued in optics motivated by the resemblance between the

scalar Helmholtz equation and time-independent Schrödinger equation. Thereby, the correspondence between the potential energy in quantum mechanics and the permittivity in optics demands the ensuing condition $\varepsilon(\boldsymbol{r}) = \varepsilon^*(-\boldsymbol{r})$, which implies that the refractive index must be symmetric in coordinate space while the imaginary (namely gain or loss) part must be odd. Another notable feature of PT-symmetric optical systems is their ability to exhibit a phase transition (spontaneous PT-symmetry breaking). PT symmetry has been extensively investigated experimentally and theoretically in different number of physical systems, such as electronic circuits, nuclear magnetic resonances, optics, metamaterials, microwaves cavities, mechanical oscillators, and superconductors, to mention a few [2-13,42-44]. Remarkably, optical systems display the resourceful platform to study the rudiments of PT symmetry and its potential applications.

In this chapter, an experimental realization followed by theoretical modeling of a first broadband optical metasurfaces united with PT-symmetry on flexible polymer (polyimide) is discussed. As shown later, PT-symmetry is introduced in the studied optical system through an engineered amplitude and phase modulation that are levied on the surface. Previous works have reported bulk non-Hermitian 1-D gratings, nevertheless, these notions are extended here to more complex configurations with particular accentuation on optical PT-symmetric metasurfaces. The proposed PT-symmetric structures attenuate the diffraction orders in the undesired directions, while enhancing the remaining orders. In this study, we present all-passive 2-D metasurface configuration appropriate for the visible (400 – 600 nm) band. In addition, the PT-symmetric metasurfaces is fabricated on another substrate (sapphire), and in both cases, the experimental findings have excellent matching with the theoretical models. The aforementioned optical system

can offer a different avenue to current techniques that aim at controlling a number of diffraction orders through surface-confined passive nano-features [14, 26,27,30-33].

2.2 Modified design of 532nm PT-symmetric Diatomic Oblique Bravais Lattice

In this chapter, we primarily focus on the fabrication and characterization of the PT-symmetric Diatomic Oblique Bravais Lattice for 532 nm. In chapter 1, we were interested in the bending of the field in the sapphire substrate. For such structure given the dimensions of the unit cell, the incidence angle and the wavelength of operation, no diffraction orders could be supported in air. The latter can be explained straightforwardly from the diffraction equation. Therefore, no bending of the field can be observed in the air, since the primary reason for the bending is the imbalance of the efficiency of the supported diffraction orders. In the new structure, given we want to observe directive scattering in air; we have to increase the unit cell dimensions so as diffraction orders can be supported in air. Then we optimize the structure dimensions to obtain the maximum imbalance in the efficiency of the corresponding diffraction orders in air. The latter results in the bending of the field in air.

In order to observe the diffraction orders, few modifications, to the studied structure PT-symmetric Diatomic Oblique Bravais lattice in chapter 1 was required. The modifications applied to the Sapphire is shown in Table 2-1. The parameters in the previous chapter are also provided to highlight the proposed changes. For the polyimide substrate the parameters used are as follows; unit cell 690 nm, cylinder diameter 160 nm, cylinder height 370 nm with 90 nm buried in the substrate and 280 nm above the polymer and finally the center-to-center separation between the cylinders is 210 nm. Moreover, the work is extended to involve the study of the behavior in a

flexible polymer, polyimide. The substrate choice depends mainly on its transparency in the studied optical band. For example, for the 1550 nm, silicon is chosen for being transparent. For visible band, the sapphire and polyimide are transparent. However, for wavelength below 430 nm, the polyimide becomes lossy, thus the efficiencies might change for sub 430 nm wavelengths.

Table 2-1: Modified structural parameters for the PT symmetric Diatomic Bravais lattice on sapphire substrate.

	Unit Cell / nm		Cylinder diameter / nm		Cylinder height / nm		Cylinder (center to center) separation / nm	
	Old	New	Old	New	Old	New	Old	New
Sapphire	460	**690**	160	**160**	180	**290**	180	**210**

2.2.1 Numerical Analysis

Using the parameters shown in Table 2-1, near field simulation were performed exhibiting the broadband symmetry breaking in the two metasurface. The field distribution in the azimuthal planes $\varphi = 30^0, 150^0$ for both the Hermitian (lossless) and PT-symmetric case (lossy) is calculated over three different wavelengths, 430 (purple), 530 (green) and 580 (yellow) nm. Both in the case of Sapphire and flexible polymer, the surface pillars are nickel and alumina. The results are shown in Fig. 2-1 and 2-2. Moreover, Using the Finite Element Method (FEM) the transmission order efficiencies of the six diffraction orders as described in chapter 1 (Fig. 1-5) were calculated. The six diffraction orders are [1, 1] (**1**), [1, 0] (**2**), [0, 1] (**3**), [-1, -1] (**4**), [-1, 0] (**5**), and [0, -1] (**6**). The results for the 6 orders were summarized in Table 2-2 and Table 2-3, for the sapphire and the polymer respectively. The efficiencies shown are for both the Hermitian/Passive and the PT metasurfaces.

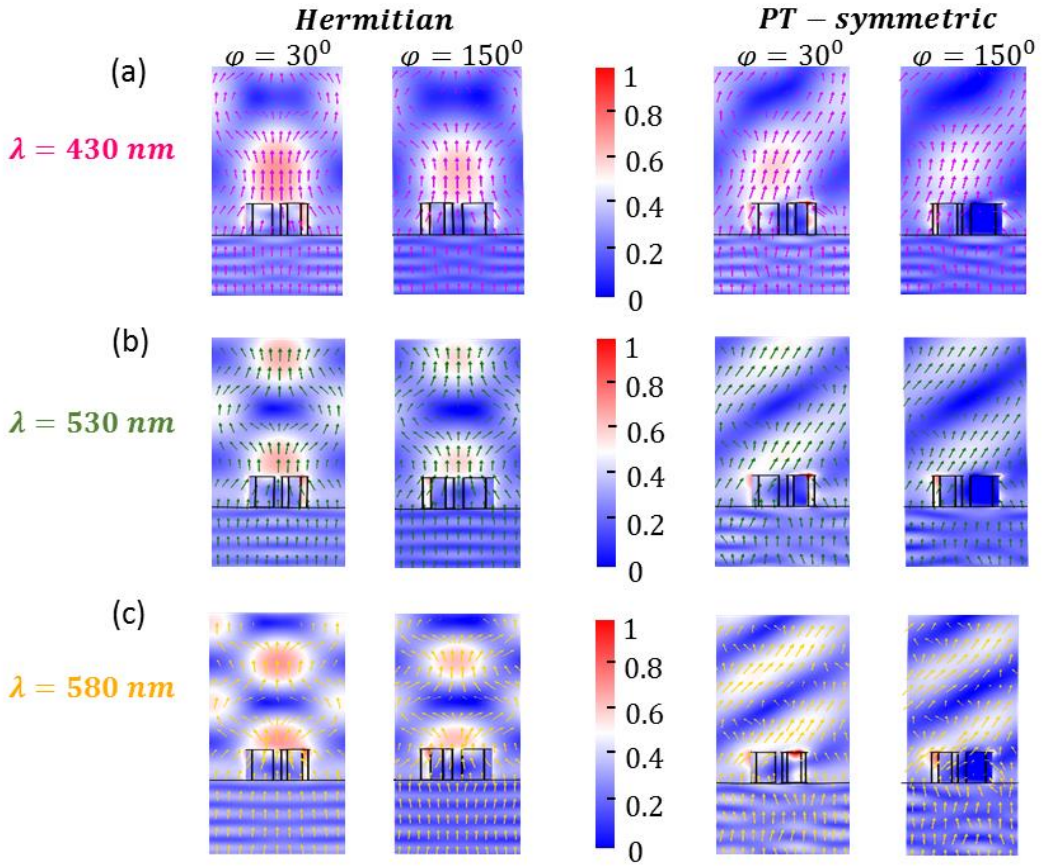

Figure 2-1: The field distribution of the sapphire substrate (Hermitian and PT-symmetric) at different wavelengths; (a) 430 nm, (b) 530 nm, (c) 580 nm.

Table 2-2: Transmission efficiency of the six diffraction disorder calculated for the sapphire substrate by FEM.

Diffraction orders	Hermitian metasurface / %			PT metasurface / %		
	430 nm	530 nm	580 nm	430 nm	530 nm	580 nm
1	2.75	1.89	1.93	3.6	3.2	3.1
2	2.75	1.89	1.93	3.6	3.2	3.1
3	7.85	2.79	1.34	2	0.55	0.18
4	2.75	1.89	1.93	0.1	0.15	0.2
5	2.75	1.89	1.93	0.1	0.15	0.2
6	7.85	2.79	1.34	2	0.55	0.18

Both structures are almost identical, in the sense of geometry and dimensions of the cylindrical pillars, periodicity of the unit cell, dimensionality of the unit cell and the refractive indices. The sapphire refractive index is 1.77 at 532 nm. As for the polyimide the refractive index is close to 2.0 at the same wavelength, thus a minor modification to the height was proposed. The height of the pillars in the flexible metasurface is 380 nm, unlike the 290 nm for sapphire.

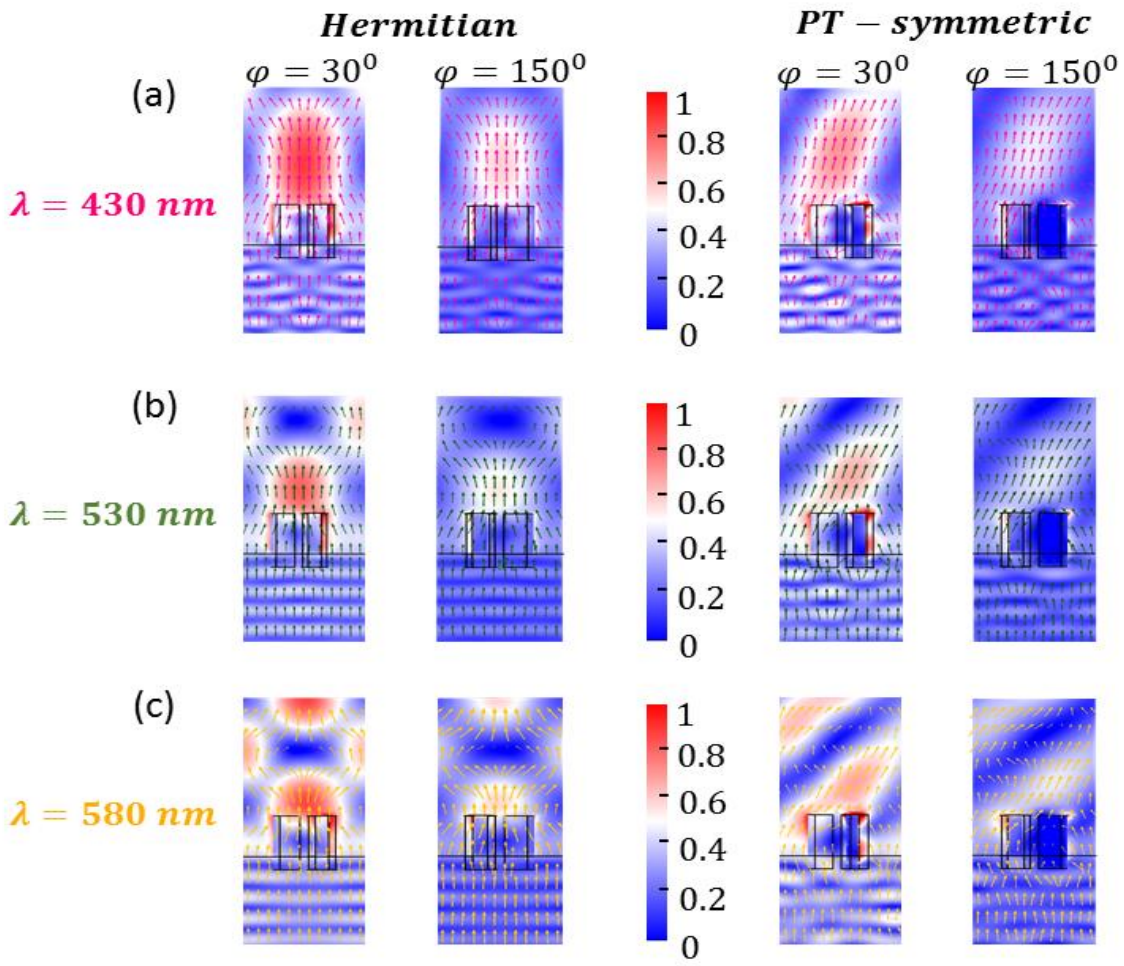

Figure 2-2: The field distribution of the Polyimide substrate (Hermitian and PT-symmetric) at different wavelengths; (a) 430 nm, (b) 530 nm, (c) 580 nm.

Table 2-3: Transmission efficiency of the six diffraction disorder calculated by FEM for the polymer substrate for the both Hermitian and PT symmetric metasurface.

Diffraction orders	Hermitian metasurface / %			PT metasurface / %		
	430 nm	530 nm	580 nm	430 nm	530 nm	580 nm
1	2.06	1.53	1.56	4.34	3.61	3.32
2	2.06	1.53	1.56	4.34	3.61	3.32
3	6.17	2.13	1.09	2.79	0.66	0.4
4	2.06	1.53	1.56	0.09	0.18	0.12
5	2.06	1.53	1.56	0.09	0.18	0.12
6	6.17	2.13	1.09	2.79	0.66	0.4

2.3 Fabrication instruments

This section encompasses various techniques, instrumentation and recipes employed for the fabrication of nanostructures. The discussed information is applicable to both solid and flexible substrates. The aim of this chapter is to highlight the fabrication tools utilized for the achievement of nanomaterials. The fabrication was primarily executed at the Nano Research Facility (NRF) at University of Florida (UF), Gainesville, followed by certain steps performed at CREOL clean room. The various experimental setups used during fabrication are discussed below briefly.

A spin coater is one of the basic tool employed in fabrication of nanostructured / semiconductor devices. A simple process designed to achieve thin and uniform coating of materials on a substrate from a few millimeters square [48]. The typical materials used with this system are nanomaterials, photoresists, insulators, organic semiconductors, metals etc. The current models employ high spinning speeds equipped with high airflow, resulting in high consistency of deposition and fast drying times. Figure 2-3 showcase a typical spin coater, with the arrow pointing at the head used

to place sample, the sample is secured at the spinning head by creating vacuum.

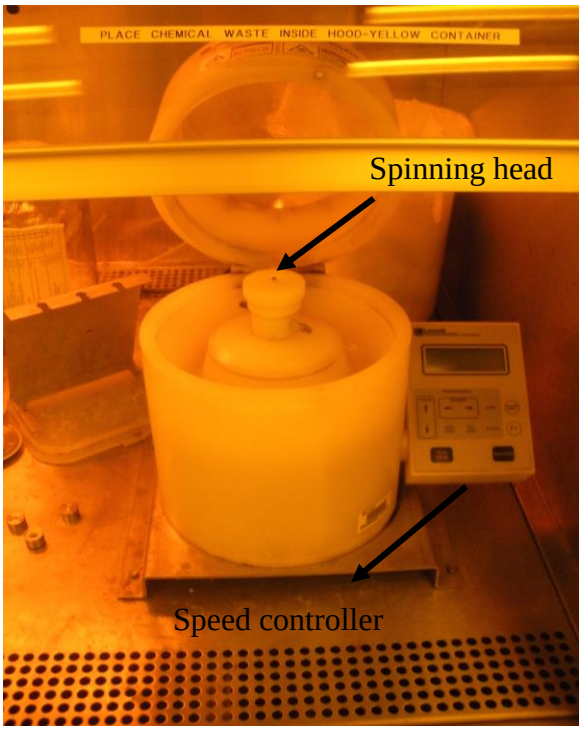

Figure 2-3: Spin coating setup with the parameter control.

Electron Beam (e-beam) deposition machine is a powerful technique designed to evaporate / deposit difficult materials especially that require high temperatures, like Gold or titanium or ceramics as in our case Alumina. The technique is more formally known as Electron beam physical vapor deposition (EBPVD) a form of physical vapor deposition methods. As opposed to conventional deposition vacuum chambers based on resistive thermal evaporation technique, in e-beam deposition setup an accelerated magnetically focused beam of electrons is directed at a crucible of the desired deposition materials. Upon evaporation induced because of the energy/heat from the beam, the material coat the substrate. The model available for the current recipe in NRF UF is 4 pocket 15cc e-beam, with one 3-inch DC sputter source and substrate heater (Fig. 2-4). The deposition rate in this process can be as low as 1 nm per minute to as high as few micrometers

per minute. Whereas, in CREOL, a TEMESCAL was used to achieve the Alumina deposition, as shown later in the recipe.

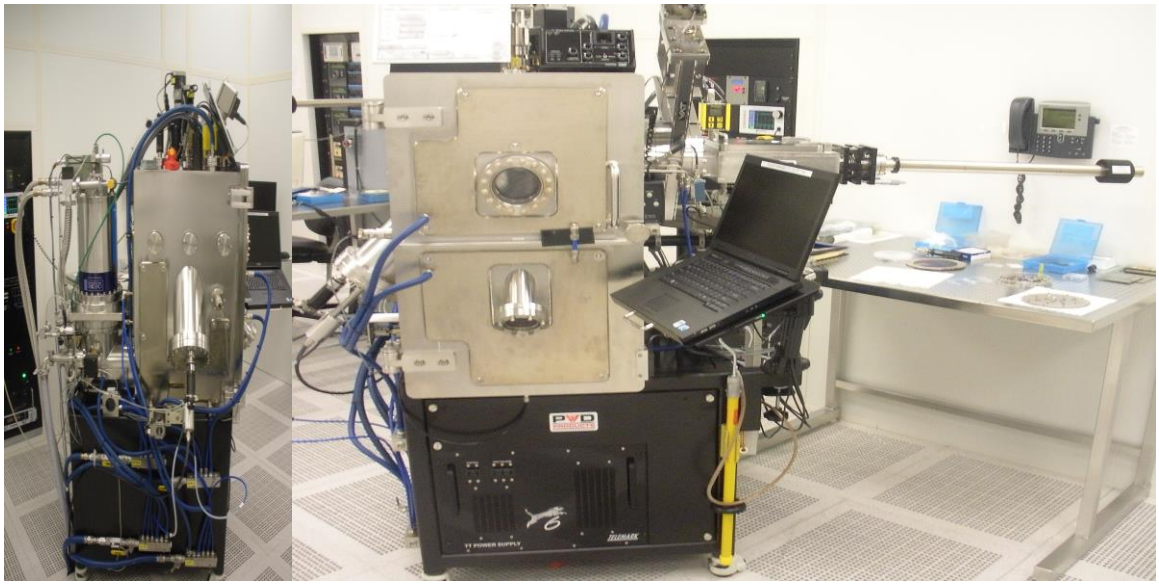

Figure 2-4: E-beam evaporator, PVD.

Electron beam lithography commonly written as e-beam lithography is a popular writing technique, where specialized pattern (~ 50 nm) can be written in a polymer film with a beam of electrons. It's a two-step process, the substrate is first coated with a thin layer of resist like poly (methyl methacrylate) commonly known as PMMA, which undergoes chemical changes upon exposure to the beam of electrons [49]. The designed writing is then developed, by dissolving the exposed areas in specific solvents. The RAITH150 Lithography (see Fig. 2-5) setup used for this work, is a multipurpose tool capable of direct e-beam exposure, wafer scale process development with high resolution. The system is extremely sensitive this ensuring an optimized process reproducibility. It can be used to expose structures of the magnitude of 5nm on very small few millimeters to larger few inches substrates.

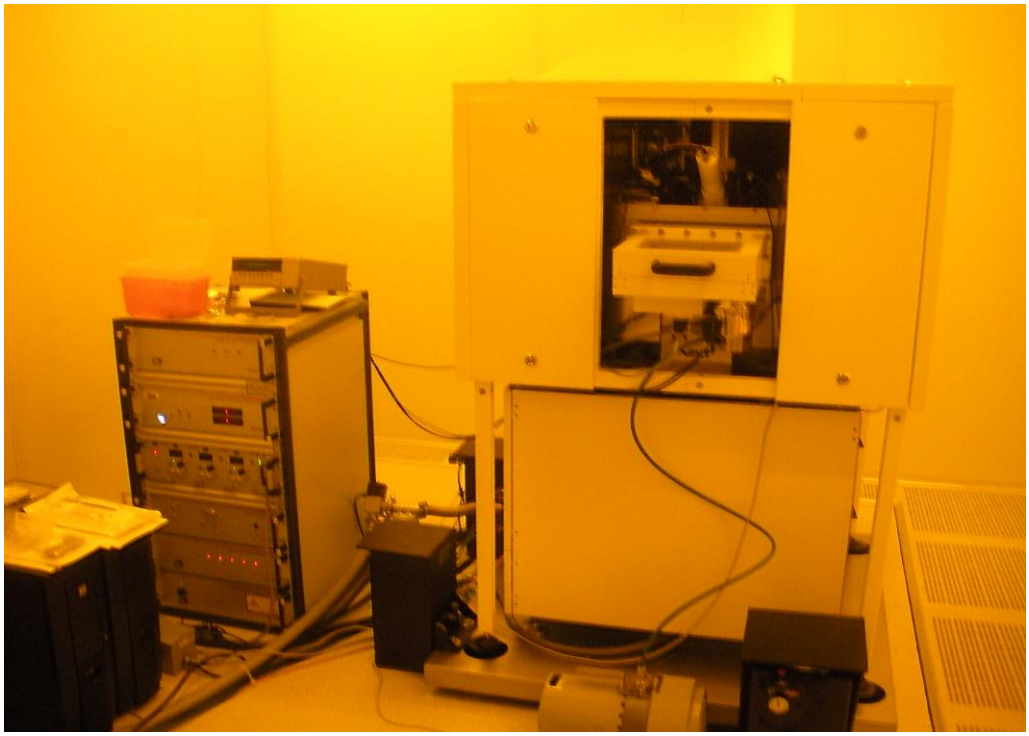

Figure 2-5: RAITH150 e-beam lithography setup at NRF.

Thermocouple is a precision cooling device, normally used in clean room fabrication of nanostructures. For our work, one tenth of a degree reliable stir-Kool Model SK-12D is employed, as shown in Fig. 2-6. The current model boasts both set point control function for long term use as well as a time dependent mechanism for ramp and soak setups. Furthermore, the unit can also be employed for isothermal stirring of solutions using magnetic bars.

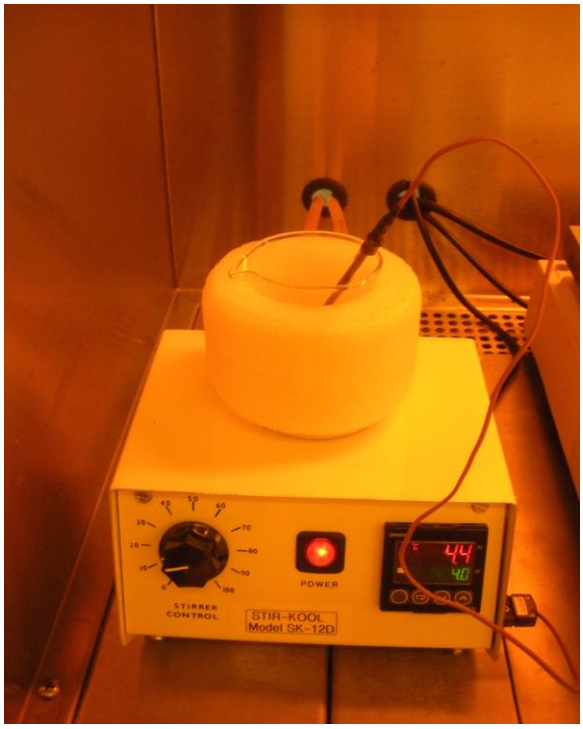

Figure 2-6: Thermocouple with MIBK and IPA at 1:3 ratio with a sample placed in a glass gar with a magnetic stirrer.

The Asher, uses O_2 plasma for shedding photoresist and descum, a technique commonly referred to as plasma ashing. The model used in this work is a ANATECH barrel SCE600 (Fig. 2-7), workable with a maximum power of 600 W. It is also functional for surface cleaning and surface treatment. The sophisticated device is equipped to work with up to 25 wafer, each four inch in thickness. More insight into the plasma ashing and advantages is discussed in the following section.

Figure 2-7: Asher, ANATECH barrel SCE600.

Plasma Enhanced Chemical vapor deposition (PECVD) method is commonly used to deposit dielectric layers [50]. PECVD uses plasma, a mixture of energetic species like reactive radicals, ions. The technique works with both etching and deposition requirements, depending on the interaction of the substrate with the plasma. In this work PECVD is used to deposit high quality silicon dioxide film. The Model used for this work is a STS 310PC SiO_2 - SIN - Amorphous Si at NRF in UF as shown in Fig. 2-8. The system has the capability to deposit silicon nitride, silicon dioxide and amorphous Si films. The temperature of the system is normally kept at 300 °C. and one can process up to four wafer of 4-inch thickness. The operational information can be found at the UF database [51].

Figure 2-8: STS 310PC - Plasma Enhanced Chemical Vapor Deposition System PECVD.

2.4 Nanostructure fabrication approaches

The work presented in this chapter uses the "Top-down" approach to fabrication, a favorable technique initiated with bulk materials / structures followed by elimination or complementing of nanoscale patterns. This technique is primarily utilized in fabricating semiconductor devices, photonics, memory integrated circuits [52].

2.4.1 Plasma ashing

In semiconductor manufacturing plasma ashing is common practice employed in semiconductor manufacturing pertaining to the removal of photoresist from an etched wafer. In

particular, oxygen (O_2) plasma, the oxygen combines with the photoresist to form ash, that is removable using a vacuum pump in a clean room. The particular "stripping" or high temperature ashing is used to remove bulky amounts of photo resist to clean the surface of photoresist as much as possible. Whereas, "descum" approach of plasma ashing is particularly used to remove photoresist in residual trenches, thus fine tuning the cleaning process.

2.4.2 Lift-off processing

Lift-off is a standard method employed in nano-fabrication of devices to create patterns on a substrate [53]. The patterns generated normally yield high fidelity and very reasonable geometries. During fabrication of semiconductor devices, the lift-off step is initiated after several stops of depositing photoresist, desired materials, lithography and so on. The lift-off mechanics dictates that the targeted/extra layers are removed using an appropriate solvent, usually acetone, resulting in the desired pattern with the desired material exposed directly on the substrate. Particularly, in our case of e-beam writing, the lift-off step is the process of dictating the pattern of e-beam written metal lines, ensuring film remains only where the photoresist has been cleared. [54].

2.5 Fabrication Recipes

The recipes discussed in this section lead to the realization of metasurfaces on Sapphire substrate and on a flexible Polyimide polymer, using the experimental tools discussed above. Moreover, for each substrate two devices were fabricated; a PT structure and a Passive/Hermitian metasurfaces. The recipes are adjusted accordingly to achieve the passivity as opposed to the PT symmetry. One must point out that the recipes are devolved using precise and certain chemicals

and equipment with particular strength, time etc. and variation from any of the parameters discussed here will lead to very different results.

2.5.1 Hermitian and PT metasurfaces on a sapphire substrate

The steps outlined in this section are applicable to both the passive/Hermitian and the Parity Time (PT) structures.

I. Pre-cleaning and preparation of Sapphire substrate

The sapphire substrate is cleaned by solvent clean (Acetone, Isopropanol (IPA)), followed by deionized water and blow dry (N_2).

The used Sapphire substrate has dimension 10 x 10 nm.

II. Spin coating the substrate

The substrate is spin coated using electron-sensitive resist film, poly (methyl methacrylate) commonly known as PMMA, we used the PMMA 950 A6 for spin coating.

1- First spin coat is executed at 500 rpm speed with 352 rpm acceleration, for 5 seconds.
2- It is followed by another coating at 4000 rpm speed at 352 rpm acceleration, for 45 seconds.
3- This yields a uniform thin film of PMMA of 600 – 630 nm thickness, measured using filmometrics.
4- Bake the substrate in the oven at 180 ^{0}C for 15 plus hours.

III. e-beam deposition and writing

1- Using e-beam deposition machine (discussed above), deposit 10 nm of Chromium (Cr).

2- e-beam writing parameters are slightly different for the PT and the passive/Hermitian structure, furthermore, for PT structure this step produces the first layer, whereas for the passive structure this is the final writing step. The writing parameters for the two structures are shown in Table 2-4.

Table 2-4: e-beam writing variables for the PT and Hermitian metasurfaces.

	Dosage / μCcm^{-2}	Size / nm	Separation / nm
PT structure	760	110	80
Hermitian structure	900	100	100

IV. Etching and development of the structures

1- Both the structures undergo etching using chrome etch solvent (CRH) of the 10 nm Cr.

2- Rinse the structures with Deionized (DI) water.

3- Dry with nitrogen (N_2) gas.

4- PMMA on the structures is developed using Methyl isobutyl ketone (MIBK) and Isopropanol (IPA) in 1 to 3 ratio, using a thermocouple at 4 ^{0}C.

5- Let the structures develop for 60 seconds.

6- Thoroughly rise with IPA.

7- Dry with N_2 gas.

V. Descum using O_2 Plasma

Desum procedure is initiated at 150 W power, 300 standard cubic centimeter per minute (SCCM) flowrate for 60 second. The image of the structure as seen by the Optical microscope is shown in Fig 2-9(left).

VI. e-beam deposition

At this step different materials are used for disposition, each deposited with a thickness of 290 nm at 1 Å/sec. For PT structure the material is Nickle (Ni), whereas Alumina (Al_2O_3) was deposited on the passive structure.

VII. Lift-off processing

1- The lift-off is done using acetone for both active and PT.

2- Wash the device with IPA to get rid of any residual material.

3- Dry with N_2 gas, final patterns are shown in Fig 2-9(middle) as observed under the microscope.

VIII. Ash using O_2 Plasma

Ash procedure is introduced at 300 W power, 3000 SCCM flowrate for 60 second.

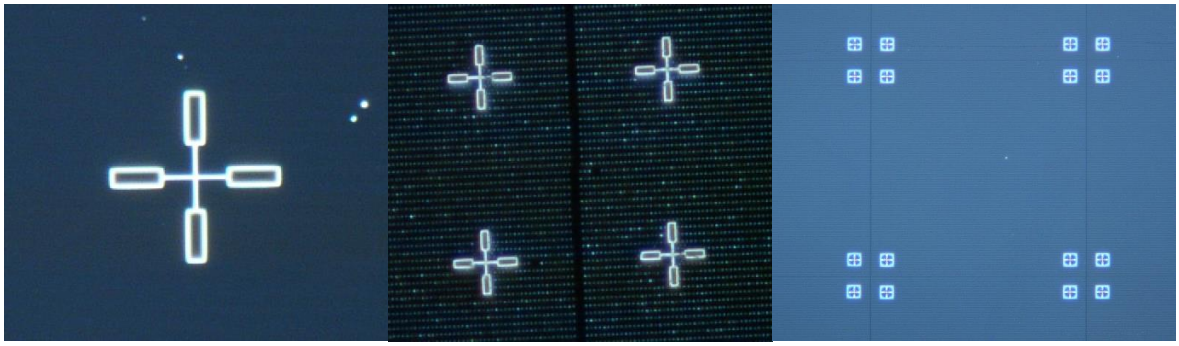

Figure 2-9: Fabrication steps of the PT metasurface on sapphire substrate. (left) Pre-Ni e-beam deposition, (middle) Ni-liftoff, (right) Pre-Al_2O_3 e-beam deposition.

Important Note: At this point the Hermitian structure is ready. From here onward the recipe steps only apply for the PT structure.

IX. *Spin coating and e-beam deposition*

Follow the steps outlined in *II* and *III* at a dosage of 840 μCcm^{-2}, of dimensions 110 nm and at a separation of 80 nm. The sample is now ready for alumina deposition as shown in Fig 2-9(right).

X. Follow steps from *IV-VIII* to create the second layer, but this time the depositing material is Al_2O_3.

Important Note: At this point the PT structure is ready. The final device was than checked under optical microscope Fig. 2-10. Summary of the fabrication steps employed to develop the PT metasurface on the sapphire substrate is shown in Fig. 2-11.

Figure 2-10: The sapphire substrate as seen using an optical microscope.

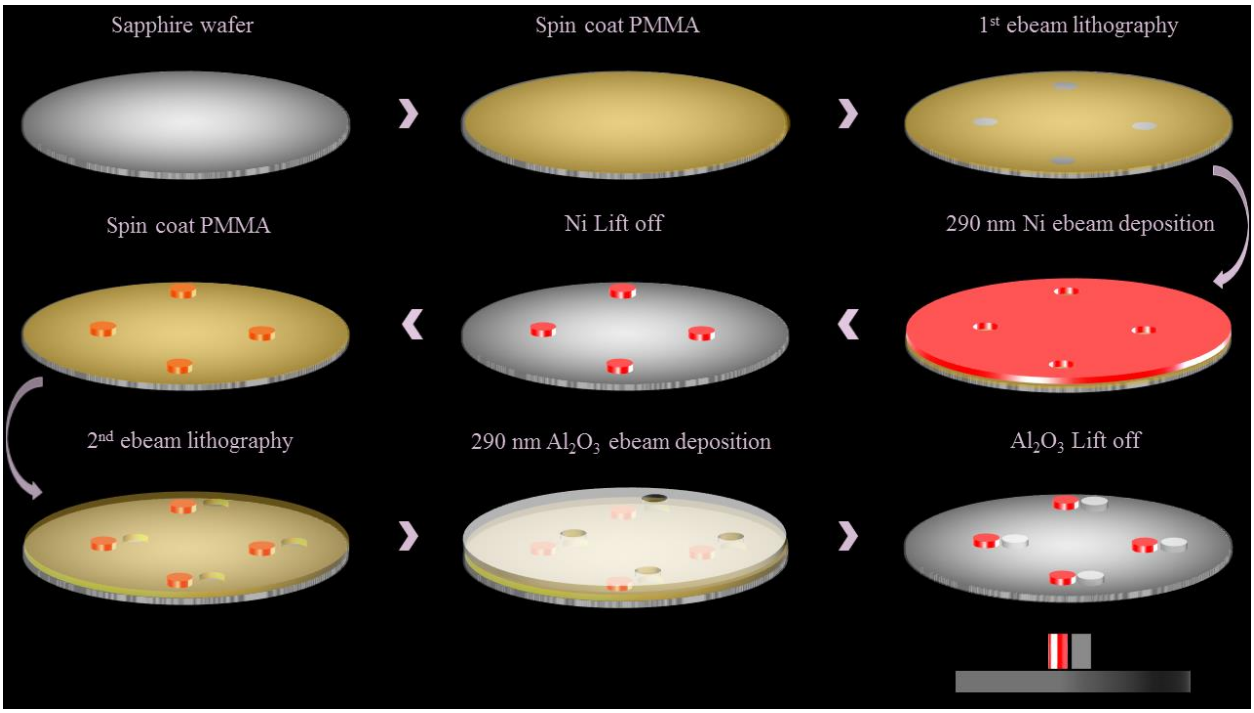

Figure 2-11: Detailed schematic of fabrication procedure of the sapphire based PT metasurface.

2.5.2 Polyimide polymer PT and Hermitian metasurface structures

The steps outlined in this section are applicable to both the Hermitian and the Parity Time (PT) structures.

I. *Pre-cleaning and preparation of Silicon substrate*

The silicon substrate is cleaned by solvent clean (Acetone, Isopropanol (IPA)), followed by deionized water and blow dry (N_2).

The dimensions of the substrate used to develop polyimide metasurface is 2 x 3 cm^2.

II. *PECVD the substrate*

The substrate is deposited with 300 nm of silica SiO_2.

III. *Spin coating the substrate*

PMMA 950 A6 is used for spin coating.

1- First spin coat is executed at 500 rpm speed with 352 rpm acceleration, for 5 seconds.
2- It is followed by another coating at 4000 rpm speed at 352 rpm acceleration, for 45 seconds.
3- This yields a uniform thin film of PMMA of 600 – 630 nm thickness, measured using filmometrics.
4- Bake the substrate in the Oven at 180 ^{0}C for 15 plus hours.

IV. e-beam writing

1st e-beam deposition, e-beam writing parameters for the two structures are the same described in Table 2-4. The device under the optical microscope is shown in Fig. 2-12(a).

V. 1st e-beam deposition

Ni is deposited for the PT structure, whereas Alumina (Al_2O_3) was deposited on the passive structure, both deposited with a thickness of 290 nm at 1 Å/sec.

VI. Ni Lift-off

1- The lift-off is done using Acetone.
2- Wash the device with IPA to get rid of any residual material.
3- Dry with N_2 gas, clear patterns were observed as seen in Fig. 2-12(b).

Important Note: At this point the Passive/hermitian structure is half done. From here onward the recipe steps only apply for the PT structure. From steps X and onward focus on removing the Si

wafer and getting the final flexible device and these steps are common between the Passive/hermitian and the PT device.

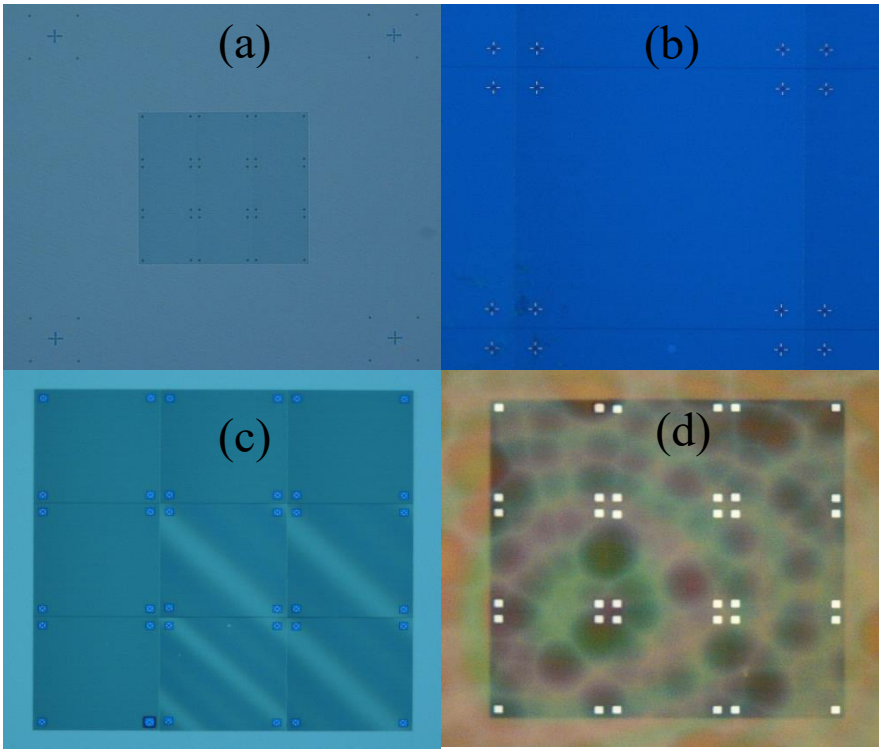

Figure 2-12: Fabrication steps observed under the optical microscope. (a) Pre-Ni deposition, (b) after Ni liftoff, (c) Pre-Al_2O_3 deposition, (d) final pattern on the polymer.

VII. Spin coating and e-beam lithography

1- Repeat step *III.*

2- Execute 2nd e-beam writing, at a Dosage of 760 µCcm^{-2}, using separation of 80 nm and a size of 110 nm, as seen under optical microscope Fig. 2-12(c).

VIII. 2nd e-beam deposition

Al_2O_3 was deposited at a thickness of 290 nm at 1 Å/sec.

IX. Al_2O_3 *Lift-off*

1- Depositing alumina increases the temperature of the chamber, thus causing the PMMA to be hardened. As a result, the PMMA is exposed to UV for 6 min to soften it. Afterwards, the lift off is done using Acetone.
2- Wash the device with IPA to get rid of any residual material.
3- Dry with N_2 gas.

X. Spin coating Polyimide

1- Polyimide is spin coated on both the passive and the PT structures, at 1000 rpm speed at 100 rpm acceleration, for 60 seconds.
2- This result in a uniform Polyimide film of 10 μm thickness.

XI. Dry and wet etching

1- Both structures undergo dry etching to remove the Si substrate.
2- This is followed by removal of SiO_2 by wet etching (buffer oxide) the devices. The final pattern on the Polymer is shown in Fig. 2-12(d).

Important Note: At this point the PT structure and the passive flexible polymer devices are ready. The summarized schematic of the fabrication steps of the Polyimide PT metasurface device is shown in Fig. 2-13.

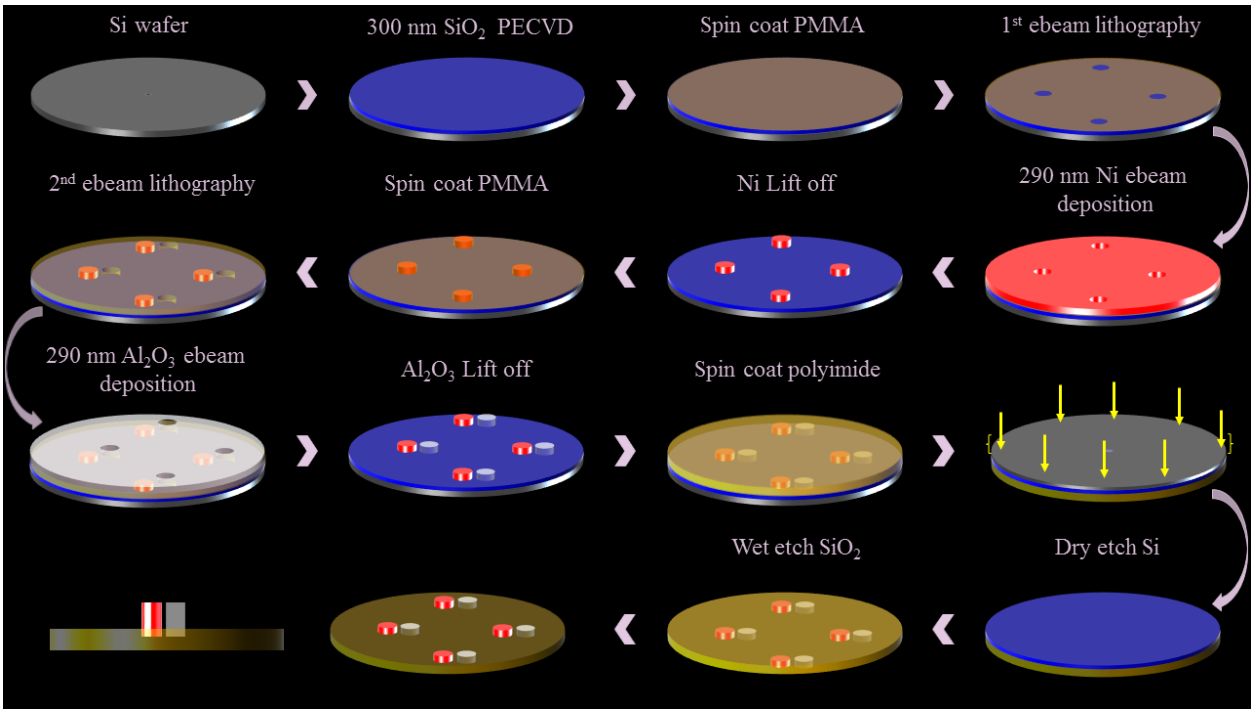

Figure 2-13: Summary of the fabrication steps employed to develop the Polyimide metasurface.

Figure 2-14 is an image of the ready flexible device, where images (a) and (b) highlight the device from the top and side, with the arrow in (b) pointing to the designed pattern. Whereas, (c) is the final device with the Si etched off. In order to confirm the pattern, the patterns on the device were observed with a Scanning Electron Microscope (SEM) and the resulting images are shown in Fig. 2-15. The SEM images show that cylinders average diameter is 158 nm, with a average separation of 54 nm. The average lattice constant average is 696 nm along the x-axis and 615 nm along the y –axis.

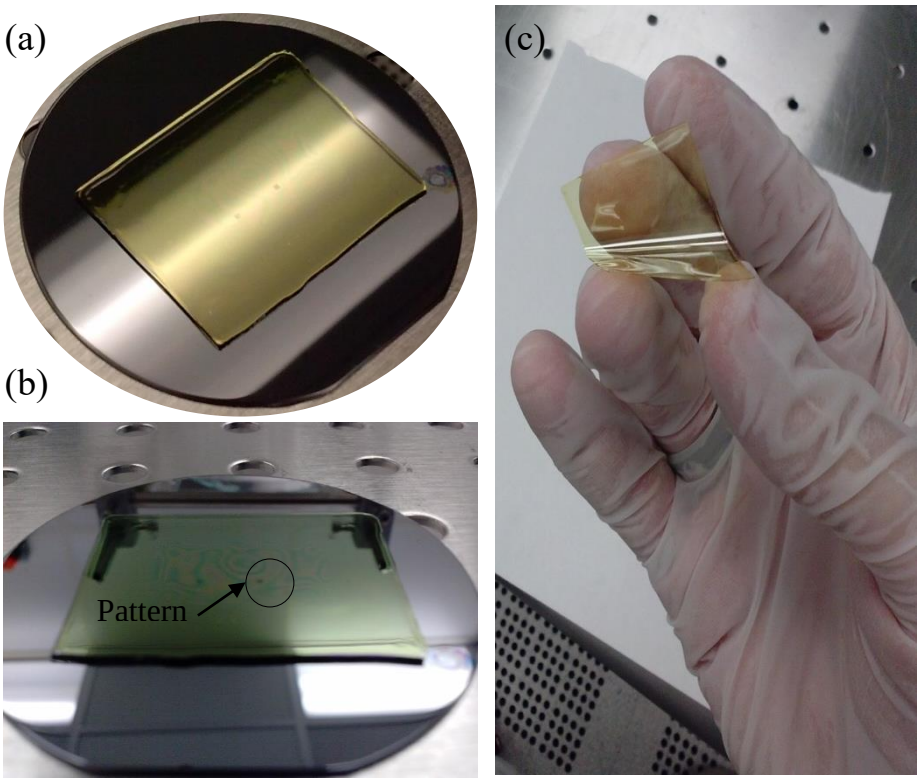

Figure 2-14: (a) Top view, (b) side profile of the flexible PT symmetric metasurface on a silicon substrate, (c) The final device in hand.

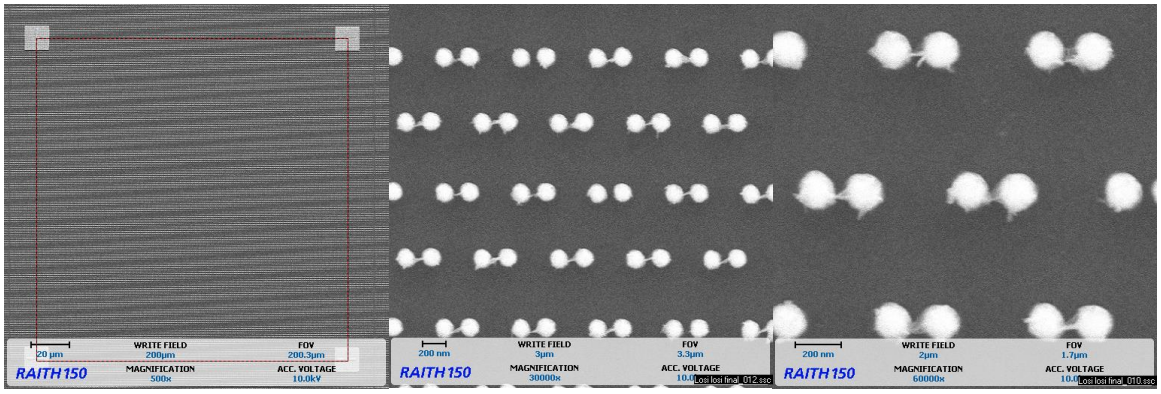

Figure 2-15: SEM images of the pattern on the flexible PT metasurface.

2.6 Experimental diffraction orders of fabricated PT metasurfaces

All the aforementioned samples, sapphire based (PT and passive) and polymer based (PT and passive) were optically illuminated by a 532 nm continuous wave laser beam, and incoherent white light beam. Both beams pass through a vertical polarizer, then focused by a biconvex lens, and are at normal incidence to the substrates. The power of the diffracted orders power was measured by a powermeter.

Both configurations are shown in Fig. 2-16, where the white and red structure represents the pattern and it is quite clear that the diffraction is occurring at an angle. Starting off with 532 nm results, the transmission efficiency was calculated the expression (output power/input power)*100 at each diffraction pattern. One should point out that the diffraction pattern appeared 5 cm from the device as shown in Fig 2-17. The six diffraction orders are [1, 1] (**1**), [1, 0] (**2**), [0, 1] (**3**), [-1, -1] (**4**), [-1, 0] (**5**), and [0, -1] (**6**).

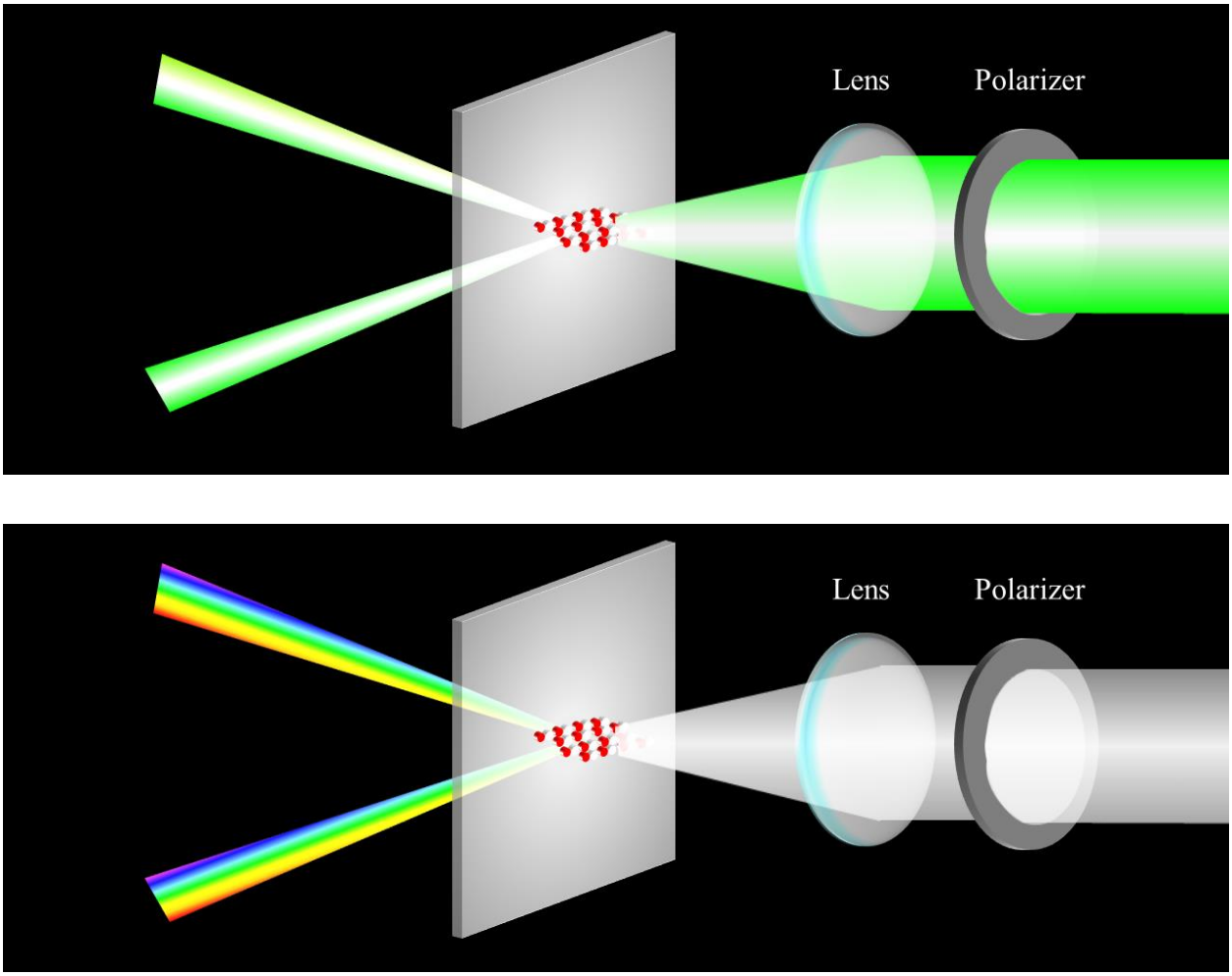

Figure 2-16: (Top) A schematic of the characterization set-up, with a 532 nm continuous wave laser beam, (Bottom) A schematic of the characterization set-up, with a broadband incoherent white light beam.

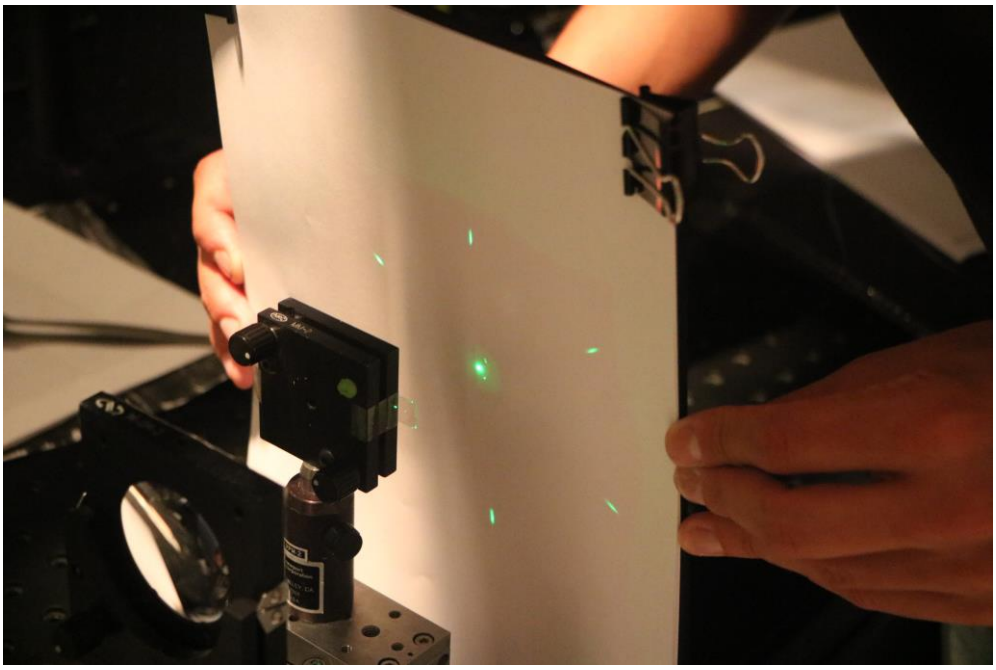

Figure 2-17: Experimental setting to observe the diffraction orders.

The respective transmission efficiency in percentage output powers for each diffraction pattern corresponding to the surfaces (PT and passive) and the location of the diffraction pattern from the device is shown in diagrams Fig. 2-18 for the sapphire substrate and Fig. 2-19 for the flexible device. The drawn images show clearly that once green light passes through the designed PT metasurface certain diffraction orders are diminished, as opposed to the equal power diffraction patterns observed in the case of passive structure. The images of the diffraction pattern as observed by naked eye and captured by camera are also shown for sapphire, Fig. 2-18(b) Hermitian and (d) is the PT metasurface.

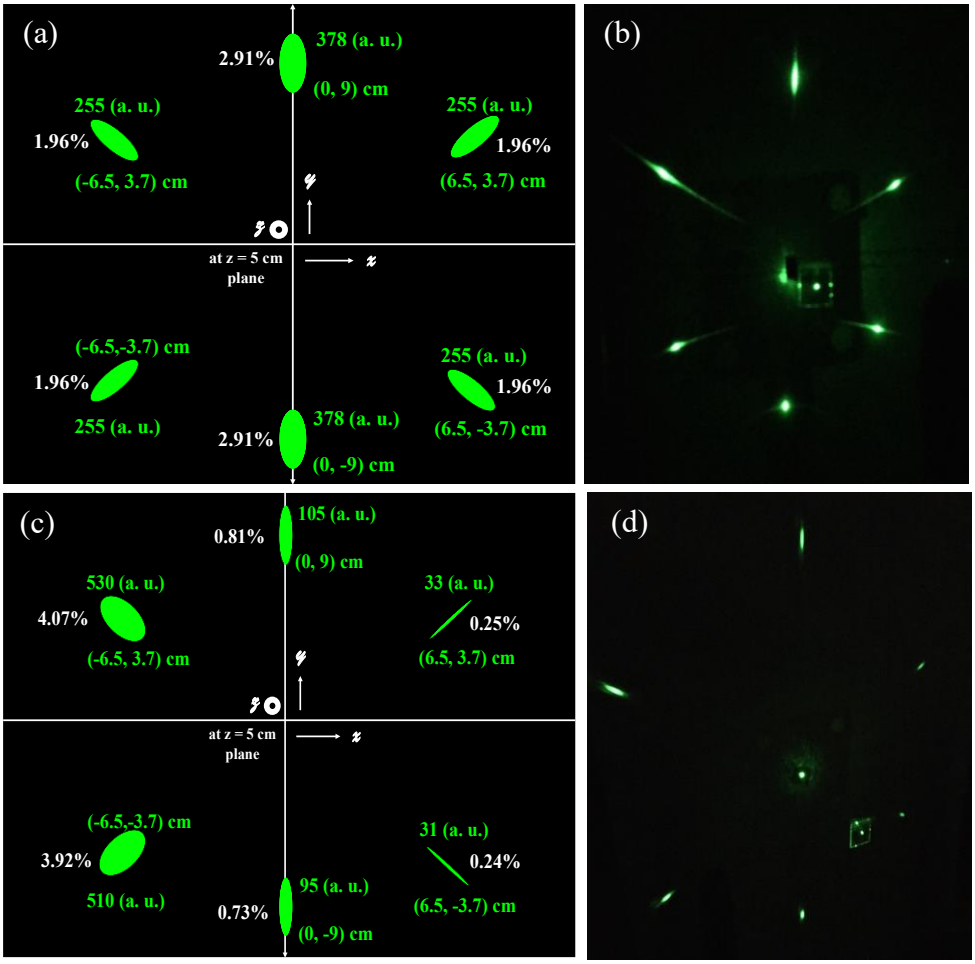

Figure 2-18: At 532 nm transmission efficiency and output power along with location of diffraction orders as observed experimentally for the sapphire substrate, (a) Hermitian, (b) PT metasurface. (c-d) correspond to images captured by a digital camera.

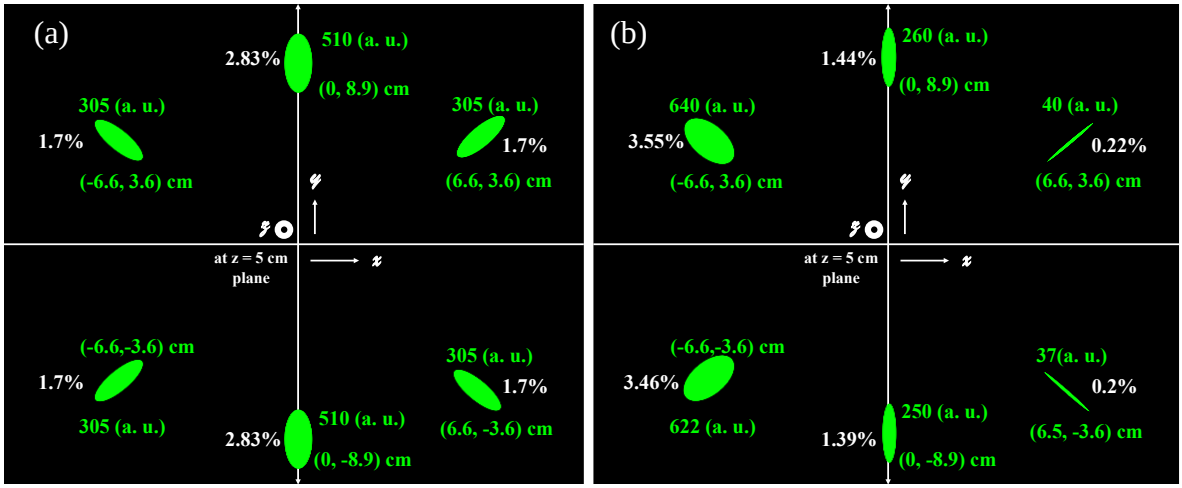

Figure 2-19: Transmission efficiency and output power along with location of diffraction orders as observed experimentally for the flexible substrate, (a) Hermitian, (b) PT metasurface at 532 nm.

In order to discuss the accuracy of the experimental results observed at 532 nm, the transmission efficiency of the six orders are shown in Table 2-5. It is a comprehensive summary of the experimental as well as the numerical data observed at 530 nm shown in section 2.2.1. The table is focusing on the PT metasurface for both the sapphire and polyimide.

Table 2-5: Comparative study of the transmission efficiency at 532-530 nm for the six diffraction order as observed experimentally and numerically for the sapphire and polymer PT metasurface.

Diffraction orders	Sapphire / %		Polyimide / %	
	Numerical	Experimental	Numerical	Experimental
1	3.2	4.07	3.61	3.55
2	3.2	3.92	3.61	3.46
3	0.55	0.81	0.66	1.44
4	0.15	0.24	0.18	0.2
5	0.15	0.25	0.18	0.22
6	0.55	0.73	0.66	1.39

As shown in Table 2-5, both sapphire and polyimide samples yield matching results as predicted by the numerical simulations. Some discrepancy is observed and this is due to the fact to the imperfection in fabrication. The vertical spacing between the different unit cells in both samples is not exactly 597 nm, it is close to 615 nm (this is attributed mainly to the e-beam lithography machine used). The vertical orders (3 and 6) are also affect as direct consequent of the aforementioned comment.

2.6.1 Transmission efficiency for Broad band diffraction orders

This section is focused on the response of the six diffraction orders as a result of incident white light, a broad band feature. The experimental plan followed coincides with above results, and the transmission efficiencies are observed for both the substrates and the respective PT and passive/Hermitian metasurfaces.

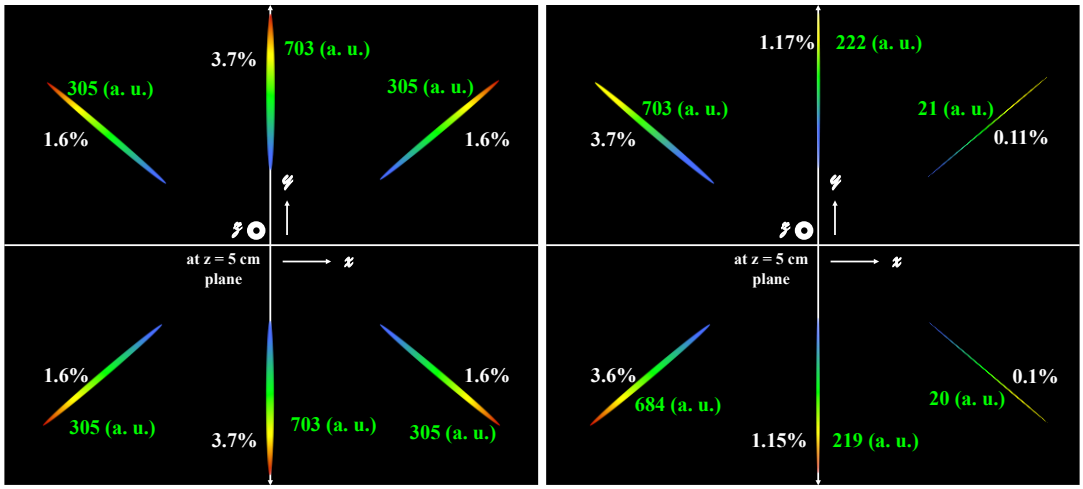

Figure 2-20: Broad band transmission efficiency and output power along with location of diffraction orders as observed experimentally for the flexible substrate, (left) Hermitian, (right) PT metasurface.

Fig. 2-20 shows a schematic diagram of diffraction orders for a Hermitian structure (a) and a clear decrease in efficiency for certain orders as expected by numerical analysis for the PT metasurface (b) for the case of polyimide. The same set of measurements were carried out for the sapphire substrate and the corresponding transmission efficiencies are shown in Table 2-6. Figure 2-21 showcase the image captured by the digital camera, clearly highlighting the PT symmetry effect as oppose to the diffraction patterns observed for the Hermitian surface, Fig. 2-12(a).

Table 2-6: Broad band transmission efficiency experimentally observed for the sapphire substrate.

Diffraction orders	Hermitian / %	PT metasurface / %
1	2.05	4
2	2.05	3.85
3	3.98	1.33
4	2.05	0.14
5	2.05	0.12
6	3.98	1.3

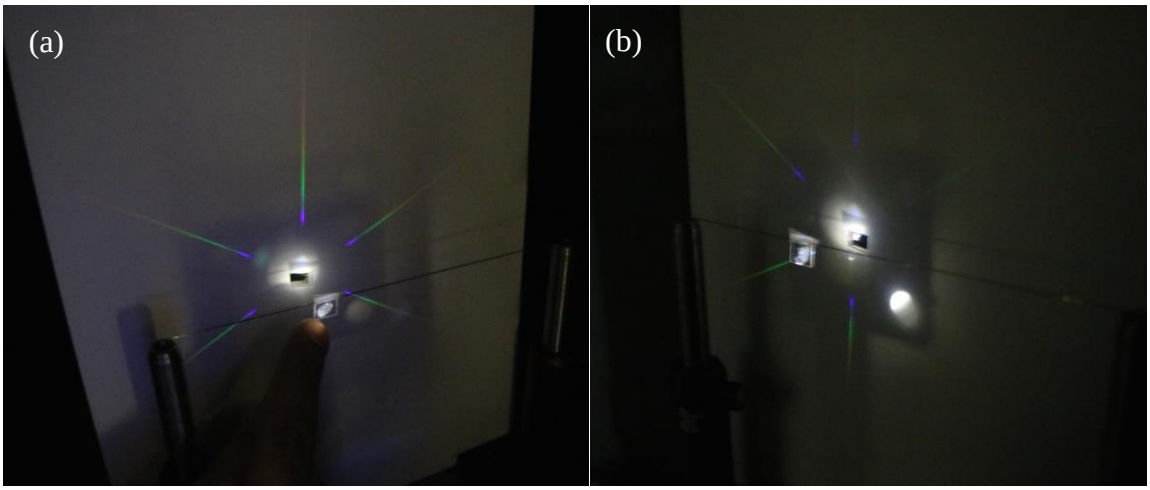

Figure 2-21: Digital image captured for the broad band diffraction orders of sapphire substrate, (a) Hermitian, (b) PT metasurface.

2.7 Summary

In this chapter, we have shown experimentally that PT symmetry is established through the diatomic Bravais Lattices. Such lattices are not only suitable for single wavelength i.e. 532 nm, but it is extended over a broadband (400 – 600 nm) of wavelengths. The first ever example of a flexible PT meatsurface is presented and the transmission efficiency of the six observed diffraction orders is observed. The experimental results have an excellent agreement with numerical simulations. In addition, we have shown that different substrates, with few modifications to the structural dimensions, can still lead to the same results. Both substrates (sapphire and polyimide) are not lossy for the visible band.

CHAPTER 3: DECOHERENCE AND QUANTUM INTERFERENCE ASSISTED ELECTRON TRAPPING IN A QUANTUM DOT

3.1. Introduction

The interaction between any quantum system and its environment is inevitable, thus, decoherence and dissipation contribute significantly to the coherence-destructive process [55]. Decoherence is one of the main obstacles in many research fields such as: quantum information processing [56]; quantum optics, when measuring optical Schrodinger cat States [57]; condensed matter physics, when looking for mesoscopic interference phenomena in quantum transport of electrons [58-59], etc. Since many interesting quantum phenomena are based on coherence, many solutions are proposed, and are currently in use, to suppress or overcome decoherence [60], such as quantum error-correction codes [61], error-avoiding codes [61, 62], echo techniques [63], quantum feedback operations [57], optimal control technique [64], and many more. Furthermore, some groups are looking for the spectral composition of the noise generated by the decoherence. Other research groups are trying to fight decoherence, through the knowledge of their spectral density, thinking this would be more operative [65]. A rather opposite approach to this stream of research is found in the quantum biology, where scientists are trying to take advantage of the decoherence in the quantum dynamics of excitons in order to find explanations for the high efficiency in solar energy harvesting in photosynthetic systems [66]. Recently, there are many works proposing mechanisms for environment-assisted energy transfer in quantum networks, such as noise-assisted transport [67] and oscillation-enhanced transport [68-70]. The efficiency of the energy transfer through the biological quantum systems and the evidence of quantum coherence have provoked questions about the role of the environment in the quantum transfer process and its

contribution to the transport efficiency. One of the non-biological applications that could not operate at high temperatures (100 K – 300 K), mainly because of decoherence, is the electrically driven Single Photon Source (SPS). The role of decoherence in localizing electrons has been reported in many previous works [71, 72]. Another approach is applying continuous measurement to keep the quantum state in a pure state. This approach is known as quantum Zeno effect [73]. On the other hand, some groups reported that continuous measurement will lead to quantum anti-Zeno effect [74]. The role of decoherence in damping quantum interference has been discussed in many reports [75, 76] led by the work presented by Stern, Aharanov, and Imry (SAI) [77].

In this chapter, a novel physical method is discussed that takes advantage of decoherence and results in an enhanced electron trapping probability in the central QD at room temperature. The configuration spots the light on the interplay between quantum interference of the electron with itself and decoherence in trapping the electron in the central quantum dot (QD). This physical phenomenon can be a prototype to be used for an electrically driven SPS operating at room temperature as shown in Chapter 4.

3.2. Structural realization of the trapping mechanism

We consider the transport of a single electron in a nanoring (NR) with 15.1 nm as minor radius and 30 nm as major radius as shown in Fig. 3-1. The NR is divided into two regions. The first region, which is *n*-doped $In_{0.45}Ga_{0.55}As$ with concentration of 6.0×10^{14} cm^{-3}, constitutes 85% of the NR, and it will be referred to as the 'zero-region' for the rest of the dissertation. As for the second region, referred to as the 'intrinsic-region' for the rest of the dissertation, it is made of five QDs, four of them are InAs and the central QD is $In_{0.5}Ga_{0.5}As$, with different heights. QD # 5 (see Fig. 3-2 for QDs labeling), is *n*-doped with a concentration of 1.0×10^{18} cm^{-3}. The zero-region and

QD # 5 are not degenerate semiconductors. Barrier # 1 and # 6 are made of GaAs, while barriers # 2 and # 5 are made of $In_{0.1}Ga_{0.9}As$. As for barrier # 3 and # 4, they are made of $Al_{0.4}Ga_{0.6}As$. A monolayer of ploy (methyl methacrylate) (PMMA), which has radius of 8.05 nm, is coating the region starting from the interface between QD # 2 and barrier # 3 to the interface of barrier # 4 and QD # 4. The outer layer, up to the surface of the NR, is made of $In_{0.2}Ga_{0.8}As$. As a result of this concentric configuration, the central QD acts like an *electron pocket* that traps the electron with the help of decoherence as shown later. All interfaces between the materials considered in the aforementioned configuration are recognized as straddling gap (type I). Based on all chosen materials and types of interfaces, the conduction band (CB) profile is shown in Fig. 3-2, based on Schrödinger-Poisson solution. All semiconductor materials have the same crystal structure and direct band gap. In addition, the NR is coupled to a single-electron source (SES) (it is not the scope of this work to provide SES operating at room temperature) [78, 79]. The SES is triggered to emit an electron and thus this electron can transport through the whole configuration. Such SES emit a single electron every 0.1-10 ns depending on the configuration of the SES. Therefore, the time evolution is well described by the single-electron master equation as shown and justified below.

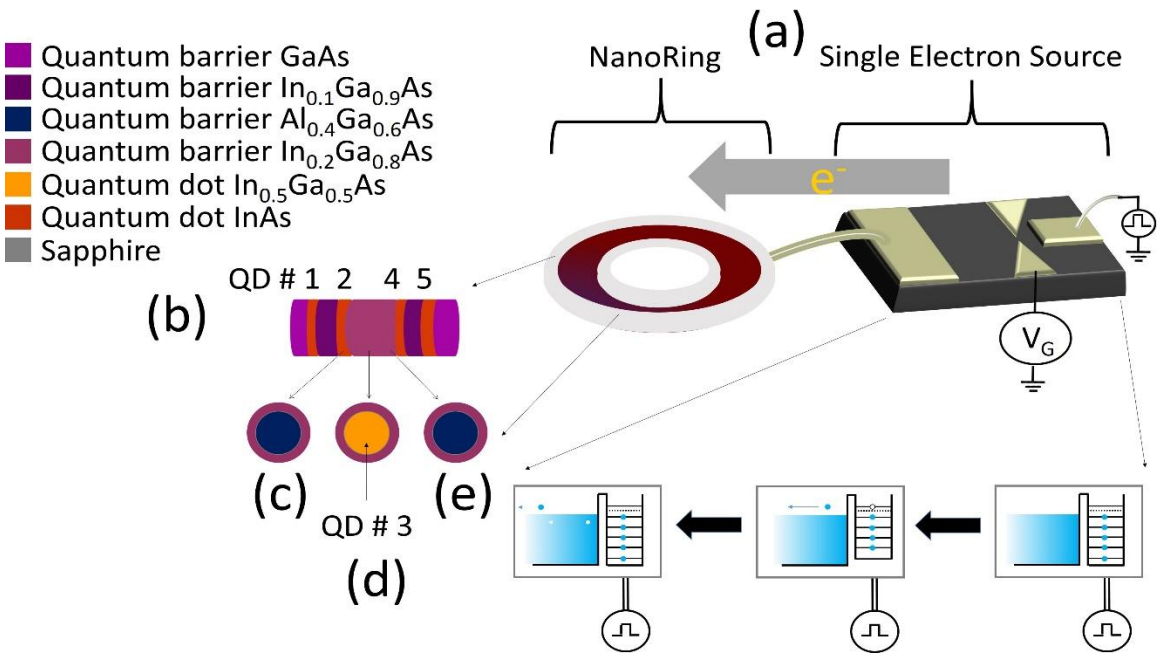

Figure 3-1: (a) Schematic setup (not to scale). (b) A magnified diagram for the intrinsic region made of five quantum dots of (from left to right) 1.24, 1.5, 5.0, 1.5, 3.14 nm height, respectively. (c) A cross section view for the interface between quantum dot #2 and barrier #3. (d) A cross section view for quantum dot #3 (electron pocket). (e) A cross section view for the interface between quantum dot #2 and barrier #4.

3.3. Quantum transport in the Nanoring

Given that aforesaid configuration has zero electric field across the five-QD region and the electron's eigenenergies are close to the conduction band-edge minima, the 3D time-independent Schrödinger equation in cylindrical coordinates and in the effective mass approximation is used to find the eigenenergies and eigenstates for each QD separately. These states are used later (see below) to describe the dynamics of the electron by means of a generalized master equation in the tight-binding approximation, taking into account electron-LO phonon interaction (ELOPI).

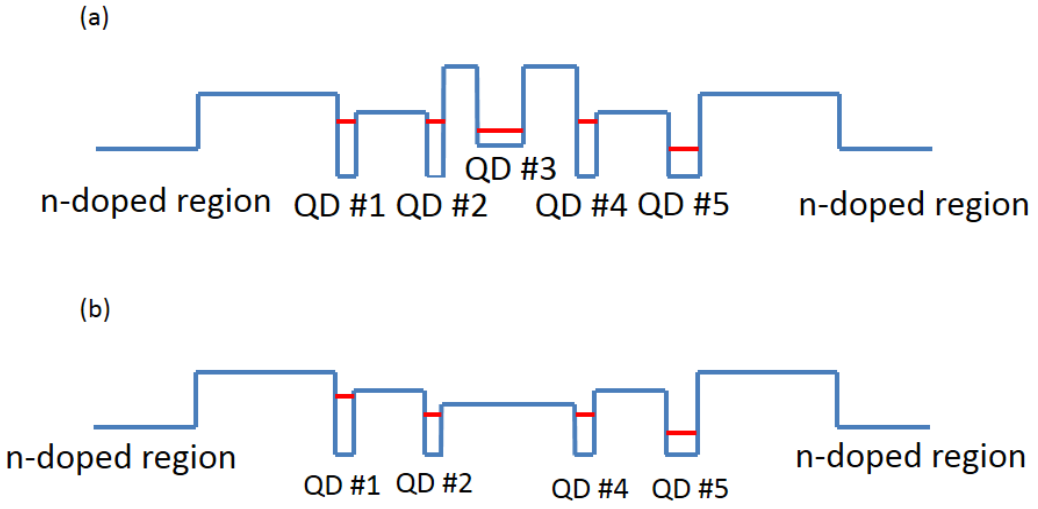

Figure 3-2: (a) The conduction band, for radius r < 8.05 nm. (b) The conduction band, for r > 8.05 nm. The quantum dots' ground eigenstates are shown.

For simplicity, an infinite confining potential in the radial direction is assumed. The eigen energies and wavefunctions of QDs # 1 and # 5 are obtained systematically. As for QD # 3, due to the relatively large band gap (5 eV) for the PMMA monolayer, it is assumed to be confined in infinite potential but with different radius than QD # 1 and # 5. Both QDs # 2 and # 4 (see Appendix A) require an additional boundary condition due to the *electron pocket*, i.e. the electron's energy has to be conserved irrespective of the interface with $Al_{0.4}Ga_{0.6}As$ or $In_{0.2}Ga_{0.8}As$ (see Fig. 3-1). The zero energy is set at the minimum of the conduction band of InAs QDs.

We start with the following Hamiltonian,

$$H = H_I + H_c \tag{3-1}$$

where H_I is the Hamiltonian of an electron in the 'intrinsic region' described as

$$H_I = \sum_i \varepsilon_i a_i^\dagger a_i + \left(-\sum_{i\neq j} t_{ij} a_i^\dagger a_j + h.c\right) + \hbar\omega_{LO} b^\dagger b + \lambda \sum_i a_i^\dagger a_i (b^\dagger + b) \tag{3-2}$$

and H_c is the Hamiltonian that describes the coupling between both QD # 1 and # 5 and 'zero-region'

$$H_c = \left(\sum_0 V_{01} C_0^\dagger a_1 + h.c\right) + \left(\sum_0 V_{05} C_0^\dagger a_5 + h.c\right) \tag{3-3}$$

In Eqn. (3-2), the first term describes the on-site ground state for the five QDs. The second term, which is based on the tight-binding model, describes the hopping of the electron between the QDs, where t_{ij} is a 3-D hopping integral given by the off-diagonal matrix elements of H_t [80], i.e. (see Section 3.4 for details)

$$t_{ij} = \int \Psi_i^* H_t \Psi_j d^3 r \tag{3-4}$$

where H_t is the kinetic and potential energy of the electron inside the QD,

$$H_t = -\frac{\hbar^2}{2m^*}\nabla_{3D}^2 + V(r,z) \tag{3-5}$$

The third term in Eqn. (3-2) describes non-dispersive LO phonons of $In_{0.45}Ga_{0.55}As$, since it constitutes 85% of the NR. In polar semiconductors, as the size of the QD decreases, electrons strongly interact with the phonons that have long wavelength $|\boldsymbol{q}| \leq 2\pi/(QD\ size)$. This suggests that a model with dispersionless LO phonons will be accurate [81]. It has been shown in experimental work that for InAs QDs embedded in GaAs matrix, the GaAs LO are more prominent than the InAs LO phonons [82]. The fourth term in Eqn. (3-2) describes the interaction between the electron and LO phonons with coupling strength λ (see Appendix B). In this work, $g = \lambda/(\hbar\omega_{LO})$ is almost 0.066. As for the acoustic phonons, in polar semiconductor nanostructures, the electron-acoustic phonon coupling is weak because the energy difference between the ground state and excited state ΔE is greater than 64 meV in all QDs except the central QD where the

energy difference is greater than 110 meV. As a result, the acoustic phonons are taken into account in the master equation, as shown later, as part of the total decoherence. Since we are dealing with ELOPI, a canonical unitary transformation is required to eliminate the linear coupling terms in Eqn. (3-2). The transformed Hamiltonian is $H_I' = e^S H_I e^{-S}$, where $S = -g\left(\sum_i a_i^\dagger a_i (b^\dagger + b)\right)$. We obtain

$$H_I' = \sum_i a_i^\dagger a_i \left(\varepsilon_i - \lambda^2/\hbar\omega_{LO}\right) + \left(-\sum_{ij} t_{ij} a_i^\dagger a_j e^{-2g(b^\dagger - b)}\right) + \left(-\sum_{ij} t_{ji} a_j^\dagger a_i e^{-2g(b^\dagger - b)}\right) + \hbar\omega_{LO} b^\dagger b + \left(2\lambda^2/\hbar\omega_{LO}\right) \tag{3-6}$$

In Eqn. (3-6) the first term shows the renormalization of the QDs' eigenstates in the presence of strong ELOPI. The eigenstates of the transformed Hamiltonian H_I' are in the tensor product form and are denoted by $|n_e, N\rangle$, where $n_e$represents the state of the electron, i.e. ground or excited, and *N* represents the number of LO phonons. The Hamiltonian in Eqn. (3-6) is solved in the following basis $|SES\rangle$, $|zero - region\rangle$,$|1_g, 0\rangle$, $|2_g, 0\rangle$, $|3_g, 0\rangle$, $|4_g, 0\rangle$, and $|5_g, 0\rangle$, where $|SES\rangle$ is the electron in the SES before being injected in the NR, $|zero - region\rangle$ is the electron in the 'zero-region' in the NR after being injected from the SES and $|1_g, 0\rangle$ is the electron in the ground state of QD # 1 with no phonons. We define the phonon displacement operator $\mathcal{D}(\beta) = e^{\beta b^\dagger - \beta^* b}$. We can now make use of the well-known formula for the matrix elements of the displacement operator [83, 84].

$$\langle N'|\mathcal{D}(\beta)|N\rangle = \left(\frac{N!}{N'!}\right)^{1/2} |\beta|^{N'-N} e^{-|\beta|^2/2} \times L_N^{N'-N}(|\beta|^2) e^{i(N'-N)\phi} \tag{3-7}$$

where $\beta = |\beta|e^{i\phi}$ and $L_N^{N'-N}(|\beta|^2)$ are the associated Laguerre polynomials. For $\beta \ll 1$ the associated Laguerre polynomials are approximately

$$L_N^{N'-N}(|\beta|^2) \approx \frac{N'!}{N!\ (N'-N)!}\left(1 + \frac{N}{N'-N+1}|\beta|^2\right) \tag{3-8}$$

Thus, for $\beta \ll 1$ only the phonon states with $N' = N$ couple to each other in a good approximation, and $\langle N|\mathcal{D}(2g)|N\rangle = e^{-2g^2}$. Therefore, the second and third terms in Eqn. (3-6) show that the hopping term t_{ij} is reduced by a factor of $e^{-2\lambda^2/(\hbar\omega_{LO})^2}$. In the weak ELOPI considered in this work, $e^{-2\lambda^2/(\hbar\omega_{LO})^2} \approx 1$ and thus the hopping terms are not reduced (see Appendix B).

The validation of the aforementioned Hamiltonian depends on the following criteria; in this configuration there must be no electrons in the CB. This is calculated in the standard way as follows:

$$n = \int_{E_c}^{\infty} D(E) f^{FD}(E) dE \tag{3-9}$$

Since the configuration has a large length-to-width ration, $D(E)$ is approximated by the density of states of a 1D NR (shown later in text). Doping (type and concentration) along with temperature are taken into account through the Fermi-Dirac function $f^{FD}(E)$. We observe that on average there are virtually no electrons in the whole configuration. Consequently, when the SES is triggered and a single electron is emitted, H_I' is a valid description for this single electron. Nevertheless, H_c describes the coupling between the 'zero-region' (quasi-continuum) and QDs # 1 and # 5. The

electron inside the 'zero-region' is incoherent because of the long time effects of the acoustic phonons. Such effects do not conserve the energy of the electron. This coupling is well described by the Fermi's golden rule for transition rates as follows:

$$W_{0\to 1_g} = \frac{2\pi}{\hbar}\int_{E_c}^{\infty} dE_0 \left|\langle 1_g|H_c|0\rangle\right|^2 D(E_0)\, f^{FD}(E_0)\, \left(1 - f^{FD}\left(E_{1g}\right)\right)\delta\left(E_{1g} - E_0\right) \qquad (3\text{-}10)$$

$$W_{1_g\to 0} = \frac{2\pi}{\hbar}\int_{E_c}^{\infty} dE_0 \left|\langle 0|H_c|1_g\rangle\right|^2 D(E_0)\, f^{FD}\left(E_{1g}\right)\left(1 - f^{FD}(E_0)\right)\delta\left(E_{1g} - E_0\right) \qquad (3\text{-}11)$$

$$W_{5_g\to 0} = \frac{2\pi}{\hbar}\int_{E_c}^{\infty} dE_n \left|\langle 0|H_c|5_g\rangle\right|^2 D(E_0)\, f^{FD}\left(E_{5g}\right)\left(1 - f^{FD}(E_0)\right)\delta\left(E_0 - E_{5g}\right) \qquad (3\text{-}12)$$

and

$$W_{0\to 5} = \frac{2\pi}{\hbar}\int_{E_c}^{\infty} dE_0 \left|\langle 5_g|H_c|0\rangle\right|^2 D\left(E_{5_g}\right) f^{FD}(E_0)\, \left(1 - f^{FD}\left(E_{5g}\right)\right)\delta\left(E_0 - E_{5g}\right) \qquad (3\text{-}13)$$

The coupling terms in Eqn. (3-3), V_n and V_p, are much smaller than t_{12} and t_{45}. This confirms that we have a weak coupling between the outer QDs and the leads. Thus a standard formalism appropriate for the description of such a system is the generalized master equation in Born and Markov approximation [85],

$$\partial_t \rho_{m,n} = \frac{i}{\hbar}[\rho, H_I']_{m,n} + \delta_{m,n}\sum_{l\neq m}\rho_n W_{m,l} - \gamma_{m,n}\rho_{m,n} \qquad (3\text{-}14)$$

where $\gamma_{m,n} = \frac{1}{2}\sum_l (W_{l,n} + W_{l,m}) + \frac{1}{T_2}$ is the total decoherence which includes the dephasing time T_2 due to interaction of the electron with its environment, such as electron-phonon (both acoustic and optical, and both elastic and inelastic) interaction, hyperfine interaction, and charge noise. The rates $W_{m,l}$ of transition between the leads and the outer QDs. Eqn. (3-14) is valid when the correlation time in the heat bath is much smaller than the relaxation time of the electron system. A rough estimate for the correlation time is $\frac{\hbar}{k_b T} \sim (1 - 3.5) \times 10^{-14}$s for $T = 100 - 300$ K, respectively, which is smaller than the electron relaxation time, in such systems, $\sim 10^{-12}$s. The dephasing time T_2, based on temperature, is determined through the homogeneous broadening $2\hbar/T_2$ [86, 87]. At room temperature, the experimental dephasing times are of the order of 200-300 fs [86-88]. We choose $T_2 = 285$ fs at 300 K because there is no carrier-carrier interaction. At $T = 100$ K, the dephasing time is 2 ps [86-88]. It is worth to mention that we ignore the change in band gap due to the lattice constant mismatch between the different materials. However, this does not affect the final results. In addition, we disregard any electron-hole interaction until the electron is trapped. For calculating the ground state of QD # 5 the doping is taken into account through the Schrödinger-Poisson equation. As a result, the ground state of QD # 5 will be $E'_{5g} = E_{5g} - \frac{\lambda^2}{\hbar\omega_{LO}} + \Delta$, where Δ is the increase in the ground energy of QD # 5 (few meV) due to doping. The change in wavefunction of QD # 5 is negligibly small. In this work only the ground state in each QD # I, denoted by $|i_g, 0\rangle$, is considered. Such contribution is attributed to the following reasons; first, the electron's transition from the 'zero-region' to the ground state $|1_g, 0\rangle$ is 100 times faster than the transition to the excited state $|1_e, 0\rangle$. In addition, the transition to $|5_g, 0\rangle$ is 10 times less than the transition to $|1_g, 0\rangle$. As a result, the electron in the 'zero-region' will basically

favour tunnelling toward QD # 1 more than QD # 5. Second, in systems where the energy separation is 44 meV the relaxation takes 20 (40) ps at 300 (100) K [89]. Thus, based on the detailed balance condition, $\frac{W_{nm}}{W_{mn}} = e^{-\frac{\hbar\omega_{nm}}{k_B T}}$, phonon-assisted excitation will take much more time. Nevertheless, in the aforementioned configuration, based on the dimensions of the QDs, the energy separation is more than 64 meV. Third, in polar semiconductors, even at room temperature, the emission of LO phonon is more favourable than the absorption of LO phonon. As a result, the $|i_g, 0\rangle$ state does not show any exponential decay and excited states can be neglected.

Next, we show that the escape rate is negligibly small. The escape of the trapped electron to QDs # 2, 4 or 5 can be calculated by considering a multi-phonon process. For both QDs # 2 and # 4, absorption of LO phonons are required. As mentioned previously, the emission rate is still higher than the absorption rate even at room temperature. The escape time to QD # 5 via the emission of LO phonons takes more than few μs. This can be shown from the following second-order contribution to the escape rate τ. For a LO + LA processes (one LO phonon is emitted in addition to an LA phonon),

$$\frac{1}{\tau} = \frac{2\pi}{\hbar}\sum_{\boldsymbol{q}}\sum_{\boldsymbol{k}}\left|\sum_{s}\left(\frac{\boldsymbol{M}_{\boldsymbol{q}}^{is}\boldsymbol{M}_{\boldsymbol{k}}^{sf}}{E_i - E_s - \hbar\omega_q} + \frac{\boldsymbol{M}_{\boldsymbol{k}}^{is}\boldsymbol{M}_{\boldsymbol{q}}^{sf}}{E_i - E_s - \hbar\omega_q}\right)\right|^2 (N_q + 1)(N_k + 1)\,\delta(E_0 - \hbar\omega_q - \hbar\omega_k) \tag{3-15}$$

where **q** and **k** refer to the LO and LA modes respectively. N_q is the Bose distribution function $\boldsymbol{M}_{\boldsymbol{q}}^{if}$ is the form factor matrix element, which reads;

$$\boldsymbol{M}_{\boldsymbol{q}}^{if} = \alpha_{\boldsymbol{q}} \langle i | e^{i\boldsymbol{q}.\boldsymbol{r}} | f \rangle \tag{3-16}$$

with $\alpha_{\boldsymbol{q}} = M_0/q\sqrt{\Omega}$ for the Fröhlich interaction, $\alpha_{\boldsymbol{q}} = D\sqrt{\mathrm{q}/\rho \mathrm{c}\Omega}$ for the deformation interaction. Ω is the volume of the QD, ρ is the density 5.36 g/cm^3 and c is the sound of velocity 5.15 × 10^3 m/s [81]. $M_0 = 0.15$ is the Fröhlich coupling constant [82, 90]. The acoustic deformation potential $D = 6.7$ eV [81]. The form factor for either QD # 3 and QD # 4 or QD # 3 and QD # 5 is very small, leading to an escape rate of the order of few μs. In this model, we calculate all ten hopping integrals (Section 3.4). Since $|i_g, 0\rangle$ states are only considered the hopping terms will not be reduced by the factor $e^{-2\lambda^2/(\hbar\omega_{LO})^2}$because of the weak ELOPI, so the electron hops without a phonon cloud. Based on the *electron pocket* configuration, t_{24} is larger than t_{43} + t_{32}. This is however impossible to achieve in a similar configuration without an *electron pocket*.

3.4. Calculation of hopping matrix elements

The total Hamiltonian of our system is

$$H_t = -\frac{\hbar^2}{2m^*}\nabla_{3D}^2 + V(r,z) \tag{3-17}$$

where the first term is the kinetic energy and the second term is the potential energy

$$V(\boldsymbol{r},z) = \sum_i V_i \tag{3-18}$$

The potential V_i represents the local potential of the QD # i. This representation can be used to derive the tight-binding Hamiltonian H_I given in Eqn. (3-2) for the 'intrinsic-region'. We provide an approximation to H_I in Appendix D. The diagonal and off-diagonal elements of H_t are given by

$$\epsilon_i = -\int \Psi_i^* \frac{\hbar^2}{2m^*} \nabla_{3D}^2 \Psi_i d^3r \; + \int \Psi_i^* V_i \Psi_i d^3r \tag{3-19}$$

and

$$t_{ij} = -\int \Psi_i^* \frac{\hbar^2}{2m^*} \nabla_{3D}^2 \Psi_j d^3r \; + \int \Psi_i^* V_i \Psi_j d^3r \tag{3-20}$$

respectively. These are the variables that enter the tight-binding Hamiltonian H_I in Eqn. (3-2). Due to the cylindrical symmetry of the QDs we can write the wave function as,

$$\Psi = R(\rho)\Phi(\varphi)Z(z) \tag{3-21}$$

Since the hopping is only along the axial axis (z-axis), H_t is

$$H_t = -\frac{\hbar^2}{2m^*}\partial_{zz} + V(r,z) \tag{3-22}$$

The hopping integral is calculated in the following manner

$$t_{ij} = \int \mathrm{R}_i^*(\rho)\Phi_i^*(\varphi)\mathrm{Z}_i^*(z) H_t \mathrm{R}_j(\rho)\Phi_j(\varphi)\mathrm{Z}_j(z) d^3r \tag{3-23}$$

Separating variables will yield

$$t_{ij} = \int_0^{2\pi} \Phi_i^*(\varphi)\Phi_j(\varphi) d\varphi \int_0^r \mathrm{R}_i^*(\rho)\mathrm{R}_j(\rho)\, d\rho \int_{-\infty}^{\infty} \mathrm{Z}_i^*(z) H_t \mathrm{Z}_j(z)\, dz \tag{3-24}$$

The azimuthal part will always result in 1. The azimuthal part acts like a selection rule for the electron hopping. Electron, in the considered configuration, hops between states that possess the same ‘m’. Consequently, the hopping will occur among the QDs’ ground states only. The radial integral requires special care especially when the hopping integral has interface with the *electron pocket*

$$\int_0^{\gamma r} \mathrm{R}_{iin}^*(\rho)\mathrm{R}_{jin}(\rho)\, d\rho + \int_{\gamma r}^{r} \mathrm{R}_{iout}^*(\rho)\mathrm{R}_{jout}(\rho)\, d\rho \tag{3-25}$$

Since H is Hermitian, $t_{ij} = t_{ji}^{*}$. The values of the hopping integral vary based on the QDs. The electron's hopping from QD # 1 to # 2 t_{21}, and vice versa, t_{12} is 161 meV. t_{54} and t_{45} are 180 meV. t_{31} and t_{13} are 14 meV. t_{53} and t_{35} are 5 meV. t_{41} and t_{14} are 24 meV. t_{25} and t_{52} are 0.464 meV. t_{51} and t_{15} are 0.1047 meV. t_{32} and t_{23} are 56.44 meV. t_{34} and t_{43} are 18.6 meV. And finally, t_{42} and t_{24} are 85.7 meV.

Moreover, the NR's minor radius is 15.1 nm, and the circumference of almost 190 nm. The length-to-width ratio is almost 7 justifying the 1-D density of states (DOS) employed in this work. The DOS is as follows

$$\rho^{1D}(E) = \sum_{i=1}^{n} \left(\frac{2m^{*}}{\hbar^{2}}\right)^{1/2} \frac{1}{\pi(E - E_i)^{1/2}}\, \Theta(E - E_i), \tag{3-26}$$

where Θ is a step function. The DOS graph is plotted in Fig. 3-3.

3.5. Electron trapping as a function of temperature

In the numerical calculations using Eqn. (3-14) the trace of the density matrix is equal to one at all times. This assures that the particle conservation principle is not broken. Moreover, it implies that the Hamiltonian is Hermitian. In Fig. 3-4, at $t = 0$, $\rho_{SES} = 1$, hence there is no electron in the configuration. In addition, when there is no decoherence, the probability of the electron to get trapped in the central QD is 27%. On the other hand, when decoherence comes into action, the electron's trapping probability does increase to 58-70% depending on the temperature (see Figs. 3-4 and 3-5). The probability of the electron's trapping at different temperatures and their corresponding dephasing times are shown in Table 3-1.

Table 3-1: Probability of electron being trapped in the central quantum dot at various temperatures between 100 and 300 K.

Temperature / K	Dephasing time T_2	Electron trap / %
100	2 ps	70
150	667 fs	65
200	500 fs	63
250	334 fs	60
300	285 fs	58

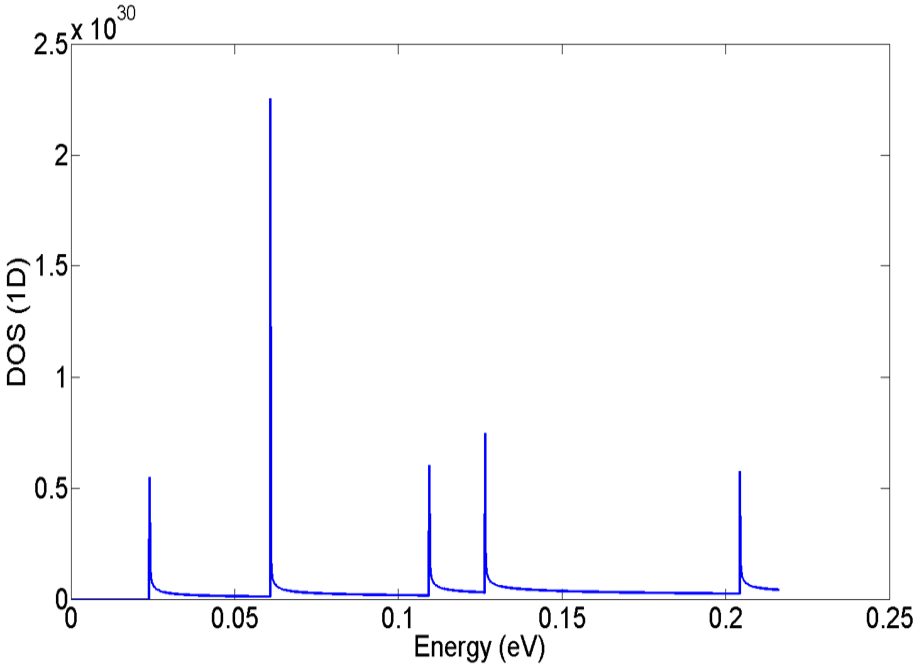

Figure 3-3: Density of states for a circular nanowire with radius of 15.1 nm.

Although as the dephasing rate increases the trapping probability decreases, it is larger than the zero-decoherence case. Many factors contributed to this counter-intuitive result. First factor is the *electron pocket*, which is essential for the electron to get accumulated in the central QD. To

show the importance of the *electron pocket*, consider the following figure where there is no *electron pocket* (i.e. $t_{42} < t_{43}$ and t_{32}). The electron is delocalized among all five QDs. In Fig. 3-6, the same eigenenergies and same hopping matrix elements values were exactly considered but t_{42}, the result is due to the detuning of the energy levels of the QDs. However, there is no significant localization of the electron in QD # 3. Second factor is the fast electron transition from the 'zero-region' to QD # 1 and from QD # 5 to the 'zero-region'. The electron's transition rate from the 'zero-region' to the first QD's ground state $W_{0\rightarrow 1_g}$ is almost 100 times larger than $W_{1_g\rightarrow 0}$. The electron's transition rate from the ground state of QD # 5 to the 'zero-region' $W_{5_g\rightarrow 0}$ is almost 10 times larger than $W_{0\rightarrow 5g}$, this is due the *n*-doping of QD # 5.

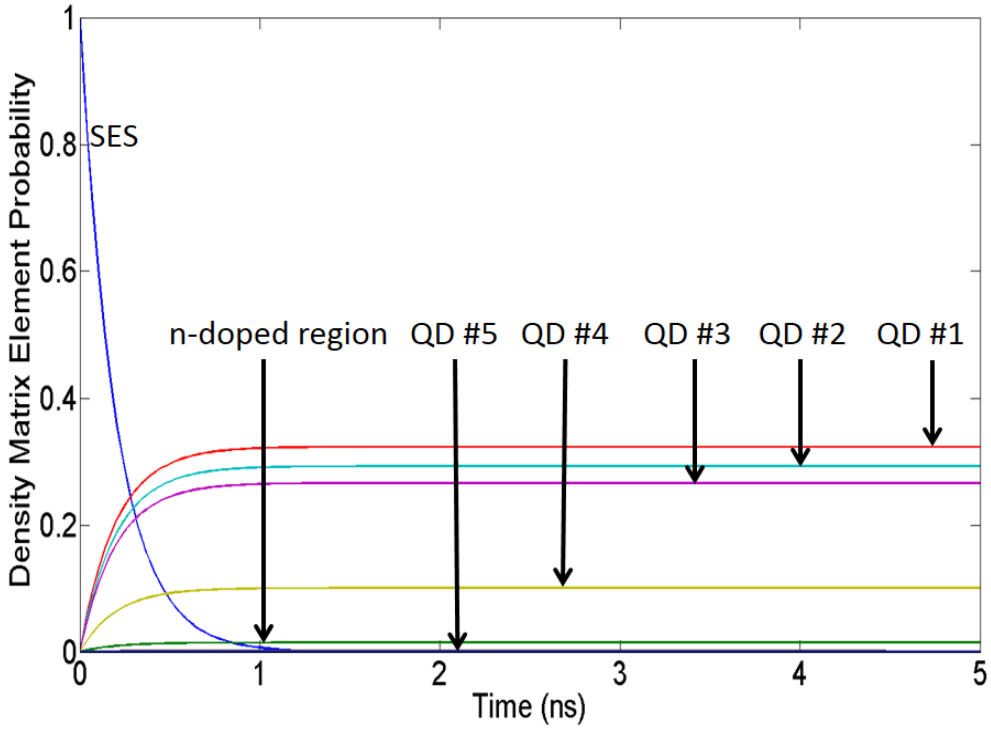

Figure 3-4: The electron's time-dependent probability distribution among the five quantum dots in the zero-decoherence case.

In this work, both $W_{0\rightarrow 1_g}$ and $W_{5_g\rightarrow 0}$ are 9.5×10^{13} s^{-1} and 2.0×10^{14} s^{-1}, respectively. These fast transitions are achieved through two factors: the density of states of the NR and the *n*-doping of the 'zero-region' and QD # 5. Another contributing factor is the QDs' eigen energies relative to each other, i.e. if any of the QDs' energy level is modified without adjusting the other QDs' eigen energies, the trapping efficiency will decrease. Furthermore, the central QD's eigenenergy is the second lowest among all QDs but QD # 5. Based on the geometry and the dimensions of the QDs, the energy difference between the central QD's eigenenergy and the neighbor QDs' eigen energies is almost 65 meV. This means the trapped electron needs to absorb two LO phonons in addition to LA phonon to be able to escape. On the other hand, in order for the trapped electron to escape to QD # 5 ground state, an energy difference of 86 meV need to be overcome by the emission of at least 2 LO phonons in addition to LA phonons. Even with a strong ELOPI, these processes take more than 1ns [91].

Once the electron gets injected from the 'zero-region' to the QD # 1, it keeps hopping among the five QDs. As shown in section 3.4, both t_{21} and $t_{54}$are of the order of 170 meV, which means the electron hopping is faster than the phonons response. However, due to the presence of the *electron pocket*, i.e. $t_{42} > t_{43} + t_{32}$, the electron hops faster between QD # 2 and QD # 4 than hopping between QD # 2 and QD # 3, so electron trapping due to detuning is excluded. Meanwhile, due to the relatively smaller values of t_{43} and t_{32}, part of the electron's wave slowly keeps accumulating inside the central QD, while the rest of the electron's wave hops to QD # 4 from QD # 2 then fast to QD # 5 then to the 'zero-region'.

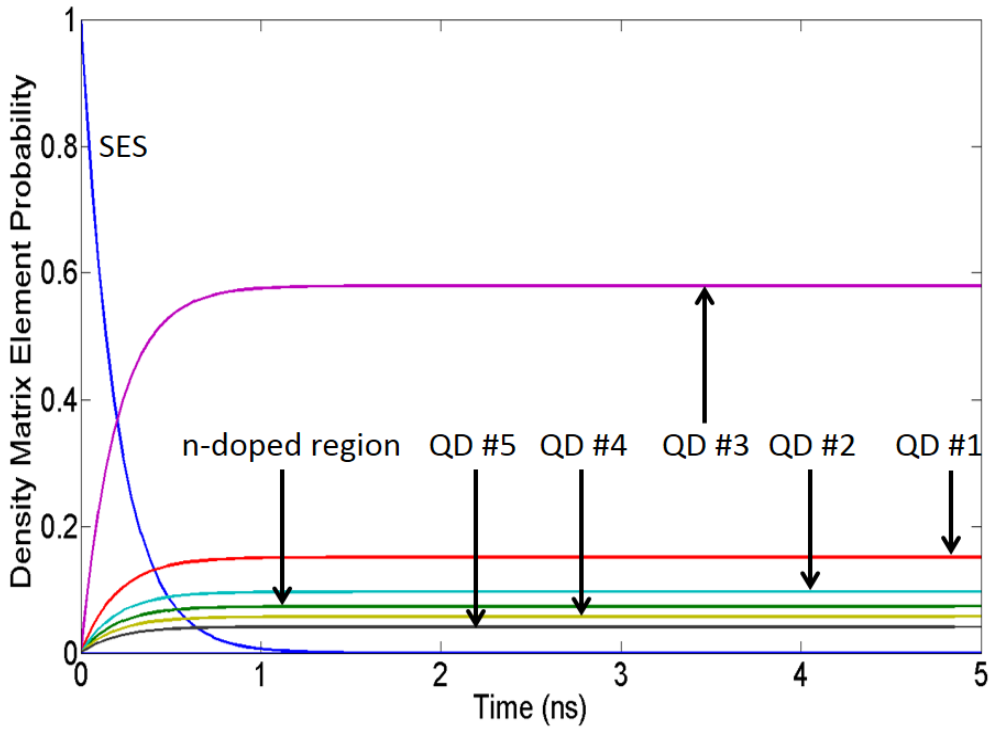

Figure 3-5: The electron's time-dependent probability distribution among the five quantum dots at room temperature.

From 'zero-region' to QD # 1 again, and the revolved electron's wave interference constructively with the part that remained in the *electron-pocket* leading to a localization of the electron. However, the localized electron will not stay inside QD # 3 leaving behind 27% probability of trapping. The trapping probability depends on when decoherence will terminate the hopping, i.e. off-diagonal terms, between QDs. At 100 K, the electron gets accumulated inside QD # 3, before the electron starts to hop out of QD # 3, the decoherence destroys the electron's hopping, hence the electron is trapped with a trapping probability of 70%. At 300 K, decoherence is much faster than 100 K, the electron, while being accumulated inside QD # 3, the decoherence kicks and destroys the continuation of accumulation, thus the trapping efficiency decreases to 58%. The whole mechanism is based on a configuration that constructively localize the electron inside

the central QD through the quantum interference of the electron with itself, then counts on decoherence to ban the electron from hopping out. Therefore, trapping an electron inside QD # 3 requires a delicate balance between how fast the electron is accumulated versus how fast the decoherence kicks in. Such physical mechanism should manifest itself through oscillations in the diagonal density matrix elements in Fig. 3-3. The absence of oscillations due to the above explanation is attributed to the strong damping of the decoherence. However, check Appendix D, when the electron's initial state is $|1_g, 0\rangle$ instead of $|SES\rangle$, the oscillations reflecting the electron's dynamics will be visible and clear as shown in Fig. 3-7.

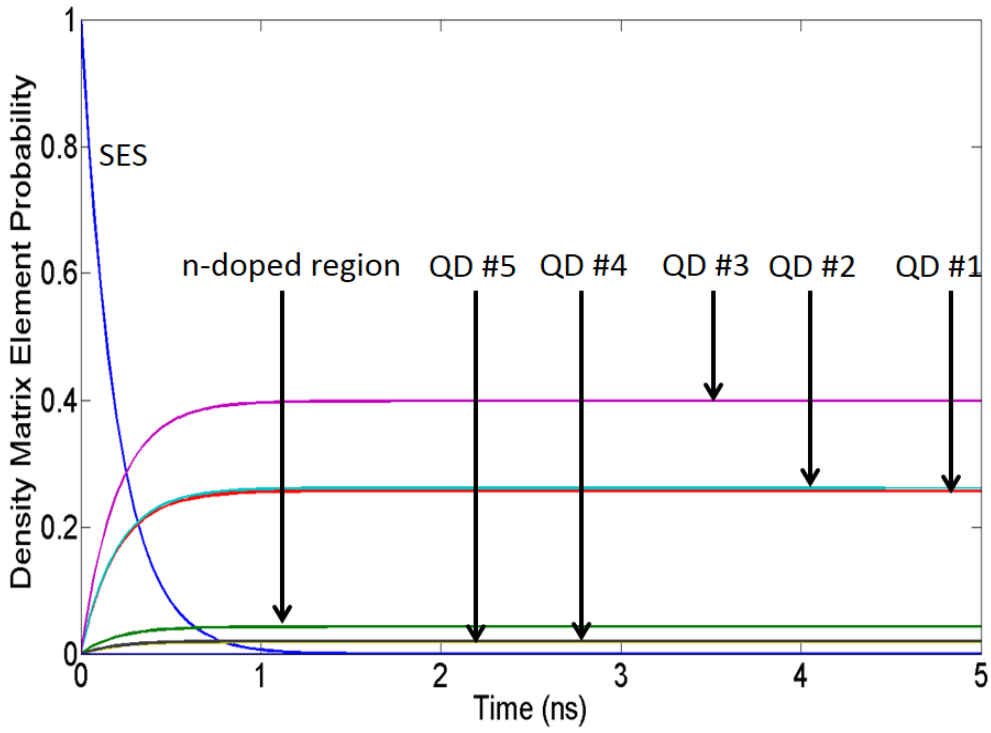

Figure 3-6: The electron's time-dependent probability distribution among the five quantum dots, at T = 300K without electron pocket.

It is important to note that the shown electron trapping takes place as a result of the interplay of both decoherence and quantum interference, neither of them can achieve electron trapping alone. In addition, as mentioned previously, the electron will require two LO phonons in addition to 1 LA phonon to be able to escape to the next QDs. Since there is neither a model nor an experimental implementation of electrically driven single-photon source in the telecommunication range at room temperature [92], this configuration provides an efficient trapping scheme that could be implemented as a suitable candidate for an electrically driven single photon source operating at high temperature (100 – 300 K).

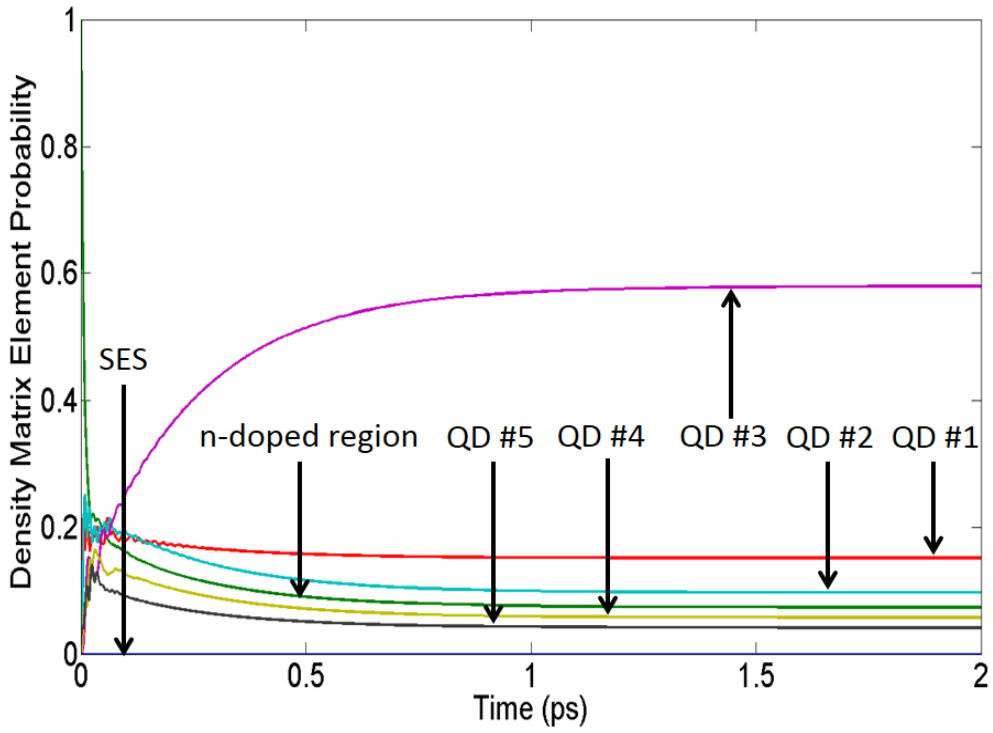

Figure 3-7: The electron's time-dependent probability distribution among the five quantum dots at room temperature with $\rho_{11} = 1$ as initial condition.

3.6. Summary

In this chapter, a realistic configuration to trap an electron at high temperature (100 – 300 K) taking advantage of the interplay between quantum interference and decoherence phenomenon in an electron-pocket configuration is presented. The trapping is achieved with a probability ρ_{33} depending on the temperature. At T = 100 K, 200 K, and 300K the trapping probability is $\rho_{33} = 70\%, 63\%,$ and 58%, respectively. Furthermore, our model could be used to implement an efficient electrically driven single photon source operating at wavelengths $\lambda = 1.3 - 1.5$ μm and between 100 and 300 K. We mention that we do not consider the photon collection efficiency in a cavity, which is beyond the scope of this work. Regarding the experimental realization of the proposed setup, heterostructure nanowires with different materials and sizes have been fabricated with high control and precision [93]. It has demonstrated experimentally that broad bandgap materials such as PMMA can be grown in GaAs [94]. Furthermore, different research groups have reported the ability to turn nanowires into nanorings through nanomanipulation [95]. We conclude that, based on the current experimental techniques, the presented setup is experimentally feasible.

The presented setup is robust within about ± 1 nm variations in sizes of the QDs and barriers. Coulomb blockade does not play any role in this work. The main advantage of the decoherence-assisted trapping is that it happens on a time scale of sub-picoseconds. The reason for this fast trapping is that the trapping happens dynamically due to decoherence and does not require the switching of any external voltage. The dynamics inside the 5 QDs is illustrated in Appendix E (see Fig. 3-7). When a SES is used, it takes on the order of 1 ns for the full probability of the electron to be trapped, as shown in Fig. 3-4, because the SES switching time is on the order of 1 ns. However, the internal dynamics inside the 5 QDs is on the sub-picosecond time scale (Fig. 3-7).

There is no voltage switch that can reach sub-picosecond time scales. In addition, the trapping due to decoherence isolates the electron in QD # 3 strongly from the leads due to the presence of the surrounding QDs # 1, 2, 4, and 5.

CHAPTER 4: ELECTRICALLY DRIVEN SINGLE PHOTON SOURCE AT HIGH TEMPERATURE

4.1 Introduction

In recent years, single photon sources (SPSs) have attracted a lot of attention [99, 100]. The single photon plays a crucial role in both the fields of quantum mechanics and quantum measurement theory [101]. An efficient reliable SPS is an essential element for the implementation of photonic quantum information processing, quantum key distribution, and quantum repeaters [100, 102, 103]. SPSs have been implemented with non-linear crystals using parametric down conversion [104, 105], ion traps [106, 105], quantum dots [108], and N-V centers in diamond [109]. In general, they are either optically driven single photon sources (OSPS) [110] or electrically driven single photon sources (ESPS) [111, 112]. The idea of an electrically driven SPS, based on Coulomb blockade, was first proposed by Yamamoto's group in 1994 [113]. Since then, many groups have managed to construct such sources [114-118], nevertheless, cryogenic temperatures are essential for the performance of such sources. Some groups managed to construct electrically driven SPS operating at room temperature using diamond [119]. However, the emitted photons have wavelength in the range of 575 – 637 nm, hence they exist outside the telecommunication range (1.3 – 1.5 μm), in which attenuation is lowest in an optical fiber. One of the main weaknesses of SPSs based on the parametric down-conversion is the probabilistic timing of the single-photon generation [100]. While ion traps do not suffer from timing issues, they require cryogenic cooling to mK level [120]. OSPS based on quantum dots and N-V centers provide reliable timing of single-photon generation and operation at high temperature [121, 122]. In comparison with OSPSs, ESPSs are simpler, less expensive, can be fully miniaturized and

integrated on a chip [100]. However, there are several drawbacks, such as finite carrier injection (which leads to multi-photon emission), coupling to high-Q cavities and most importantly the poor performance at temperatures above 70 K [111]. While OSPSs can operate efficiently at higher temperatures, nevertheless so far no OSPS can emit photons in the telecommunication range (1.3–1.5 μm). ESPS can emit photons in the telecommunication range [123]. Consequently, a single photon source operating at high temperatures, in the telecommunication range, is not available because of the aforementioned trade-off between OSPS and ESPS.

In this chapter, we present a novel scheme for an ESPS operating efficiently at high temperatures and emitting a single photon in the telecommunication range. The photon is emitted as a consequence of the recombination of an electron and a hole in a quantum dot (QD). The novel feature in our proposed ESPS is that we take advantage of decoherence, a consequence of electron-phonon interaction for the controlled emission of a single photon [124]. Although being counterintuitive, our scheme shows clearly that while in the case of zero decoherence single-photon emission probability is 35%, in the case of decoherence due to electron-phonon interaction, the photon emission probability is almost 100% with a strong antibunching behavior, i.e. $g^{(2)}(0) \ll 1$. The antibunching is ensured by the single electron source (SES) that electrically drives our SPS. Remarkably, the photon emission is facilitated by both quantum interference and decoherence. The electron's dynamics is described using the generalized master equation with a Hamiltonian based on the tight-binding model, taking into account the electron-LO phonon interaction (ELOPI). The photon emission is studied in both Rabi and Purcell regimes. The second-order correlation is calculated using the quantum regression theorem. We obtain strong antibunching behavior at high temperatures up to 300 K.

In the previous chapter, the transport of a single electron in a nanoring (NR) is discussed. For this chapter, the same structure is employed, where the NR is comprised of two regions, the n-doped $In_{0.45}Ga_{0.55}As$ and the InAs hosting the five quantum dots (QDs) with the exception of the central QD with $In_{0.5}Ga_{0.5}As$ p-doped composition. The setup is intentionally designed to exploit the central QD as an *electron pocket*, resulting in a decoherence enabling electron trapping. A detailed schematic of the second region is shown Fig. 3-1. The details of the structure and a detailed conduction band profile is elaborated in Chapter 3. The electrons are injected to the aforementioned setup via a single-electron source (SES) (see appendix F) [78, 79]. The time evolution in this case is described by means of a single-electron generalized master equation, because a single electron is ejected from the SES when it is triggered electrostatically by means of a gate voltage. This injected electron then moves through the whole configuration.

4.2. Model

The mechanism involved in Fig. 3-1 can be described qualitatively as follows; the SES is attached to a NR. This NR is embedded in a microcavity (not shown in Fig. 3-1). An electrostatic pulse on the gate voltage of the SES triggers the emission of a single electron into the NR. This electron propagates for few picoseconds in the NR until it gets trapped in QD # 3 by means of decoherence and quantum interference. A heavy hole is presented in QD # 3 because of the δ doped QD # 3. The trapped electron recombines with the heavy hole, resulting in the emission of a photon. Both Purcell and Rabi regimes are discussed later. The minimum of the conduction band of InAs QDs is set to be the zero energy.

The single photon emission is enhanced by means of a cavity. Therefore, the model Hamiltonian has an extra term that was absent in the Hamiltonian in Eqn. 3-1. This extra term

considers the interaction of the quantized mode of the cavity and the photon emission. The new total Hamiltonian is given;

$$H = H_I + H_{JCM} + H_c \tag{4-1}$$

where H_I is the Hamiltonian of an electron in the intrinsic region and reads

$$H_I = \sum_i \varepsilon_i a_i^\dagger a_i + \left(-\sum_{i \neq j} t_{ij} a_i^\dagger a_j + h.c \right) + \hbar\omega_{LO} b^\dagger b + \lambda \sum_i a_i^\dagger a_i (b^\dagger + b) \tag{4-2}$$

H_{JCM} is a Jaynes-Cummings like Hamiltonian that describes the interaction between two levels system (QD # 3) and a photon in a cavity. The two levels are the electron's ground state in QD # 3 and the heavy hole's ground state in QD # 3. H_{JCM} is written as;

$$H_{JCM} = \hbar\omega_O (c^\dagger c + \pi^\dagger \pi) + \hbar\Omega (\pi^\dagger a + a^\dagger \pi) \tag{4-3}$$

where c is the annihilation operator for the photons inside a cavity and π is the transition lowering operator of QD # 3. ω_0 is the transition frequency of QD # 3. Ω is the coupling constant. H_C is the Hamiltonian of the coupling between both QD # 1, # 5 and the zero-region;

$$H_c = \left(\sum_0 V_{01} C_0^\dagger a_1 + h.c \right) + \left(\sum_0 V_{05} C_0^\dagger a_5 + h.c \right) \tag{4-4}$$

In Eqn. (4-2), the first term describes the on-site ground state for the five QDs. The hopping of the electron between the QDs is represented by the second term, where t_{ij} is a 3D hopping integral given by the off-diagonal matrix elements of H_t [80], i.e.

$$t_{ij} = \int \Psi_i^* H_t \Psi_j d^3r \tag{4-5}$$

where H_t is the kinetic and potential energy of the electron inside the QD,

$$H_t = -\frac{\hbar^2}{2m^*}\nabla_{3D}^2 + V(r,z) \tag{4-6}$$

The third term in Eqn. (4-2) quantifies non-dispersive LO phonons of $In_{0.45}Ga_{0.55}As$, because it makes up 85% of the NR. A canonical unitary transformation can be applied to eliminate the linear coupling terms. The transformed Hamiltonian is $H_I' = e^S H_I e^{-S}$, where $S = -g\left(\sum_i a_i^\dagger a_i (b^\dagger + b)\right)$. Thus

$$H_I' = \sum_i a_i^\dagger a_i \left(\varepsilon_i - \lambda^2/\hbar\omega_{LO}\right) + \left(-\sum_{ij} t_{ij} a_i^\dagger a_j e^{-2g(b^\dagger - b)}\right) + \left(-\sum_{ij} t_{ji} a_j^\dagger a_i e^{-2g(b^\dagger - b)}\right) + \hbar\omega_{LO} b^\dagger b + (2\lambda^2/\hbar\omega_{LO}) \tag{4-7}$$

In equation 4-7 the first term shows the renormalization of the QDs eigenstates as a result of the strong ELOPI. The eigenstates of the transformed Hamiltonian H_I' are in the tensor product form and are denoted by $|i, N, n\rangle$ where i, N, and n represent the state of the electron, the number of LO phonons, and the number of photons, respectively. The hopping of the electron, coupled to the LO phonons, among the QDs is described rigorously in Chapter 3.

For the scheme presented here, initially there should not be any electrons in the CB. The electron density is given by;

$$n = \int_{E_C}^{\infty} D(E) f^{FD}(E) dE \tag{4-8}$$

The considered NR has a large length-to-width ratio, so D(E) is estimated by the density of states of a 1D NR [124]. The doping (both type and concentration) along with the temperature are part of the Fermi–Dirac function $f^{FD}(E)$. We compute that there are virtually no electrons in the whole configuration. The mechanism of the triggering of the SES and the emission of a single electron are accurately described by $H_I^{'}$. In addition, H_c describes the coupling between the zero-region (quasi-continuum) and QDs # 1 and # 5. The coupling to the zero-region is described by Fermi' s golden rule,

$$W_{i\to j} = \frac{2\pi}{\hbar}\int_{E_C}^{\infty} dE_i |\langle j|H_C|i\rangle|^2 D(E_i) f^{FD}(E_i) \times (1 - f^{FD}(E_i))\delta(E_j - E_i) \quad (4\text{-}9)$$

where i corresponds to the zero-region state, while j denotes the states of either QD # 1 or # 5. The coupling terms in Eqn. (4-4), V_n and V_p, are much smaller than t_{12} and t_{45}. This demonstrates that we have a weak coupling between both QDs # 1 and # 5 and the leads. Therefore, a standard formalism suitable for the description of such a system is the generalized master equation in the Born and Markov approximation [85, 125] given by;

$$\partial_t \rho_{m,n} = \frac{i}{\hbar}[\rho, H_I']_{m,n} + \frac{i}{\hbar}[\rho, H_{JCM}]_{m,n} + \delta_{m,n}\sum_{l\neq m}\rho_n W_{m,l} - \gamma_{m,n}\rho_{m,n} + \alpha\left(c\rho c^{\dagger} - \frac{1}{2}c^{\dagger}c\rho - \frac{1}{2}\rho c^{\dagger}c\right) \quad (4\text{-}10)$$

where the total decoherence, including the dephasing time T_2 due to electron–phonon (both acoustic and optical, and both elastic and inelastic) interaction and the rates $W_{m,l}$ of transition between the leads and the outer QDs, is quantified through $\gamma_{m,n} = \frac{1}{2}\sum_l (W_{l,n} + W_{l,m}) + \frac{1}{T_2}$, α is the photon's decay rate out of the cavity.

4.3. Electron trapping mechanism

The emission of a single photon requires the presence of a single electron–hole pair in a QD for sufficient time until recombination takes place and the photon is emitted. A heavy hole is located in the central QD as result of the δ p-doping. An electron is trapped in the central quantum dot by means of decoherence and interference. Since the photon cannot be emitted unless there is an electron in the central quantum dot, decoherence plays a crucial role in the emission of the photon. Once the electron is injected into the NR, it travels in both directions, since there is no electric field to force the electron to favor either arm. While the electron propagates through both arms simultaneously, the electron tunnels to the heterostructure region through both sides. The tunneling rates in the two arms are not equal, as elaborated below. Once the electron tunnels in the heterostructure region through both sides, the electron keeps hopping from QD # 1 to QD # 5 through the intermediate QDs. The hopping rates are carefully designed. The hopping rate between QD # 2 and QD # 3 is relatively low compared to the hopping rate between QD # 2 and QD # 4. In addition, the hopping rate between QD # 3 and QD # 4 is lower than the hopping rate between QD # 2 and QD # 4. As the electron revolves in the NR, the amplitude of the electron's wavefunction gradually builds up in QD # 3. However, this steady accumulation cannot be maintained in QD # 3 as a result of the hermiticity of the Hamiltonian. The electron's wavefunction goes outside the heterostructure region to the rest of the NR. It is worth to mention that even at room temperature, the decoherence does not prevent the electron from tunneling for the second time. As the electron tunnels to the hetreostructure region for the second time from both sides, it interferes with the built-up amplitude in QD # 3. This interference contributes to the significant increase in the electron's density matrix element in QD # 3. Nevertheless, this increase would not

last in the quantum dot unless decoherence is active. Without the decoherence, the accumulated wavefunction hops outside QD # 3. Decoherence inhibits the accumulated electron amplitude to get out of QD # 3.

The role of decoherence in the trapping of the electron is demonstrated by comparing the electron's trapping probability in the central QD in the cases when there is decoherence, as shown in Fig. 3-5, and when there is no decoherence, as shown in Fig. 3-4. Thus, in the absence of the decoherence, there is no significant trapping of the electron. On the contrary, the electron's probability is distributed mostly among QDs 1– 3. As shown in Fig. 3-5, the electron's trapping is significantly enhanced in the presence of decoherence. The role of the decoherence can be clearly shown by comparing the photon emission' s probability in Fig. 4-1 and Fig. 4-2. When decoherence is absent, the photon emission probability is almost 35%. In contrast, when decoherence in present, the probability for the photon to be emitted is 100%. Consequently, if there is no significant electron trapping probability, the probability for emission of the photon is low. As a consequence of the hermiticity of the Hamiltonian, the trace of the density matrix is equal to one at all times in the numerical computations using Eqn. 4-10. In Fig. 4-1, at t = 0, $\rho_{SES} = 1$, indicating the absence of any electron in the configuration. Moreover, if decoherence is zero, 27% is the probability for an electron to get trapped in the central QD as shown in Fig. 3-4. In contrast, if decoherence is considered, the electron' s trapping probability increases to 70%– 58% depending on the temperature (100– 300 K) [124].

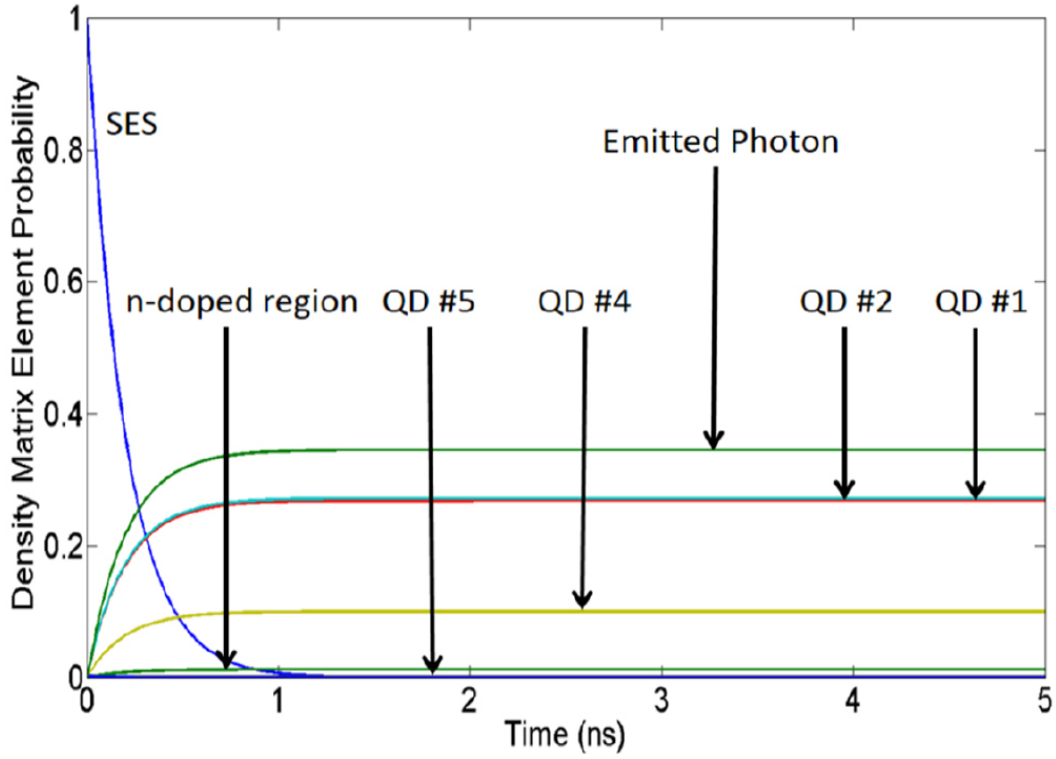

Figure 4-1: The electron's time-dependent probability distribution among the five quantum dots and the photon's emission probability at room temperature. The emitted photon shows the probability of a single photon after leaving the cavity.

Although decoherence is necessary to trap the electron, it is essential to have interference inside the nanostructure. The successful trapping is achieved by means of a delicate balance between decoherence and interference. Several aspects lead to this counter-intuitive result. The first aspect is the *electron pocket*, which is substantial for the electron to get accumulated in the central QD *via* interference. The second aspect is the fast electron transition from both the zero-region to QD # 1 and from QD # 5 to the zero-region. These fast transitions are realized through two factors: the n-doping of the zero-region and QD # 5 and the density of states of the NR. The third aspect is that the central QD's eigenenergy is the second lowest among all QDs but QD # 5. The energy difference between the central QD's eigenenergy and the neighboring QDs' eigen energies is

almost 65 meV. Thus, the trapped electron is required to absorb two LO phonons in addition to LA phonon to be able to escape. In order for the trapped electron to escape to QD # 5 ground state, an energy difference of 86 meV needs to be overcome by means of the emission of at least 2 LO phonons in addition to LA phonons. Even with a strong ELOPI, these processes take more than 1 ns [91]. The dynamics of the electron's trapping is discussed extensively in Chapter 3.

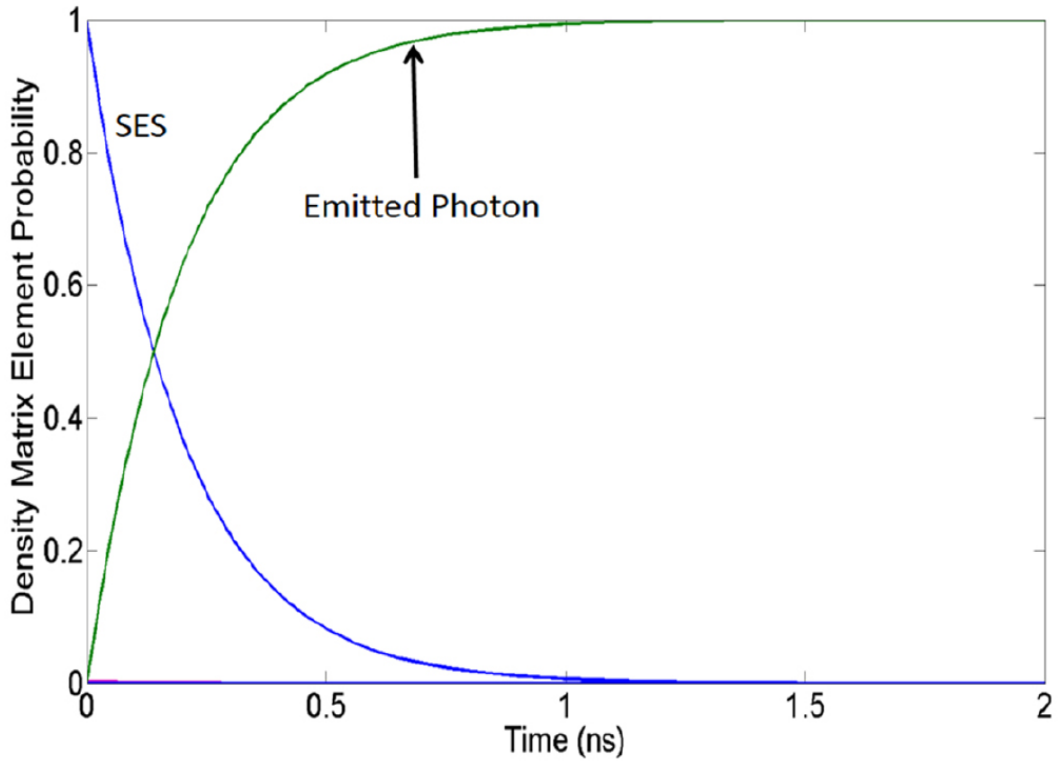

Figure 4-2: The electron's time-dependent probability distribution among the five quantum dots and the photon's emission probability at room temperature. The emitted photon shows the probability of a single photon after leaving the cavity.

4.4. Single photon emission

Figures 4-3 to 4-5 dictate the photon emission probability after being leaked from the cavity. A strong QD-photon coupling (Rabi regime) is achieved when the coupling strength Ω is faster

than any involved dissipation. In this work, the dissipation lies in the dephasing rate $1/T_2$ and the photon decay rate of the cavity α. On the other hand, the weak coupling (Purcell regime) is defined when $\Omega << 1/T_2$ and α . Experimentally, for strong coupling $\Omega \approx 0.08$ meV [126, 127]. No matter the value of α, the dephasing rate $1/T_2$, even at 100 K (1/2 ps), is faster than Ω. Thus, the single photon emission takes place in the Purcell regime.

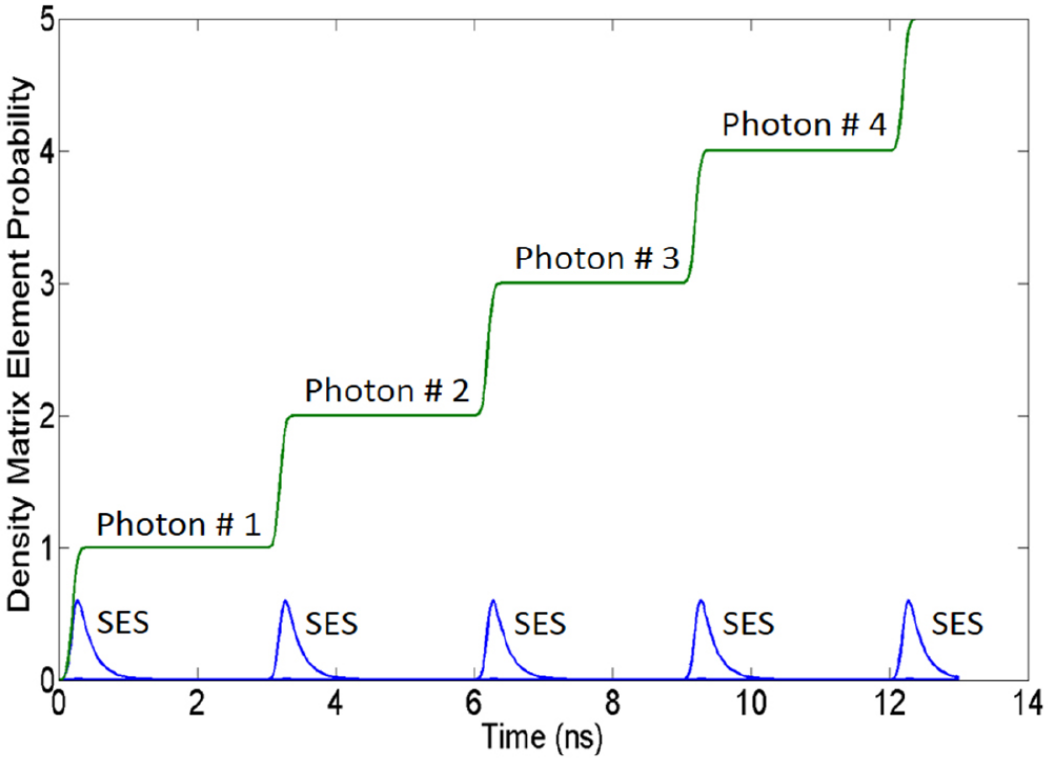

Figure 4-3: Train of electrons resulting in a train of single photon emissions. After every single electron injection, a single photon is emitted. The emitted photon shows the probability of a single photon after leaving the cavity.

Decoherence plays an essential part in the single photon emission. Without decoherence, the probability for the studied configuration to emit a single photon resulting from the injection of the single electron is less than 35%, as shown in Fig. 4-1. In other words, 35% is the probability for a single photon to leave the cavity in the zero-decoherence case. However, once decoherence is

taken into account, the photon emission probability resulting from the injection of the single electron is almost 100% as shown in Fig. 4-2. The photon emission reaches 100% because decoherence enhances the electron trapping in the central QD. In addition, the cavity enhances the electron– hole recombination rate since this recombination takes place in the Purcell regime as explained above in the beginning of this section. Compared with Fig. 4-1, the cavity effect is still effective, nevertheless, decoherence is absent. Consequently, the electron trapping probability is not as high as in the decoherence case, thus a single photon leaked from the cavity will not have more than 35% probability.

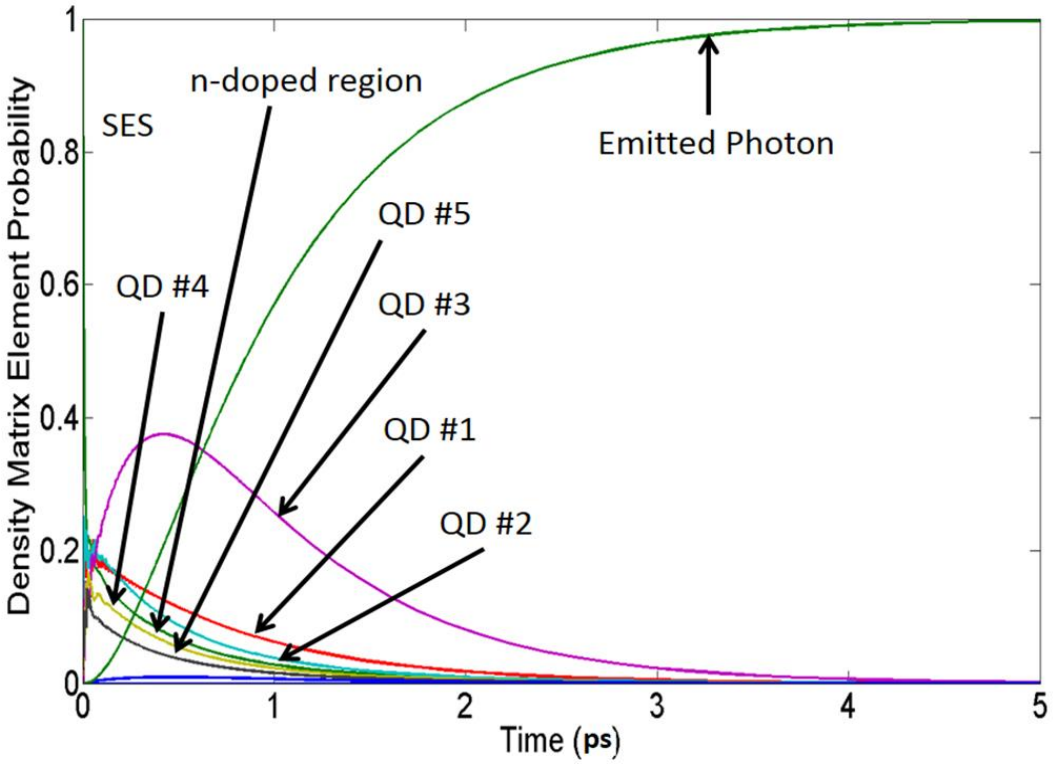

Figure 4-4: The electron's time-dependent probability distribution among the five quantum dots at T = 300 K with $\rho_{zero-region} = 1$ *as initial condition. The emitted photon shows the probability of a single photon after leaving the cavity.*

Experimentally, it is challenging to inject just a single electron using the SES. That is why both Fig. 4-1 and Fig. 4-2 are shown to highlight the role of decoherence in enhancing the photon emission probability from less than 35% to almost 100% at room temperature. The attached SES triggers many electrons (one electron per time interval) over a period of time. As shown in Fig. 4-3, an electron is triggered from the SES every 3 ns and this is obvious from the SES density matrix graph. The injected electron gets trapped by means of decoherence and the interference due to the electron pocket. The recombination is enhanced because of the cavity; hence a single photon is emitted. One requirement is that the QD-photon coupling rate Ω has to be larger than the SES triggering rate so that there is only a single electron in the NR. Behavior of a single electron over the five QDs is shown in Fig 4-4.

In case of the existence of two electrons at the same time in the NR, the considered Hamiltonian will not reflect accurately the physical dynamics of the electrons due to the absence of the Coulomb interaction in the Hamiltonian. In addition, the effect of electron-electron interaction on the trapping mechanism by decoherence and *electron pocket* is beyond the scope of this work.

4.5. Quantum signature of Single Photon Source

SPSs can be characterized by the second-order correlation function $g^{(2)}(\tau)$ [128]. In order to have a SPS, $g^{(2)}(\tau = 0)$ must be much smaller than 1 or equal to zero, which corresponds to sub-Poissonian statistics or antibunching. In order to derive $g^{(2)}$, we start from the second-order correlation function for the electric field, which is formally defined as [129];

$$g^{(2)}(\tau) = \frac{\langle E^-(\mathbf{r}t)E^-(\mathbf{r}t+\tau)E^+(\mathbf{r}t+\tau)E^-(\mathbf{r}t)\rangle}{\langle E^-(\mathbf{r}t+\tau)E^+(\mathbf{r}t+\tau)\rangle\langle E^-(\mathbf{r}t)E^+(\mathbf{r}t)\rangle} \tag{4-11}$$

where τ is the delay time.

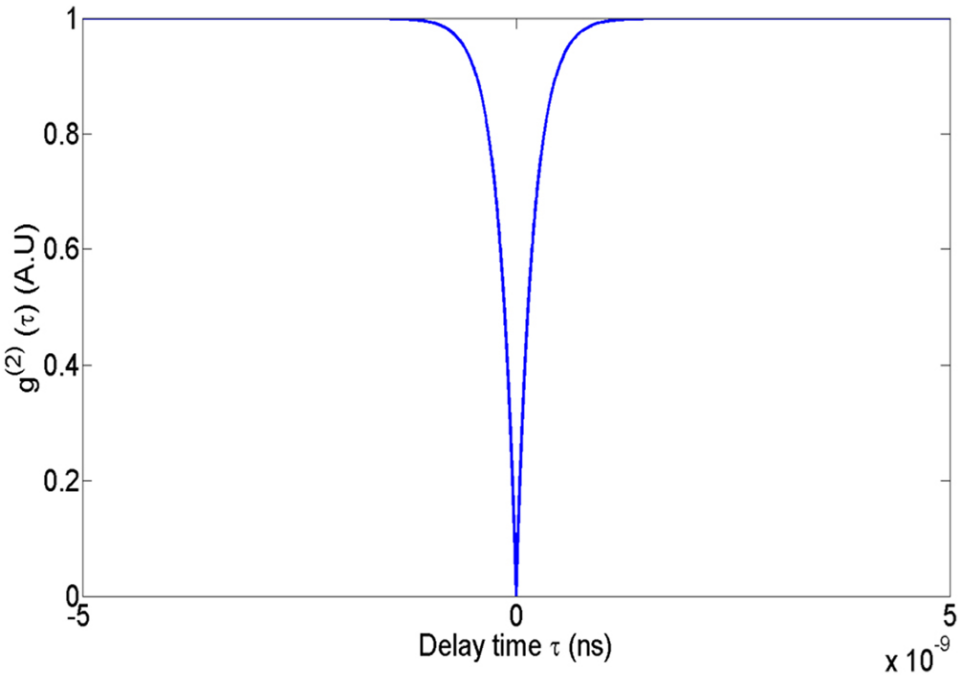

Figure 4-5: Second-order correlation function for the emitted photon from the central QD. $g^{(2)}(\tau = 0) \approx 0$ at room temperature, which indicates strong antibunching.

The electric field can be written in terms of the photon operators c and c† as follows;

$$E^{+}(\mathbf{r}t) = i\sum_{\mathbf{k}} \frac{(\hbar w_{\mathbf{k}})^2}{2V\epsilon_0}\, \epsilon_{\mathbf{k}} c_{\mathbf{k}}(t)\exp(i\mathbf{k}.\mathbf{r}) \qquad (4\text{-}12)$$

and E^{-} is the Hermitian conjugate of E^{+}. Based on the source field relationship, the photon operators can be expressed in terms of the transition operators π and $\pi^{\dagger}$. Thus the electric field can be written as;

$$E^{+}(\mathbf{r}t) = -\frac{e\epsilon_0^2 D_{12}}{4\pi\epsilon_0 v^2|\mathbf{r}-\mathbf{R}|}\pi(t - \frac{|\mathbf{r}-\mathbf{R}|}{v})$$

(4-13)

where v is the speed of light and D_{12} is the electric-dipole matrix element. Consequently, the second-order correlation function in equation (4-11) can be cast in terms of transition operators as;

$$g^{(2)}(\tau) = \frac{\langle \pi^+(t)\pi^+(t+\tau)\pi(t+\tau)\pi(t)\rangle}{\langle \pi^+(t+\tau)\pi(t+\tau)\rangle\langle \pi^+(t)\pi(t)\rangle} \tag{4-14}$$

The expectation value is,

$$\langle \pi^+(t)\pi(t)\rangle = \rho_{33}(t) \tag{4-15}$$

where ρ_{33} is the density matrix of QD # 3. According to the quantum regression theorem [125], the second-order correlation function is

$$g^{(2)}(\tau) = 1 - exp(-(\Gamma + R)\tau) \tag{4-16}$$

where Γ is the electron–hole recombination rate and R is the effective filling rate for QD # 3, taking into account the SES triggering rate, the injection rate, and the trapping rate. As shown in Fig. 4-5, at τ = 0, the second-order correlation function is equal to zero, indicating a strong antibunching behavior. This means that the probability of emitting two photons simultaneously is almost zero.

The second-order autocorrelation function $C^2_{3,3}(\tau)$ is calculated by integrating $\tilde{G}^2(t,\tau)$, i.e.

$$C^2_{3,3} = \lim_{T\to\infty} \int_0^\infty \tilde{G}^2(t,\tau)dt \tag{4-17}$$

Where,

$$\tilde{G}^2(t,\tau) = \langle \pi^+(t)\pi^+(t+\tau)\pi(t+\tau)\pi(t)\rangle \tag{4-18}$$

The second-order autocorrelation function is plotted in Fig. 4-6. The temporal separation between the emission of two successive photons indicates the strong antibunching behavior, with

exceptionally low probability of emitting two photons, of the proposed single photon source.

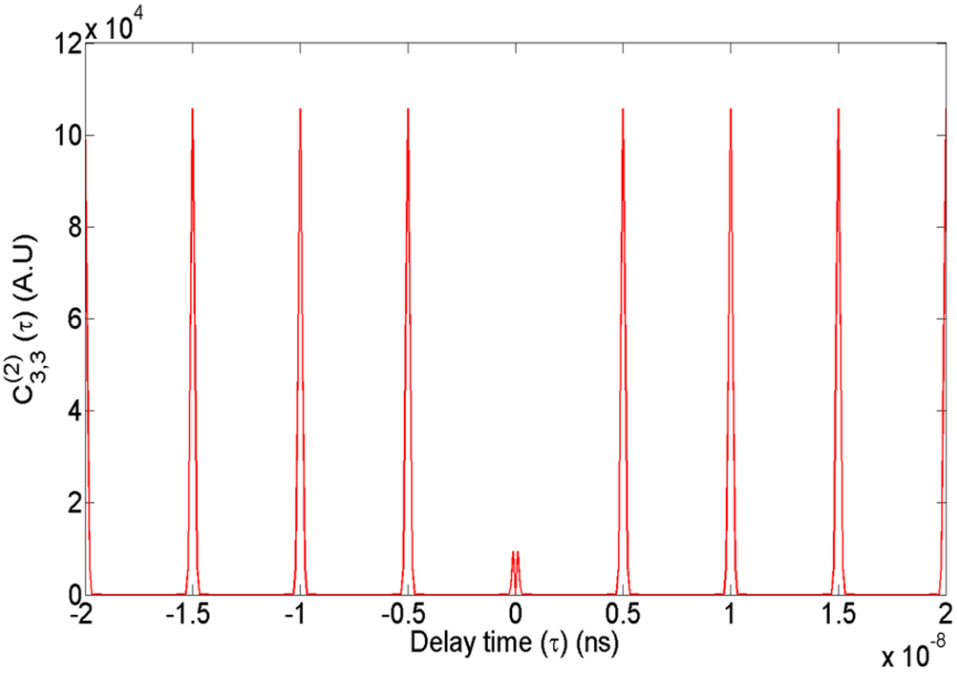

Figure 4-6: Second-order autocorrelation function for the emitted photon from the central QD. This also shows that our proposed SPS has a strong antibunching behavior and extremely low probability of producing two photons per single electron injection at room temperature.

4.6. Summary

In this chapter, I discussed a realistic configuration for an efficient and reliable electrically driven single photon source operating at high temperatures (100 – 300 K). The advantage of this configuration is that it benefits from decoherence to realize a ESPS at high temperature up to 300 K, where current ESPSs fail. While in the case of zero-decoherence the photon emission probability is less than 35%, in the case of decoherence the photon emission probability is almost 100% at high temperature. This result is possible due to our proposed novel physical mechanism

which takes advantage of the combined effect of decoherence and the interference provided by the *electron pocket*. A single photon in the telecommunication range is emitted every 3 ns, which means that our proposed ESPS can operate at GHz frequencies at high temperatures. We show that a single photon is emitted as long as there is decoherence and the electronic injection rate is slower than the quantum dot-photon coupling, no matter whether the ESPS is in the strong-coupling (Rabi) or the weak-coupling (Purcell) regime. In addition, the time scale here is in the picosecond regime, while the timescale for the previous results is in the nanosecond regime.

CHAPTER 5: CONCLUSIONS

In this chapter, comprehensive summary of the projects discussed above is presented. The thesis is comprised of two parts; First part is a theoretical realization of trapping of an electron using decoherence, followed by a realization of an electrically driven Single Photon source. The second part is a theoretical understanding of directionality of Field scattering in case of passive/hermitian Parity Time metasurfaces and the subsection leads to an experimental realization of such surface characteristics with the discussion focused on the first ever flexible broadband PT symmetric metasurface.

In the first chapter, an insight into the highly directional scattering characteristics of a one and two-dimensional passive Parity Time symmetry metasurface is discussed. The designs are discussed for both the visible (532 nm) and NIR (1550 nm) bands. The focus on PT-symmetric metasurfaces is because they are potential candidates for a distinctive avenue to explore diffraction orders through surface-confined passive nano-features. It is shown that when imposed on an optical metasurface surface, PT-symmetry is activated in these systems via amplitude and phase modulation, resulting in controlled diffraction orders as function of specific directions. The applied variations were found to maintain, enhance and suppress the orders.

The proposed structure is than modified to accommodate the need to observe directive scattering in air; thus the unit cell dimensions were increased so that diffraction orders can be supported in air. Then we optimized the structure dimensions to obtain the maximum imbalance in the efficiency of the corresponding diffraction orders in air. Moreover, this work was extended to be studies on two different substrates as shown in Chapter 2. In this chapter, it is experimentally and numerically established that the PT symmetry can be established through the diatomic Bravais

Lattices. Such lattices are not only suitable for single wavelength i.e. 532 nm, but it is extended over a broadband (400 – 600 nm) of wavelengths. The first ever example of a flexible PT meatsurface is presented and the transmission efficiency of the six observed diffraction orders is observed. The experimental results have an excellent agreement with numerical simulations. In addition, we have shown that different substrates, with few modifications to the structural dimensions, can still lead to the same results. Both substrates (sapphire and polyimide) are not lossy for the visible band.

In Chapter 3, we discuss quantum interference and decoherence phenomenon and more specifically utilizing decoherence to trap electron. A novel physical mechanism of electron-pocket scheme is employed, ensuring trapping of electron at high temperature range (100 to 300 K), with the trapping probability is discussed as a function of temperature (70 to 58 %). The decoherence-assisted trapping happens on a time scale of sub-picoseconds and does not require the switching of any external voltage. The internal dynamics inside the 5 QDs is on the sub-picosecond time scale, the electron is trapped as the decoherence isolates the electron in QD # 3 strongly from the leads due to the presence of the surrounding QDs # 1, 2, 4, and 5. A detailed set of calculation reveal the authenticity of results from the presented setup within ± 1 nm variations in sizes of the quantum dots and barriers. Furthermore, this model could be used to implement an efficient electrically driven single photon source operating at wavelengths $\lambda = 1.3 - 1.5$ μm and between 100 and 300 K as shown in Chapter 4.

Finally, as opposed to optically driven single photon source a room temperature model of an elusive electrically driven single photon source is presented. In contrast to work presented in Chapter 3, the proposed scheme is tinkered to work in the picosecond regime. The idea is based

on the fact that the numerical analysis reveal, a zero-decoherence scenario with a photon emission probability of less than 35%, whereas a 100 % photon emission is expected in the presence of decoherence at high temperature. The emitted photon is in the telecommunication range and emission times allow a ESPS operable at GHz frequencies and high temperatures. The ESPS is designed to work under strong-coupling (Rabi) or the weak-coupling (Purcell) regime, as long as the following criteria is met; (i) presence of decoherence, (ii) electronic injection rate is slower than the quantum dot-photon coupling.

APPENDIX A: ENERGY LEVELS AND WAVEFUNCTIONS OF CYLINDRICAL QUANTUM DOTS

As shown in Fig. 3-1, the 'intrinsic-region' constitutes 15% of the NR. In addition, the 'intrinsic-region' is along the z-axis. In this work, we consider the 'intrinsic-region' will be treated without curvature. We start with the Schrödinger's equation in cylindrical coordinates

$$E\Psi(\rho,\phi,z) = -\frac{\hbar^2}{2m^*}\left[\frac{1}{\rho}\partial_\rho\left(\rho\partial_\rho\Psi(\rho,\phi,z)\right) + \frac{1}{\rho^2}\partial_{\phi\phi}\Psi(\rho,\phi,z) + \partial_{zz}\Psi(\rho,\phi,z)\right] + V(\rho,\phi,z)\Psi(\rho,\phi,z) \quad \text{(A.1)}$$

where $E = E_\rho + E_z$ is the total eigenenergy of the electron. Applying separation of variables, the azimuthal differential equation and its normalized solution will be

$$\partial_{\phi\phi}\Phi(\phi) + m^2\Phi(\phi) = 0 \quad \text{(A.2)}$$

and

$$\Phi(\phi) = \frac{1}{\sqrt{2\pi}}e^{+im\phi} \quad \text{(A.3)}$$

where *m* is the azimuthal quantum number. As for the axial differential equation, it is as follows:

$$\frac{-\hbar^2}{2m^*}\mathrm{Z}(z) + V(z)\mathrm{Z}(z) = E_z Z(z) \quad \text{(A.4)}$$

The solution for the axial equation is shown later in Appendix C. As for the radial differential equation, it is as follows:

$$\partial_{\rho\rho}\mathrm{R}(\rho) + \frac{1}{\rho}\partial_\rho R(\rho) + \left(k_\rho^2 - \frac{m^2}{\rho^2}\right)R(\rho) = 0 \quad \text{(A.5)}$$

The general solution for the radial differential equation is

$$\mathrm{R}(\rho) = C_1 J_m(k_\rho\rho) + C_2 N_m(k_\rho\rho) \quad \text{(A.6)}$$

where J_m is the Bessel function first kind and N_m is the Bessel function second kind. In this work, not all QDs share the same boundary conditions, i.e. *electron pocket*. Both QD # 1 and # 5 do not share an interface with the *electron pocket*, thus at $\rho = 0$, $R(\rho)$ is finite, i.e. $C_2 = 0$. For both QD # 1 and # 5, at $\rho = r$, $R(\rho)$ is equal to zero. In order to satisfy this boundary condition, $k_\rho = \alpha_{mn}/r$. The radial wavefunction for both QD # 1 and # 5, is

$$\mathrm{R}(\rho) = C_1 J_m\left(\frac{\alpha_{mn}\rho}{r}\right) \tag{A.7}$$

The energy of the electron inside either QD # 1 or QD # 5 is the sum of the radial energy and the axial energy:

$$E = E_\rho + E_z \tag{A.8}$$

The axial energy will be explored in details in Appendix C. As for the radial energy, it is as follows:

$$\mathrm{E}_\rho = \frac{\hbar^2 \alpha_{mn}^2}{2m^* r^2} \tag{A.9}$$

C_1 is determined from the normalization condition as follows

$$|C_1|^2 \int_0^{\rho=r} \rho \left| J_m\left(\frac{\alpha_{mn}\rho}{r}\right)\right|^2 d\rho = 1 \tag{A.10}$$

As for QD # 2 and # 4, both are identical.

For $\rho < \gamma r$, the electron's energy is denoted by E_{in}, where $E_{in} = E_{\rho in} + E_{zin}$, while for $\rho > \gamma r$, the electron's energy is denoted by E_{out}, where $E_{out} = E_{\rho out} + E_{zout}$. Based on Fig. A-1, the boundary conditions are as follows:

1. At $\rho = 0$, $R(\rho)$ is finite.

2. At $\rho = \gamma r$, $R_{in}(\rho) = R_{out}(\rho)$.
3. At $\rho = \gamma r$, $\frac{dR_{in}(\rho)}{d\rho} = \frac{dR_{out}(\rho)}{d\rho}$.
4. At $\rho = r$, $R_{out}(\rho) = 0$.
5. Normalization condition: $|\langle R|R\rangle|^2 = 1$.
6. $E_{in} = E_{out}$.

Here γ is a constant factor that varies between 0 and 1. We set γ to be 0.533. The value of γ is chosen based on two factors. First, it is chosen to increase the efficiency of trapping through making t_{42} larger than $t_{32} + t_{43}$. Second, the value of γ makes the energy separation between the ground state's energy of QD # 2 or # 4 is almost 70 meV higher than the ground state's energy of QD # 3, hence the trapped electron will almost 1 ns to escape. For $\rho < \gamma r$, the radial differential equation is;

$$\partial_{\rho\rho}\mathrm{R}(\rho) + \frac{1}{\rho}\partial_{\rho}R(\rho) + \left(k_{\rho in}^2 - \frac{m^2}{\rho^2}\right)R(\rho) = 0 \tag{A.11}$$

where $E_{\rho in} = \hbar^2 k_{\rho in}^2/(2m^*)$. The general solution for Eq. (A.11) is,

$$\mathrm{R}_{in}(\rho) = C_3 J_m\left(k_{\rho in}\rho\right) + C_4 N_m\left(k_{\rho in}\rho\right) \tag{A.12}$$

From boundary condition 1, C_4 is zero. For $\rho > \gamma r$, the radial differential equation is,

$$\partial_{\rho\rho}\mathrm{R}(\rho) + \frac{1}{\rho}\partial_{\rho}R(\rho) + \left(k_{\rho out}^2 - \frac{m^2}{\rho^2}\right)R(\rho) = 0 \tag{A.13}$$

where $E_{\rho out} = \hbar^2 k_{\rho out}^2/(2m^*)$. The general solution for Eq. (A.13) is

$$\mathrm{R}_{out}(\rho) = C_5 J_m\left(k_{\rho out}\rho\right) + C_6 N_m\left(k_{\rho out}\rho\right) \tag{A.14}$$

Both R_{in} and R_{out} share the same *'m'*. From the boundary condition 4,

$$C_6 = -C_5 \frac{J_m(k_{\rho out} r)}{N_m(k_{\rho out} r)} \tag{A.15}$$

From both boundary conditions 2 and 3, and simple algebraic manipulation, the transcendental equation reads

$$k_{\rho out} J_m(k_{\rho in}\gamma r)\left[J'_m(k_{\rho out}\gamma r)N_m(k_{\rho out}\gamma r) - J_m(k_{\rho out}\gamma r)N'_m(k_{\rho out}\gamma r)\right]$$

$$=$$

$$k_{\rho in} J'_m(k_{\rho in}\gamma r)\left[J_m(k_{\rho out}\gamma r)N_m(k_{\rho out}\gamma r) - J_m(k_{\rho out}\gamma r)N_m(k_{\rho out}\gamma r)\right] \tag{A.16}$$

As shown in the above figure, the solution for this transcendental equation, with $\gamma = 0.533$, is $E = 0.348$ eV. QD # 3 is treated the same as both QD # 1 and # 5, but with different radius.

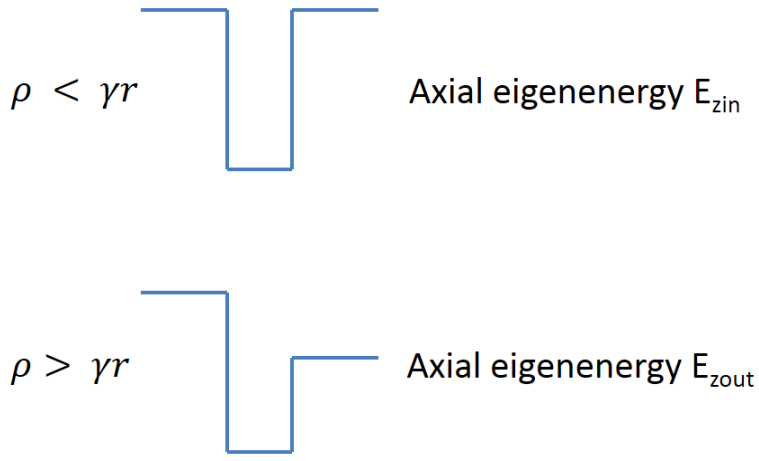

Figure A-1: Schematic for the QD # 2 or # 4 interface with the electron pocket.

APPENDIX B: ELECTRON-PHONON INTERACTION IN QUANTUM DOTS

The Fröhlich Hamiltonian describes the electron-LO phonon interaction (ELOPI). For quantum dots (QDs), it is as follows:

$$H_{e-ph} = \frac{1}{\sqrt{V}} \sum_{q,i,j} M_{q,i,j}\, a_i^{\dagger} a_j \left(b_q^{\dagger} + b_{-q}\right) \tag{B.1}$$

$$M_{q,i,j} = i\sqrt{4\alpha}\,\frac{\hbar\omega_q}{q}\left(\frac{\hbar}{2m^*\omega_q}\right)^{1/4} \langle i|e^{iq.r}|j\rangle \tag{B.2}$$

Where α is the Fröhlich coupling constant. In bulk InAs, α is 0.052, however, in InAs QDs it should be 0.15 [96, 97]. $|i\rangle$ is the wavefunction for the electron level *i* in the QD. *V* is the volume of the NR. The phonons are assumed to be the same as those in the bulk $In_{0.45}Ga_{0.55}As$, since 85% of the NR is made of $In_{0.45}Ga_{0.55}As$. In this work, the LO phonons are regarded as dispersionless; $\hbar\omega_q = \hbar\omega_{LO} = 32$ meV. We calculate the strength of couplings, in each QD, for the following cases: $|i\rangle = |j\rangle = |g\rangle$, $|i\rangle = |j\rangle = |e\rangle$ and ($|i\rangle = |g\rangle$ and $|j\rangle = |e\rangle$), where $|g\rangle$ ($|e\rangle$) is the ground (excited) state. The coupling strength in Eqn. (2) is calculated as follows;

$$\lambda^2 = \sum_{|\boldsymbol{q}|\leq 2\pi\backslash L} \left|\lambda_{\boldsymbol{q}}\right|^2 \tag{B.3}$$

$$= \frac{1}{V}\sum_{|q|\leq 2\pi\backslash L} \left|M_{q,i,j}\right|^2 \tag{B.4}$$

$$= \frac{4\alpha V}{(2\pi)^3}(\hbar\omega_{LO})^2 \sqrt{\frac{\hbar}{2m^*\omega_{LO}}} \left|\left\langle i\left|\frac{2\pi}{r^2}\right|j\right\rangle\right|^2 \tag{B.5}$$

where $r = \sqrt{\rho^2 + z^2}$. For both $M_{q,g,g}$ and $M_{q,e,e}$, an all five QDs, $g = \lambda/(\hbar\omega_{LO}) = 0.066$. Consequently, e^{-2g^2} will be almost 1. As for $M_{q,g,e}$ or $M_{q,e,g}$, in all five QDS, they are almost 0.0066.

APPENDIX C: THE AXIAL ENERGY LEVELS OF THE CYLINDRICAL QUANTUM DOTS

Writing down the solution for Schrödinger's non-relativistic independent equation for the QD's different regions along the z-axis, for $-\infty < z < a$ (see Fig. C-1),

$$Z_1(z) = Ae^{k_{n-1}(z-a)} \tag{C.1}$$

For $a < z < a + z_1$,

$$Z_2(z) = Bcos\big(k_n(z-a)\big) + Csin\big(k_n(z-a)\big) \tag{C.2}$$

where z_1 is the height of the QD. For $a + z_1 < z < \infty$,

$$Z_3(z) = De^{-k_{n+1}(z-a)} \tag{C.3}$$

From the boundary conditions at $z = a$,

$$B = A \tag{C.4}$$

$$C = \sigma_1 A \tag{C.5}$$

where $\sigma_1 = \frac{m_n k_{n-1}}{m_{n-1} k_n}$. From the boundary conditions at $z = a + z_1$,

$$Bcos(k_n z_1) + Csin(k_n z_1) = De^{-k_{n+1} z_1} \tag{C.6}$$

and

$$-\frac{k_n}{m_n} Bsin(k_n z_1) + \frac{k_n}{m_n} Csin(k_n z_1) = -\frac{k_{n+1}}{m_{n+1}} De^{-k_{n+1} z_1} \tag{C.7}$$

From Eqns. (C.1) to (C.4), respectively, will be

$$Acos(k_n z_1) + \sigma_1 Asin(k_n z_1) = De^{-k_{n+1} z_1} \tag{C.8}$$

and

$$-Asin(k_n z_1) + \sigma_1 Acos(k_n z_1) = -\sigma_2 De^{-k_{n+1} z_1} \quad \text{(C.9)}$$

where $\sigma_2 = \frac{m_n k_{n+1}}{m_{n+1} k_n}$. Getting rid of A by dividing Eqn. (C.8) by Eqn. (C.9) and after few straightforward algebraic steps, the transcendental equation, for the QD eigen energies, is as follows:

$$tan(k_n z_1) = \frac{\sigma_2 + \sigma_1}{1 - \sigma_1 \sigma_2} \quad \text{(C.10)}$$

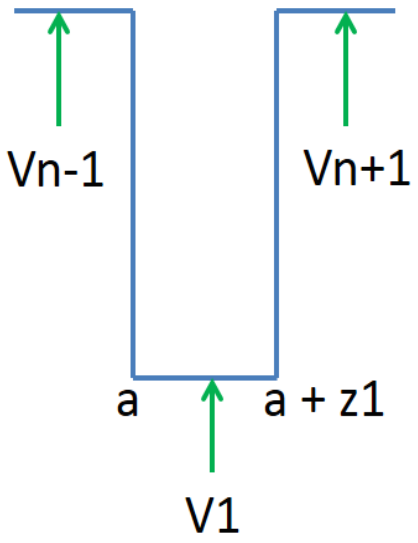

Figure C-1: Schematic for the QD's height.

A graphical solution has provided the eigen energies for each QD (see Fig. C-2). Back to Eqns. (C.8) and (C.9), D in terms of A is as follows:

$$D = \frac{\sigma_1^2 + 1}{\sigma_1 + \sigma_2} sin(k_n z_1) e^{k_{n+1} z_1} A \quad \text{(C.11)}$$

After normalization, we obtain $A = 1/\sqrt{N}$, where

$$N = \frac{1}{2k_{n-1}} + \left(\frac{\sigma_1^2 + 1}{\sigma_1 + \sigma_2}\right)^2 sin^2(k_n z_1) \frac{1}{2k_{n+1}} + \frac{1}{4k_n}\left(2k_n z_1 + sin(2k_n z_1)\right)$$

$$+\sigma_1^2\left(\frac{z_1}{2} - \frac{sin(2k_n z_1)}{4k_n}\right) - \frac{\sigma_1}{2k_n}(cos(2k_n z_1) - 1) \qquad \text{(C.12)}$$

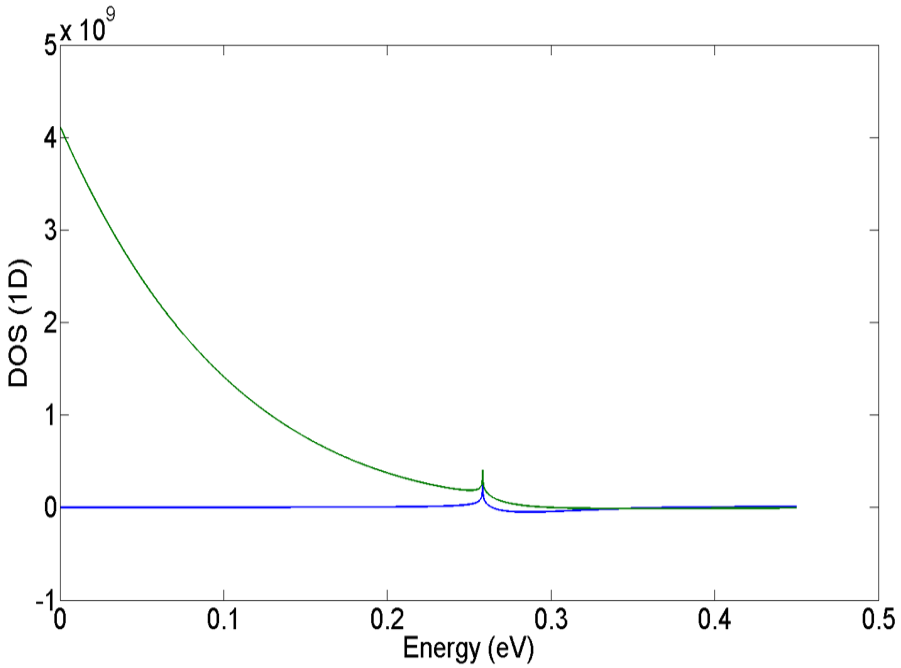

Figure C-2: The solution for the transcendental equation.

APPENDIX D: APPROXIMATION OF THE HOPPING MATRIX ELEMENTS

As an illustration, in this appendix we are going to generalize the 1D calculation of the hopping matrix elements for a symmetric double-well potential presented in Ref. [98] to the case of an asymmetric double-well potential. We emphasize that we do not use this approximation in the calculations. This appendix is provided for educational purpose only. The effective Hamiltonian for a coupled two-level system is,

$$H = \begin{pmatrix} \epsilon & t \\ t & -\epsilon \end{pmatrix} \tag{D.1}$$

where 2ϵ is the bias between the right and left well, and t is the hopping matrix element. The eigenenergies are $E_{\pm} = \sqrt{\epsilon^2 + t^2}$. The corresponding eigenstates are

$$|\psi_+\rangle = \cos\frac{\theta}{2}|\psi_R\rangle + \sin\frac{\theta}{2}|\psi_L\rangle \tag{D.2}$$

$$|\psi_-\rangle = -\sin\frac{\theta}{2}|\psi_R\rangle + \cos\frac{\theta}{2}|\psi_L\rangle \tag{D.3}$$

where $tan\theta = t/\epsilon$ with $0 \leq \theta < \pi$. For determining E_+ we use the following two Schrödinger equations:

$$\psi_R'' + \frac{2m}{\hbar^2}(E_R - V)\psi_R = 0 \tag{D.4}$$

$$\psi_+'' + \frac{2m}{\hbar^2}(E_+ - V)\psi_+ = 0 \tag{E.5}$$

where V is the 1D potential shown in Fig. D-1. Multiplying ψ_+ and ψ_R to Eqns. (D.4) and (D.5) respectively, and taking the difference results in we get,

$$\psi_+\psi_R'' - \psi_R\psi_+'' + \frac{2m}{\hbar^2}(E_R - E_+)\psi_R\psi_+ = 0 \tag{D.6}$$

After integration from 0 to infinity and integrating by parts, we obtain

$$E_+ - E_R = \frac{\hbar^2}{2m\delta_{R,+}^+}[-\psi_+(0)\psi_R'(0) + \psi_R(0)\psi_+'(0)] \tag{D.7}$$

where $\delta_{R,+}^+ = \int_0^\infty \psi_R\psi_+ dx$.

A similar calculation can be done for determining $E_- - E_R$. Evaluating the difference, we obtain

$$E_- - E_+ = \frac{\hbar^2}{2m\delta_{R,+}^+}[-\psi_+(0)\psi_L'(0) + \psi_L(0)\psi_+'(0)]$$

$$- \frac{\hbar^2}{2m\delta_{R,+}^+}[-\psi_+(0)\psi_R'(0) + \psi_R(0)\psi_+'(0)] \tag{D.8}$$

where $\delta_{L,+}^+ = \int_0^\infty \psi_L\psi_+ dx$. Using the approximation $\delta_{R,-}^+ \approx -sin\frac{\theta}{2}$ and $\delta_{R,+}^+ \approx -cos\frac{\theta}{2}$, we can substantially simplify the above equation to

$$E_- - E_+ = \frac{\hbar^2}{2m}\left[cot\frac{\theta}{2} + tan\frac{\theta}{2}\right] \times [\psi_L(0)\psi_R'(0) - \psi_R(0)\psi_L'(0)] \tag{D.9}$$

Using the formulas $tan\frac{\theta}{2} = \frac{1-cos\theta}{sin\theta}$ and $cot\frac{\theta}{2} = \frac{1+cos\theta}{sin\theta}$, we obtain

$$E_- - E_+ = \frac{\hbar^2 k^2}{m\, sin\theta} = 2\sqrt{\epsilon^2 + t^2} \tag{D.10}$$

where we defined $k^2 = [\psi_L(0)\psi_R'(0) - \psi_R(0)\psi_L'(0)]$. Since $sin\theta = t/\sqrt{\epsilon^2 + t^2}$, we get

$$t = \frac{\hbar^2 k^2}{2m} \tag{D.11}$$

We compared this approximation with the result obtained using Eqn. (20). Our calculations show that this approximation gives about 50% of the kinetic matrix element in Eqn. (20) and about 40%

of the total matrix element in Eqn. (20). This discrepancy is due to the approximations $\delta_{R,-}^{+} \approx -sin\frac{\theta}{2}$ and $\delta_{R,+}^{+} \approx -cos\frac{\theta}{2}$, which neglect the tails of the wave functions. This result illustrates also the importance of including the off-diagonal matrix elements of the potential.

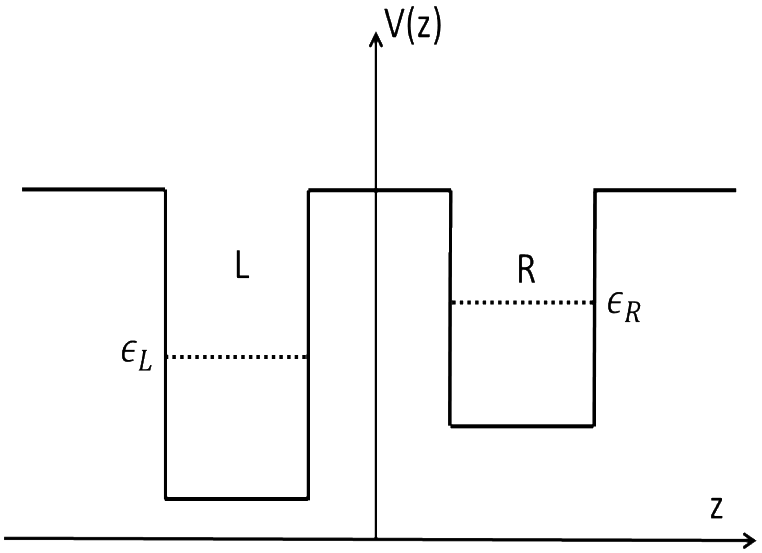

Figure D-1: Schematic showing an asymmetric double well potential.

APPENDIX E: ELECTRON'S OSCILLATIONS AMONG THE FIVE QUANTUM DOTS

In this appendix, we change the initial conditions from $\rho_{SES} = 1$ to $\rho_{11} = 1$. This is just to show the oscillations that are suppressed by decoherence if the initial condition is $\rho_{SES} = 1$ (see Fig. 3-7). Note that despite the change in the initial condition, the results are the same. In addition, the scale here is in the picosecond scale, while the previous results are in nanoscale because, in this work, the injection rate from the SES to the NR is 5×10^9 s^{-1}.

APPENDIX F: SINGLE ELECTRON SOURCE

In this section we discuss the physics behind the SES. The studied configuration can operate at room temperature (T = 300 K). This imposes requirements on the SES. Here, we propose a scheme for an SES operating at high temperature (100– 200 K). The main idea of SESs is to realize a confined region in a two-dimensional (2D) n-doped GaAs through quantum point contacts (QPCs). The single electron injection is achieved by applying a magnetic field that causes a Zeeman splitting of the QD levels. A sudden voltage step is applied to push the electron above the Fermi energy, which results in the emission of a single electron by tunneling through the barrier of the QPC. The charging energy is $\Delta + e^2/C \approx \Delta$. The capacitance is usually small, so the total charging energy is almost equal to the energy level spacing. The energy level spacing corresponds to the Zeeman splitting due to the magnetic field. Zeeman splitting in QDs is

$$\Delta_Z = g\mu_B B \tag{F.1}$$

where $\mu_B = \frac{e\hbar}{2m_e}$ is the Bohr magneton, g is Landé factor, and B is the applied magnetic field. In order to achieve a single electron injection at higher temperature, Δ_Z has to be larger than k_BT. Consequently, at T = 150 K, Δ_Z has to be larger than 17 meV in order to get a single electron injection. Such energy level spacing can be realized if the 2D GaAs is replaced with a material with smaller effective mass, like for example InAs. This would increase the Bohr magneton by factor of almost 3. Another parameter than can be modified is the Landé factor, which can range between − 15 and + 2 [130]. Thus, the QD defined by the QPCs should result in large Landé factor. Based on the above modifications, the applied magnetic field can be relatively small on the order of 1 T, thereby ensuring the operation of the ESPS at high temperature.

REFERENCES

[1] C. M. Bender and S. Boettcher, Phys. Rev. Lett. **80**(24), 5243 (1998).

[2] K. G. Makris, R. El-Ganainy, D. N. Christodoulides, and Z. H. Musslimani, Phys. Rev. Lett. **100**, 103904 (2008).

[3] C. E. R¨uter et al. Nature Phys. **6**, 192 (2010).

[4] A. Guo et al. Phys. Rev. Lett. **103**, 093902 (2009).

[5] S. Longhi, Phys. Rev. Lett. **103**, 123601 (2009).

[6] H. Hodaei, M. A. Miri, M. Heinrich, D. N. Christodoulides, and M. Khajavikhan, Science, **346**(6212), 975 (2014).

[7] L. Feng, Z. J. Wong, R.-M. Ma, Y. Wang, and X. Zhang, Science, **346**, 972 (2014).

[8] H. Ramezani, D. N. Christodoulides, V. Kovanis, I. Vitebskiy, and T. Kottos, Phys. Rev. Lett. **109**, 033902 (2012).

[9] T. Kottos, Nature Phys. **6**, 166 (2010).

[10] S. Klaiman, U. G¨unther, and N. Moiseyev, Phys. Rev. Lett. **101**, 080402 (2008).

[11] B. Peng et al., Nature Phys. **10**, 394 (2014).

[12] A. Regensburger et al., Nature, **488**, 167 (2012).

[13] Z. Lin et al., Phys. Rev. Lett. **106**, 213901 (2011).

[14] G. Castaldi, S. Savoia, V. Galdi, A. Al`u, and N. Engheta, Phys. Rev. Lett. **110**, 173901 (2013).

[15] N. Yu and F. Capasso, Nature Mater. **13**, 139 (2014).

[16] A. V. Kildishev, A. Boltasseva, and V. M. Shalaev, Science, **339**(6125), 1232009 (2013).

[17] S. Larouche and D. R. Smith, Opt. Lett. **37**, 2391 (2012).

[18] N. Yu et al., Science, **334**(6054), 333 (2011).

[19] F. Aieta et al., Nano Lett. **12**, 1702 (2012).

[20] P. Genevet et al., Appl. Phys. Lett. **100**, 013101 (2012).

[21] R. Blanchard et al., Phys. Rev. B, **85**, 155457 (2012).

[22] F. Aieta et al., Nano Lett. **12**, 4932 (2012).

[23] Y. Ra'di, V. S. Asadchy and S. A. Tretyakov, IEEE Transactions on Antennas and Propagation, **61**(9), 4606 (2013).

[24] V. S. Asadchy, Y. Ra'di, J. Vehmas, and S. A. Tretyakov, Phys. Rev. Lett. **114**, 095503 (2015).

[25] L. Poladian, Phys. Rev. E. **54**, 2963 (1996).

[26] M. V. Berry, J. Phys. Math. Gen. **31**, 3493 (1998).

[27] R. Birabassov, A. Yesayan, and T. V. Galstyan, Opt. Lett. **24**,1669 (1999).

[28] N. X. A. Rivolta and B. Maes, J. Opt. Soc. Amer. B, **32**, 1330 (2015).

[29] S. Phang, A. Vukovic, H. Susanto, T. M. Benson, and P. Sewell, J. Opt. Soc. Amer. B, **30**, 2984 (2013).

[30] M. Kulishov, H. F. Jones, and B. Kress, Opt. Express, **23**(7), 9347 (2015).

[31] M. Kulishov and B. Kress, Opt. Express, **20**, 29319 (2012).

[32] R. Fleury, D. L. Sounas, and A. Al`u, Phys. Rev. Lett. **113**, 023903 (2014).

[33] Y. Jia, Y. Yan, S. V. Kesava, E. D. Gomez, and N. C. Giebink, ACS Photon. **2**(2), 319 (2015).

[34] Y. Yan and N. C. Giebink, Adv. Opt. Mater. **2**(5), 423 (2014).

[35] H. Kogelnik, Bell Syst. Tech. J. **48**, 2909 (1969).

[36] M. G. Moharam, and T. K. Gaylord, J. Opt. Soc. Amer. **72**, 1385 (1982).

[37] J. Albero et al., Appl. Opt. **52**, 3637 (2013).

[38] H. H. Li, J. Phys. Chem. Ref. Data, **9**(3), 561 (1980).

[39] A. D. Raki´c, A. B. Djuriˇsi´c, J. M. Elazar, and M. L. Majewski, Appl. Opt. **37**, 5271 (1998).

[40] I. H. Malitson, J. Opt. Soc. Amer. **52**, 1377 (1962).

[41] M. Wimmer, M-A. Miri, D. N. Christodoulides and U. Peschel, Sci. Rep. **5**, 17760 (2015).

[42] K. G. Makris, Z. H. Musslimani, D. N. Christodoulides and S. Rotter, Nature Comm. **6**, 7257 (2015).

[43] L. Feng, et al. Nature Mater. **12**(2), 108 (2013).

[44] X. Yin, and X. Zhang, Nature Mater. **12**(3), 175 (2013).

[45] R. C. Devlin, et al. Proceedings of the National Academy of Sciences, 201611740 (2016).

[46] X. Ni, A. V. Kildishev and V. M. Shalaev, Nature Comm., **4**, 2807 (2013).

[47] Y. Zhao, M. A. Belkin and A. Alù, Nature Comm. **3**, 870 (2012).

[48] G. Wiederrecht, Handbook of Nanofabrication (Elsevier, Amsterdam, 2010).

[49] M. Stepanova and S. Dew (Editors) Nanofabrication Techniques and Principles, (Springer, 2012).

[50] M. J. Madou, Fundamentals of Microfabrication: The Science of Miniaturization (CRC Press, Second Edition, 2002).

[51] https://rsc.aux.eng.ufl.edu/_files/documents/177.pdf]

[52] A. A. Tseng, Nanofabrication: Fundamentals and Applications (World Scientific Publishing Company, 2008).

[53] Z. Cui, Nanofabrication: Principles, Capabilities and Limits (Springer, New York, 2009).

[54] S. Cabrini and S. Kawata, Nanofabrication Handbook (CRC Press, Boca Raton, 2012).

[55] H.-P. Breuer and F. Petruccione, The Theory of Open Quantum Systems (Oxford University Press, New York, 2002).

[56] J. Fischer and D. Loss, Science **324**, 1277 (2009).

[57] S. Deleglise, I. Dotsenko, C. Sayrin, J. Bernu, M. Brune, J.-M. Raimond, and S. Haroche, Nature **455**, 510 (2008).

[58] A. van Oudenaarden, M. Devoret, Y. Nazarov, and J. Mooij, Nature **391**, 768 (1998).

[59] A. Bachtold, C. Strunk, J. Salvetat, J. Bonard, L. Forro, T. Nussbaumer, and C. Schönenberger, Nature **397**, 673 (1999).

[60] J. R. Anglin, J. P. Paz, and W. H. Zurek, Phys. Rev. A **55**, 4041 (1997).

[61] P. W. Shor, Phys. Rev. A **52**, R2493 (1995).

[62] H. Bluhm, S. Foletti, I. Neder, M. Rudner, D. Mahalu, V. Umansky, and Yacoby, Nature Phys. **7**, 109 (2011).

[63] J. Petta, A. Johnson, J. Taylor, E. Laird, A. Yacoby, M. Lukin, C. Marcus, M. Hanson, and A. Gossard, Science **309**, 2180 (2005).

[64] H. Rabitz, R. de Vivie-Riedle, M. Motzkus, and K. Kompa, Science **288**, 824 (2000).

[65] G. A. Álvarez and D. Suter, Phys. Rev. Lett. **107**, 230501 (2011).

[66] M. Mohseni, P. Rebentrost, S. Lloyd, and A. Aspuru-Guzik, J. Chem. Phys. **129**, 174106 (2008).

[67] F. Caruso, A. W. Chin, A. Datta, S. F. Huelga, and M. B. Plenio, J. Chem. Phys. **131**, 105106 (2009).

[68] M. B. Plenio and S. F. Huelga, New J. Phys. **10**, 113019 (2008).

[69] F. L. Semiao, K. Furuya, and G. J. Milburn, New J. Phys. **12**, 083033 (2010).

[70] S. Lloyd and M. Mohseni, New J. Phys. **12**, 075020 (2010).

[71] D. Giulini, E. Joss, C. Kiefer, J. Kupsch, I.-O. Stamatescu, and H. D. Zeh, Decoherence and Appearance of a Classical World in Quantum Theory (Springer, New York, 1996).

[72] G. A. Álvarez and D. Suter, Phys. Rev. A **84**, 012320 (2011).

[73] M. B. and S. C. G., J. Math. Phys. **18**, 756 (1977).

[74] B. Kaulakys and V. Gontis, Phys. Rev. A **56**, 1131 (1997).

[75] D. Loss and K. Mullen, Phys. Rev. B **43**, 13252 (1991).

[76] G. A. Fiete and E. J. Heller, Phys. Rev. A **68**, 022112 (2003).

[77] A. Stern, Y. Aharonov, and Y. Imry, Phys. Rev. A **41**, 3436 (1990).

[78] G. Feve, A. Mahe, J. M. Berroir, T. Kontos, B. Placais, D. C. Glattli, A. Cavanna, B. Etienne, and Y. Jin, Science **316**, 1169 (2007).

[79] E. Bocquillon, F. D. Parmentier, C. Grenier, J.-M. Berroir, P. Degiovanni, D. C. Glattli, B. Placais, A. Cavanna, Y. Jin, and G. Fève, Phys. Rev. Lett. **108**, 196803 (2012).

[80] M. A. Omar, Elementary Solid State Physics (Addison-Wesley Publishing Company, Massachusetts, 1975).

[81] T. Inoshita and H. Sakaki, Phys. Rev. B **56**, R4355 (1997).

[82] E. Stock, M.-R. Dachner, T. Warming, A. Schliwa, A. Lochmann, A. Hoffmann, A. I. Toropov, A. K. Bakarov, I. A. Derebezov, M. Richter, V. A. Haisler, A. Knorr, and D. Bimberg, Phys. Rev. B **83**, 041304 (2011).

[83] K. E. Cahill and R. J. Glauber, Phys. Rev. **177**, 1857 (1969)

[84] K. E. Cahill and R. J. Glauber, Phys. Rev. **177**, 1882 (1969).

[85] K. Blum, Density Matrix Theory and Applications (Plenum Press, New York, 1996).

[86] P. Borri, W. Langbein, J. Mørk, J. M. Hvam, F. Heinrichsdorff, M.-H. Mao, and Bimberg, Phys. Rev. B **60**, 7784 (1999).

[87] A. V. Uskov, A.-P. Jauho, B. Tromborg, J. Mørk, and R. Lang, Phys. Rev. Lett. **85**, 1516 (2000).

[88] P. Borri, W. Langbein, S. Schneider, U. Woggon, R. L. Sellin, D. Ouyang, and D. Bimberg, Phys. Rev. Lett. **87**, 157401 (2001)

[89] S. Sauvage, P. Boucaud, R. P. S. M. Lobo, F. Bras, G. Fishman, R. Prazeres, F. Glotin, J. M. Ortega, and J.-M. Gérard, Phys. Rev. Lett. **88**, 177402 (2002).

[90] S. Hameau, Y. Guldner, O. Verzelen, R. Ferreira, G. Bastard, J. Zeman, A. Lemaitre, and J. M. Gérard, Phys. Rev. Lett. **83**, 4152 (1999).

[91] T. Inoshita and H. Sakaki, Phys. Rev. B **46**, 7260 (1992).

[92] S. Buckley, K. Rivoire, and J. Vućković, Rep. Prog. Phys. **75**, 126503 (2012).

[93] F. M. Ross, Rep. Prog. Phys. **73**, 114501 (2010).

[94] S. Y. Chou and P. B. Fischer, J. Vac. Sci. Technol. B **8** (1990).

[95] P. J. Pauzauskie, D. J. Sirbuly, and P. Yang, Phys. Rev. Lett. **96**, 143903 (2006).

[96] R. Heitz, I. Mukhametzhanov, O. Stier, A. Madhukar, and D. Bimberg, Phys. Rev. Lett. **83**, 4654 (1999).

[97] M. A. Odnoblyudov, I. N. Yassievich, and K. A. Chao, Phys. Rev. Lett. **83**, 4884 (1999).

[98] L. D. Landau and E. M. Lifshitz, Quantum Mechanics: Non-Relativistic Theory (Oxford University Press, New York, 1977).

[99] B. Lounis B and M. Orrit, Rep. Prog. Phys. **68**, 1129 (2005).

[100] C. Santori, D. Fattal and Y. Yamamoto, Single-photon Devices and Applications (Weinheim: Wiley, 2010).

[101] C. K. Hong, Z. Y. Ou and L. Mandel, Phys. Rev. Lett. **59**, 2044 (1987).

[102] M. A. Nielsen and I. L. Chuang, Quantum Computation and Quantum Information (Cambridge: Cambridge University Press, 2000)

[103] A. K. Ekert, J. G. Rarity, P. R. Tapster and G. M. Palma, Phys. Rev. Lett. **69**, 1293 (1992).

[104] D. C. Burnham and D. L. Weinberg, Phys. Rev. Lett. **25**, 84 (1970).

[105] Y. R. Shen, The Principles of Nonlinear Optics (New York: Wiley, 1984).

[106] M. Keller, B. Lange, K. Hayasaka, W. Lange and H. Walther, Nature **431**, 1075 (2004).

[107] P. Maunz, D. Moehring, S. Olmschenk, K. Younge, D. Matsukevich and C. Monroe, Nature Phys. **3**, 538 (2007).

[108] P. Michler, A. Kiraz, C. Becher, W. V. Schoenfeld, P. M. Petroff, L. Zhang, E. Hu and A. Imamoglu, Science **290**, 2282 (2000).

[109] A. Beveratos, R. Brouri, T. Gacoin, J. P. Poizat and P. Grangier, Phys. Rev. A **64**, 061802 (2001).

[110] C. Brunel, B. Lounis, P. Tamarat and M. Orrit, Phys. Rev. Lett. **83**, 2722 (1999).

[111] Z. Yuan, B. Kardynal, R. Stevenson, A. Shields, C. Lobo, K. Cooper, N. Beattie, D. Ritchie and M. Pepper, Science **295**, 102 (2002).

[112] O. Benson, C. Santori, M. Pelton and Y. Yamamoto, Phys. Rev. Lett. **84**, 2513 (2000).

[113] A. Imamoglu and Y. Yamamoto, Phys. Rev. Lett. **72**, 210 (1994).

[114] P. Michler et al., Science **290**, 2282 (2000).

[115] Z. Yuan et al. *Science* **295**, 102 (2002).

[116] C. L. Salter et al. *Nature* **465**, 594 (2010).

[117] S. Kako et al. *Nature Mater.* **5**, 887 (2006).

[118] S. Strauf et al. *Nature Photon.* **1**, 704 (2007).

[119] N. Mizuochi et al., Nature Photon. **6**, 299 (2012).

[120] J. McKeever, A. Boca, A. D. Boozer, R. Miller, J. R. Buck, A. Kuzmich and H. J. Kimble, Science **303**, 1992 (2004).

[121] C. Kurtsiefer, S. Mayer, P. Zarda and H. Weinfurter, Phys. Rev. Lett. **85**, 290 (2000).

[122] N. Mizuochi et al. Nature Photon. **6**, 299 (2012).

[123] M. B. Ward, T. Farrow, P. See, Z. L. Yuan, O. Z. Karimov, A. J. Bennett, A. J. Shields, P. Atkinson, K. Cooper and D. A. Ritchie, Appl. Phys. Lett. **90**, 063512 (2007).

[124] A. E. Halawany and M. N. Leuenberger, Phys. Status Solidi b **251**, 1498 (2014).

[125] H. J. Carmichael, Statistical Methods in Quantum Optics (Berlin: Springer, 1999).

[126] K. Vahala, Nature **424**, 839 (2003).

[127] J. Reithmaier, G. Sek, A. Loffler, C. Hofmann, S. Kuhn, S. Reitzenstein, L. Keldysh, V. Kulakovskii, T. Reinecke and A. Forchel, Nature **432**, 197 (2004).

[128] M. Fox, Quantum Optics (Oxford: Oxford University Press, 2006)

[129] R. Loudon, The Quantum Theory of Light (Oxford: Oxford University Press, 1984).

[130] C. E. Pryor and M. E. Flatté, Phys. Rev. Lett. **96**, 026804 (2006).